
Helmholtzian Eigenmap: Topological feature discovery & edge flow learning from point cloud data

Yu-Chia Chen
Meta Platforms, Inc.
Seattle, WA 98109
yuchaz@uw.edu

Weicheng Wu
Department of Statistics
University of Washington
Seattle, WA 98195
weich555@uw.edu

Marina Meilă
Department of Statistics
University of Washington
Seattle, WA 98195
mmp2@uw.edu

Ioannis G. Kevrekidis
Chemical and Biomolecular Engineering &
Applied Mathematics and Statistics
Johns Hopkins University
Baltimore, MD 21218
yannisk@jhu.edu

Abstract

The manifold Helmholtzian (1-Laplacian) operator Δ_1 elegantly generalizes the Laplace-Beltrami operator to vector fields on a manifold \mathcal{M} . In this work, we propose the estimation of the manifold Helmholtzian from point cloud data by a weighted 1-Laplacian \mathcal{L}_1 . While higher order Laplacians have been introduced and studied, this work is the first to present a graph Helmholtzian constructed from a simplicial complex as a *consistent* estimator for the continuous operator in a non-parametric setting. Equipped with the geometric and topological information about \mathcal{M} , the Helmholtzian is a useful tool for the analysis of flows and vector fields on \mathcal{M} via the Helmholtz-Hodge theorem. In addition, the \mathcal{L}_1 allows the smoothing, prediction, and feature extraction of the flows. We demonstrate these possibilities on substantial sets of synthetic and real point cloud datasets with non-trivial topological structures; and provide theoretical results on the limit of \mathcal{L}_1 to Δ_1 .

1 Motivation

In this paper we initiate the estimation of higher order Laplacian operators from point cloud data, with a focus on the first order Laplacian operator Δ_1 of a manifold. Laplacians are known to be intimately tied to a manifold's topology and geometry. While the *Laplace-Beltrami* operator Δ_0 , an operator acting on functions (0-forms), is well studied and pivotal in classical manifold learning; estimating the 1-Laplacian Δ_1 , an operator acting on vector fields (1-forms), for a manifold has rarely been attempted yet. Order k Laplacian operators (on k -forms), denoted Δ_k , exist as well, for $k = 1, 2, \dots$

The discrete operator analogue of Δ_k , known as the *k-Hodge Laplacian matrix* \mathbf{L}_k , has been proposed more than 7 decades ago [Eck44]. The beauty of the aforementioned framework generated numerous applications in areas such as numerical analysis [AFW10, Dod76], edge flow learning on graphs [SBH⁺20, JSSB19], pairwise ranking [JLYY11], and game theory [CMOP11].

Being able to estimate Δ_1 by a discrete Helmholtzian \mathcal{L}_1 acting on the edges of a graph can support many applications, just as the Δ_0 estimator by weighted Laplacians successfully did. For instance, (i) topological information, i.e., the first Betti number β_1 [Lim20], can be obtained by the dimension of

the null space of \mathcal{L}_1 ; (ii) low dimensional representation of the space of vector fields on a manifold are made possible, similar to the dimensionality reduction algorithms such as Laplacian Eigenmap from the discrete estimates of Δ_0 ; (iii) the well known *Helmholtz-Hodge decomposition* (HHD) [BNPB13, Lim20] allows us to test, e.g., if a vector field on the manifold \mathcal{M} is approximately a gradient or a rotational field; lastly (iv), edge flow semi-supervised learning (SSL) and unsupervised learning algorithms, i.e., flow prediction and flow smoothing in edge space, can be easily derived from the well-studied node based learning models [BNS06, OFK⁺18] with the aid of \mathcal{L}_1 .

In this work, we propose a discrete estimator (\mathcal{L}_1) of the Helmholtzian Δ_1 with proper triangular weights which resembles the well known Vietoris-Rips (VR) complex in the persistent homology theory. We show separately the (pointwise) convergence of the down and the up components of the discrete graph Helmholtzian \mathcal{L}_1 to the continuous operators Δ_1^{down} and Δ_1^{up} . In addition, we present several applications to graph signal processing and semi-supervised learning algorithms on the edge flows with the constructed \mathcal{L}_1 . We support our theoretical claims and illustrate the versatility of the proposed Δ_1 estimator with extensive empirical results on synthetic and real datasets with non-trivial manifold structures.

In the next section we briefly introduce Hodge theory and higher order Laplacians. Section 3 presents the \mathcal{L}_1 construction algorithm. The theoretical results are in Section 4. Sections 6 and 7 provide several applications of the estimated Helmholtzian to the analysis of vector fields. Those Figure/Table/Equation/Theorem references with prefix S are in the Supplement.

2 Background: Hodge theory

Simplicial complex A natural extension of a graph to higher dimensional relations is called a *simplicial complex*. Define a k -simplex to be a k -dimensional polytope which is the convex hull of its $k + 1$ (affinely independent) vertices. A simplicial complex SC is a set of simplices such that every *face* of a simplex from SC is also in SC. Let Σ_k be the collection of k -simplices σ_k of SC; we write $\text{SC} = (\Sigma_0, \Sigma_1, \dots, \Sigma_\ell)$, with $n_k = |\Sigma_k|$. A graph is $G = (V, E) = (\Sigma_0, \Sigma_1)$, with $n_0 = |V| = n$. In this work, we focus on dimension $k \leq 2$ and simplicial complexes of the form $\text{SC}_2 = (V, E, T) = (\Sigma_0, \Sigma_1, \Sigma_2)$, where T is the set of triangles of SC.

k (co-)chain Given an arbitrary orientation for each simplex $\sigma_i^k \in \Sigma_k$, one can define the finite-dimensional vector space \mathcal{C}_k over Σ_k with coefficients in \mathbb{R} . An element $\omega_k \in \mathcal{C}_k$ is called a k -chain and can be written as $\omega_k = \sum_i \omega_{k,i} \sigma_i^k$. Since \mathcal{C}_k is isomorphic to \mathbb{R}^{n_k} , ω_k can be represented by a vector of coordinates $\omega_k = (\omega_{k,1}, \dots, \omega_{k,n_k})^\top \in \mathbb{R}^{n_k}$. \mathcal{C}^k denotes the dual space of \mathcal{C}_k ; an element of $\omega^k \in \mathcal{C}^k$ is called a k -cochain. Even though they are intrinsically different, we will use *chains* and *cochains* interchangeably for simplicity in this work. Readers are encouraged to consult [Lim20] for thorough discussions on the distinction between these two terms.

(Co-)boundary map The *boundary map (operator)* $\mathcal{B}_k : \mathcal{C}_k \rightarrow \mathcal{C}_{k-1}$ (defined rigorously in the Supplement C) maps a simplex σ_k to the $k - 1$ -chain of its faces, with signs given by the orientation of the simplex w.r.t. each face. For example, let $x, y, z \in V$, edges $[x, y], [y, z], [x, z] \in E$, and a triangle $t = [x, y, z] \in T$, we have $\mathcal{B}_2(t) = [x, y] + [y, z] - [x, z]$. Since \mathcal{C}_k is isomorphic to \mathbb{R}^{n_k} , one can represent \mathcal{B}_k by a *boundary map (matrix)* $\mathbf{B}_k \in \{0, \pm 1\}^{n_{k-1} \times n_k}$. The entry $(\mathbf{B}_k)_{\sigma_{k-1}, \sigma_k}$ represents the orientation of σ_{k-1} as a face of σ_k , or equals 0 when the two are not adjacent. For $k = 1$, the boundary map is the node to edge *graph incidence matrix*, i.e., $(\mathbf{B}_1)_{[a], [xy]} = 1$ if $a = x$, $(\mathbf{B}_1)_{[a], [xy]} = -1$ if $a = y$, and zero otherwise; for $k = 2$, each column of \mathbf{B}_2 contains the orientation of a triangle w.r.t. its edges. In other words, $(\mathbf{B}_2)_{[a,b], [x,y,z]} = 1$ if $[a, b] \in \{[x, y], [y, z]\}$, $(\mathbf{B}_2)_{[a,b], [x,y,z]} = -1$ if $[a, b] = [x, z]$, and 0 otherwise. In this paper, we will only work with simplices up to dimension $k = 2$. Closely related to *boundary map* is the *co-boundary map*. This operator is the adjoint of the *boundary map* and it maps a simplex to its co-faces, i.e., $\mathcal{B}^k : \mathcal{C}^{k-1} \rightarrow \mathcal{C}^k$. The corresponding *co-boundary matrix* is simply the transpose of the *boundary matrix*, i.e., \mathbf{B}_k^\top . Pseudocode for constructing \mathbf{B}_k can be found in Algorithm S1.

The discrete k -Laplacian The unnormalized k -Laplacian $\mathbf{L}_k = \mathbf{B}_k^\top \mathbf{B}_k + \mathbf{B}_{k+1} \mathbf{B}_{k+1}^\top$ was first introduced by [Eck44] as a discrete analog to Δ_k . One can verify that $\mathbf{L}_0 = \mathbf{B}_1 \mathbf{B}_1^\top$ represents the *unnormalized* graph Laplacian [Chu96]. To extend the aforementioned construction to a weighted

k -Laplacian, one can introduce a diagonal non-negative *weight matrix* \mathbf{W}_k of dimension n_k , with $(\mathbf{W}_k)_{[\sigma_k, \sigma_k]}$ being the weight for simplex σ_k . For unweighted k -Laplacians, \mathbf{W}_{k-1} , \mathbf{W}_k , \mathbf{W}_{k+1} are equal to the unit matrices. By analogy to the *random walk* graph Laplacian, [HJ13] define a (weighted) *random walk* k -Hodge Laplacian by $\mathcal{L}_k = \mathbf{B}_k^\top \mathbf{W}_{k-1}^{-1} \mathbf{B}_k \mathbf{W}_k + \mathbf{W}_k^{-1} \mathbf{B}_{k+1} \mathbf{W}_{k+1} \mathbf{B}_k^\top$. Of specific interest to us are the weighted Laplacians for $k = 0$ (graph Laplacian) and $k = 1$ (graph Helmholtzian). The operator $\mathcal{L}_0 = \mathbf{W}_0^{-1} \mathbf{B}_1 \mathbf{W}_1 \mathbf{B}_1^\top$ coincides with the *random walk* graph Laplacian [Chu96]. The Helmholtzian is defined as

$$\mathcal{L}_1 = a \cdot \underbrace{\mathbf{B}_1^\top \mathbf{W}_0^{-1} \mathbf{B}_1 \mathbf{W}_1}_{\mathcal{L}_1^{\text{down}}} + b \cdot \underbrace{\mathbf{W}_1^{-1} \mathbf{B}_2 \mathbf{W}_2 \mathbf{B}_2^\top}_{\mathcal{L}_1^{\text{up}}}. \quad (1)$$

Here a, b are non-negative constants which were usually set to 1 in the previous studies, we will show that $a = \frac{1}{4}$ and $b = 1$ in Section 4. Since \mathcal{L}_k is an asymmetric matrix, one can symmetrize it by $\mathcal{L}_1^s = \mathbf{W}_1^{1/2} \mathcal{L}_1 \mathbf{W}_1^{-1/2}$ while preserving the spectral properties [SBH⁺20]; \mathcal{L}_1^s is called the *symmetrized* or *renormalized* 1-Hodge Laplacian. For more information about the boundary map and k -Laplacian, please refer to [Lim20, HJ13, SBH⁺20].

$$\mathcal{C}_1 \simeq \mathbb{R}^{n_1} = \underbrace{\text{im} \left(\mathbf{W}_1^{1/2} \mathbf{B}_1^\top \right)}_{\text{gradient}} \oplus \underbrace{\text{ker} \left(\mathcal{L}_1 \right)}_{\text{harmonic}} \oplus \underbrace{\text{im} \left(\mathbf{W}_1^{-1/2} \mathbf{B}_2 \right)}_{\text{curl}}. \quad (2)$$

$\overbrace{\text{ker} \left(\mathbf{B}_2^\top \mathbf{W}_1^{-1/2} \right) = \text{ker}(\text{curl})}^{\text{ker}(\mathcal{L}_1)}$
 $\underbrace{\text{ker} \left(\mathbf{B}_1 \mathbf{W}_1^{1/2} \right) = \text{ker}(\text{gradient})}_{\text{ker}(\mathcal{L}_1)}$

(Normalized) Hodge decomposition This celebrated result expresses a vector field as the direct sum of a *gradient*, a *harmonic*, and a *rotational* vector field. The eigenvectors of the k -Laplacian, which span the vector space \mathcal{C}_k of k -chains, specifically form the bases of three different subspaces (the image of $\mathcal{L}_k^{\text{down}}$, the image of $\mathcal{L}_k^{\text{up}}$, and the kernel of both operators). Here, we mainly discuss the *normalized Hodge decomposition* defined by [SBH⁺20] for 0 or 1-cochains as well as the Laplacian operators \mathcal{L}_0 or \mathcal{L}_1^s ; but they can be generalized to higher order cochains and Laplacians. For $k = 0$ (graph Laplacian), the first term in the decomposition vanishes and we have only the decomposition of the null and image of \mathcal{L}_0 . As for $k = 1$ (Helmholtzian), one can obtain the decomposition as in (2). Here the symbols ker , im denote respectively the null space and image of an operator. For any 1-cochain $\omega \in \mathbb{R}^{n_1}$ we can write $\omega = \mathbf{g} \oplus \mathbf{r} \oplus \mathbf{h}$, with $\mathbf{g} = \mathbf{W}_1^{1/2} \mathbf{B}_1^\top \mathbf{p}$ the gradient, $\mathbf{r} = \mathbf{W}_1^{-1/2} \mathbf{B}_2 \mathbf{v}$ the curl, and \mathbf{h} the harmonic flow component. The flows \mathbf{g} , \mathbf{r} , \mathbf{h} can be estimated by least squares, i.e., $\hat{\mathbf{p}} = \text{argmin}_{\mathbf{p} \in \mathbb{R}^{n_0}} \|\mathbf{W}_1^{1/2} \mathbf{B}_1^\top \mathbf{p} - \omega\|^2$, $\hat{\mathbf{v}} = \text{argmin}_{\mathbf{v} \in \mathbb{R}^{n_2}} \|\mathbf{W}_1^{-1/2} \mathbf{B}_2 \mathbf{v} - \omega\|^2$, and finally $\hat{\mathbf{h}} = \omega - \mathbf{W}_1^{1/2} \mathbf{B}_1^\top \hat{\mathbf{p}} - \mathbf{W}_1^{-1/2} \mathbf{B}_2 \hat{\mathbf{v}}$.

k -Laplacian operators on manifolds These operators act on *differential forms* of order k [DKT08, Whi05], the continuous analogues to k -cochains. For instance, a 0-form is a scalar function, and an 1-form a vector field. The k -Hodge Laplacian is defined to be $\Delta_k := \mathbf{d}_{k-1} \delta_k + \delta_{k+1} \mathbf{d}_k = (\mathbf{d} + \delta)^2$. Similar to the discrete operator, Δ_k can be written as the sum of down k -Laplacian ($\Delta_k^{\text{down}} = \mathbf{d}_{k-1} \delta_k$) and up k -Laplacian ($\Delta_k^{\text{up}} = \delta_{k+1} \mathbf{d}_k$). The operators δ_k and \mathbf{d}_k , called respectively *exterior derivative* and *co-derivative* are the differential analogues of the boundary \mathbf{B}_k and co-boundary operators \mathbf{B}_{k-1} (definitions in Supplement C). The well-known Laplace-Beltrami operator is $\Delta_0 = \delta_1 \mathbf{d}_0$. For our paper, the main object of interest is the 1-Hodge Laplacian $\Delta_1 = \mathbf{d}_0 \delta_1 + \delta_2 \mathbf{d}_1$, also known as *Helmholtzian*. For $d = 3$, one has $\mathbf{d}_0 = \text{grad}$, and $\delta_1 = -\text{div}$, and \mathbf{d}_1 corresponds to curl. The vector Laplacian in 3D (coordinate-wise Δ_0) corresponds to Δ_1 , i.e., $\Delta_1 = -\nabla^2 = -\text{grad div} + \text{curl curl}$ [BNPB13]. For a 1-form $\zeta_1 = (f_1, \dots, f_d)$, the expression of $\Delta_1 \zeta_1$ in local coordinates can be found in Proposition S7 in Supplement D. In particular, if ζ is purely *curl* ($\mathbf{d}_0 \delta_1 \zeta = 0$) or *gradient flow* ($\delta_0 \mathbf{d}_1 \zeta = 0$), then $\Delta_1 \zeta$ is a coordinate-wise 0-Laplacian, i.e., $\Delta_1 \zeta \propto (\Delta_0 f_1, \dots, \Delta_0 f_d)$, as shown in Corollary S9 or in [Lee06].

3 Problem formulation and main algorithm

We now formally describe the aim of this work. Suppose we observe data $\mathbf{X} \in \mathbb{R}^{n \times D}$, with data points denoted by $\mathbf{x}_i \in \mathbb{R}^D \forall i \in [n]$, that are sampled from a smooth d -dimensional submanifold $\mathcal{M} \subset \mathbb{R}^D$; and the sampling density is uniform on \mathcal{M} . In this paper, a point on \mathcal{M} has two notations: \mathbf{x} is its \mathbb{R}^D coordinate vector, while x is the coordinate free point on \mathcal{M} . For instance, computations are always in \mathbb{R}^D coordinates; whereas V, E, T , and geodesics refer to the coordinate-free representations.

Algorithm 1: MANIFOLDHELMHOLTZIAN

Input : data $\mathbf{X} \in \mathbb{R}^{n \times D}$, radius δ , kernel bandwidth ε

- 1 $\text{SC}_2 = (V, E, T) \leftarrow \text{VRCOMPLEX}(\text{data} = \mathbf{X}, \text{max_dist} = \delta, \text{max_dim} = 2)$
- 2 $\mathbf{B}_1 = \text{BOUNDARYMAP}(V, E) \triangleright \text{Algorithm S1}$
- 3 $\mathbf{B}_2 = \text{BOUNDARYMAP}(E, T)$
- 4 $\mathbf{W}_2 \leftarrow \text{diag}\{w^{(2)}(t), t \in T\}$ as in (3)
- 5 $\mathbf{W}_1 \leftarrow \text{diag}\{|\mathbf{B}_2| \mathbf{W}_2 \mathbf{1}_{n_2}\}$
- 6 $\mathbf{W}_0 \leftarrow \text{diag}\{|\mathbf{B}_1| \mathbf{W}_1 \mathbf{1}_{n_1}\}$
- 7 $\mathcal{L}_1 \leftarrow \frac{1}{4} \mathbf{B}_1^\top \mathbf{W}_0^{-1} \mathbf{B}_1 \mathbf{W}_1 + \mathbf{W}_1^{-1} \mathbf{B}_2 \mathbf{W}_2 \mathbf{B}_2^\top \triangleright \text{Set } a = \frac{1}{4}; b = 1 \text{ in (1)}$
- 8 $\mathcal{L}_1^s \leftarrow \mathbf{W}_1^{1/2} \mathcal{L}_1 \mathbf{W}_1^{-1/2}$

Return : Helmholtzian \mathcal{L}_1 , symmetrized Helmholtzian \mathcal{L}_1^s

Our aim is to approximate Δ_1 by a suitably weighted Helmholtzian \mathcal{L}_1 on a 2-simplicial complex $\text{SC}_2 = (V, E, T)$, with nodes located at the data points. The steps of this construction are given in Algorithm 1. The first 3 steps produce the simplicial complex SC_2 and the boundary matrices $\mathbf{B}_1, \mathbf{B}_2$ from \mathbf{X} . There are multiple ways to build an SC_ℓ from point cloud data [OPT⁺17]; here the *Vietoris-Rips* (VR) [CM17] complex is used for its efficient runtime and natural fit with the chosen triangular kernel which will be described below. The VR complex is an *abstract simplicial complex* defined on the finite metric space. An ℓ -simplex σ_ℓ is included in the complex if all the pairwise distances between its vertices are smaller than some radius δ . The VR complex is a special case of the *clique complex*; one can easily build such complex from a δ -radius graph by including all the cliques in the graph. Note that a VR complex built from a point cloud dataset $\mathbf{X} \in \mathbb{R}^D$ cannot always be embedded in \mathbb{R}^D due to the possible crossings between simplices. For the VR 2-complex SC_2 constructed from a point cloud, the vertex set is the data \mathbf{X} , and two vertices are connected if they are at distance δ or less. A triangle t in SC_2 is formed when 3 edges of t are all connected. The edges E and triangles T are represented as lists of tuples of lengths n_1 and n_2 , respectively. From them, $\mathbf{B}_1, \mathbf{B}_2$ are constructed in linear time w.r.t. n_1 and n_2 . In the worst case scenario, one needs $n_1 = \mathcal{O}(n^2)$ in memory. Luckily, this is oftentimes a corner case due to the manifold assumption. The memory size can further be reduced by different approximation methods [DFW13, She13, KS13] in building SC_2 . We implemented Algorithm 1 in python. The SC_2 is built with `gudhi` [MBGY14]. Upon constructing the SC_2 , Algorithm S1 `BOUNDARYMAP` is implemented by `numba` [LPS15] to speed up the for-loop operation by multi-threading.

Steps 4–6 construct the weights matrices $\mathbf{W}_2, \mathbf{W}_1, \mathbf{W}_0$. The crucial step is the weighting of the triangles, which is described below. Once the weights of the triangles are given, the weights of the lower dimensional simplices are determined by the consistency conditions required by the boundary operator. It then follows that the weight of vertex $v \in V$ equals its degree $[\mathbf{W}_0]_{vv} = \sum_{e \in E} [|\mathbf{B}_1]_{ve}| [|\mathbf{W}_1]_{ee}$ and similarly, $[\mathbf{W}_1]_{ee} = \sum_{t \in T} [|\mathbf{B}_2]_{et}| [|\mathbf{W}_2]_{tt}$. Finally, \mathcal{L}_1 and \mathcal{L}_1^s are obtained by directly applying the definitions in Section 2.

The triangle kernel $w^{(2)}$ There are multiple choices of kernels, e.g., constant values on triangles [SBH⁺20], or weights based on \mathbf{B}_2^\top [GP10]. The former fails to capture the size and geometry of a triangle while the latter violates the assumption that we are building SC_2 from a point cloud. Here we introduce a kernel which weighs triangles by the product of the pairwise edge kernels.

$$w^{(2)}(\mathbf{x}, \mathbf{y}, \mathbf{z}) = \kappa(\mathbf{x}, \mathbf{y}) \cdot \kappa(\mathbf{x}, \mathbf{z}) \cdot \kappa(\mathbf{y}, \mathbf{z}) \text{ for } x, y, z \in T, \quad (3)$$

$$\text{where } \kappa(\mathbf{x}, \mathbf{y}) = \kappa(\|\mathbf{x} - \mathbf{y}\|^2 / \varepsilon^2).$$

with $\kappa(\cdot)$ any exponentially decreasing function. In this work, we use the exponential kernel $\kappa(u) = \exp(-u)$. With the aid of an exponentially decreasing function $\kappa(\cdot)$ in (3), one can filter

out structures that are topological noise in \mathcal{L}_1 , as we will show in Section 7. Note that there is a resemblance between (3) and the VR complex. By definition, a triangle x, y, z in the VR complex is formed if and only if $\mathbb{1}(\|\mathbf{x} - \mathbf{y}\| < \varepsilon)\mathbb{1}(\|\mathbf{y} - \mathbf{z}\| < \varepsilon)\mathbb{1}(\|\mathbf{z} - \mathbf{x}\| < \varepsilon)$ equals 1. Hence the VR complex itself is given by using $\kappa(u) = \mathbb{1}(u < 1)$ in (3).

Selecting the parameters ε and δ Asymptotically, as $n \rightarrow \infty$, the kernel widths corresponding to $\mathbf{W}_1, \mathbf{W}_2$ must decrease towards 0 at rates that are mutually compatible. The consistency analysis in Proposition 2 of Section 4 suggests a choice of $\varepsilon = \mathcal{O}(\delta^{\frac{2}{3}})$. From Section 4 we can also see that, since the down Helmholtzian is consistent if the corresponding graph Laplacian is consistent, one can choose δ by [JMM17]. A data-driven approach for choosing the ε parameter is currently lacking, and we leave it as future work.

Choice of a, b In Section 4, we will analyze separately the convergence of the up and down Laplacian, i.e., $\mathcal{L}_1^{\text{down}} \rightarrow a \cdot \Delta_1^{\text{down}}$ and $\mathcal{L}_1^{\text{up}} \rightarrow b \cdot \Delta_1^{\text{up}}$. From the proof, it follows that $a = \frac{1}{4}; b = 1$. Please refer to Supplement H for more details and discussions.

4 Consistency results for graph Helmholtzian

This section investigates the continuous limits of the discrete operators $\mathcal{L}_1^{\text{down}} = \mathbf{B}_1^\top \mathbf{W}_0^{-1} \mathbf{B}_1 \mathbf{W}_1$ and $\mathcal{L}_1^{\text{up}} = \mathbf{W}_1^{-1} \mathbf{B}_2 \mathbf{W}_2 \mathbf{B}_2^\top$. We assume the following for our analysis.

Assumption 1. *The data \mathbf{X} are sampled i.i.d. from a uniform density supported on a d dimensional manifold $\mathcal{M} \subseteq \mathbb{R}^D$ that is of class C^3 and has bounded curvature. W.l.o.g., we assume that the volume of \mathcal{M} is 1; and we denote by μ the Lebesgue measure on \mathcal{M} .*

Assumption 2. *The kernel $\kappa(\mathbf{x}, \mathbf{y})$ of $w^{(2)}(\mathbf{x}, \mathbf{y}, \mathbf{z})$ in (3) is of class C^3 and has exponential decay.*

We prove the pointwise consistency of $\mathcal{L}_1^{\text{up}}$ and $\mathcal{L}_1^{\text{down}}$; in addition, we also show the spectral consistency of $\mathcal{L}_1^{\text{down}}$ based on results for the spectral consistency of the related \mathcal{L}_0 .

Pointwise convergence of the up Laplacian $\mathcal{L}_1^{\text{up}}$ Let $\gamma(t)$ for $t \in [0, 1]$ be the geodesic curve connecting x, y with $\gamma(0) = \mathbf{x}, \gamma(1) = \mathbf{y}$, and $\dot{\gamma}(t) = d\gamma(t)/dt$. A 1-form (vector field) ζ on \mathcal{M} induces the 1-cochain ω on E by $\omega([x, y]) = \omega_{xy} = \int \zeta(\gamma(t))^\top \dot{\gamma}(t) dt$ for any edge $[x, y] \in E$. For notational simplicity, let $f_{xyz} = \omega_{xy} + \omega_{yz} + \omega_{zx}$. The goal is to show the consistency of $\mathcal{L}_1^{\text{up}}$ for a fixed edge $[x, y]$, i.e., to show that $\mathcal{L}_1^{\text{up}} \omega_{xy} \rightarrow c \int_0^1 (\Delta_1 \zeta)(\gamma(t))^\top \dot{\gamma}(t) dt$. First we obtain the discrete form of the unnormalized (weighted) up-Laplacian operating on a 1-cochain ω .

Lemma 1. *Let $\omega \in \mathbb{R}^{n_1}$ be a 1-cochain induced on SC_2 by vector field ζ . For any $x, y, z \in V$, we denote by $[x', y', z']$ the canonical ordering of the triangle $t \in T$ with vertex set $\{x, y, z\}$ (if one exists). Then, $[\mathbf{B}_2 \mathbf{W}_2 \mathbf{B}_2^\top \omega]_{[x, y]} = \sum_{z \in \{v \in V: [x', y', v'] \in T\}} w^{(2)}(\mathbf{x}, \mathbf{y}, \mathbf{z}) f_{xyz}$.*

Lemma 1 is proved in Supplement E.2. From Lemma 1, it is enough to consider *divergence free* 1-forms for the limit of $\mathcal{L}_1^{\text{up}}$, because $f_{xyz} = 0$ if ζ is curl free. The following proposition shows the asymptotic expansion for the integral form of $\sum_z w_T(\mathbf{x}, \mathbf{y}, \mathbf{z}) f_{xyz}$ (Lemma 1) when n is large.

Proposition 2. *If Assumptions 1–2 hold, v is of class $C^4(\mathcal{M})$, then*

$$\int_{\mathcal{M}} w_T(\mathbf{x}, \mathbf{y}, \mathbf{z}) f_{xyz} d\mu(\mathbf{z}) = \frac{2}{3} \varepsilon^{2+d} C_2 \int_0^1 [\delta dv(\gamma_{\mathcal{M}}(t))]^\top \dot{\gamma}'_{\mathcal{M}}(t) dt + \mathcal{O}(\varepsilon^{4+d}) + \mathcal{O}(\varepsilon^{d+2} \delta^2) + \mathcal{O}(\varepsilon^d \delta^3). \quad (4)$$

with $C_2 = \varepsilon^{-(4+d)} \int_{\mathbf{z} \in \mathbb{R}^d} \kappa^2(\frac{\|\mathbf{z}\|^2}{\varepsilon^2}) \mathbf{z}_1^2 \mathbf{z}_2^2 d\mathbf{z}$ and z_i representing the i -th coordinate of \mathbf{z} .

Sketch of proof. We first prove the case when $\mathcal{M} = \mathbb{R}^d$ (Lemma S12). Consider a triangle $[x, y, z] \in T$, where z will be integrated over. We parametrize the path segments $x \rightarrow y, y \rightarrow z$, and $z \rightarrow x$ by $\mathbf{u}(t), \mathbf{v}(t)$, and $\mathbf{w}(t)$, respectively. By changing the variables from $\mathbf{w}(t)$ and $\mathbf{v}(t)$ to $\mathbf{u}(t)$, we express all three line integrals as integrals along the segment $[x, y]$. Next, when $\mathcal{M} \subseteq \mathbb{R}^D$, we bound the error terms of approximating the integration from \mathcal{M} to the tangent plane $\mathcal{T}_{\mathbf{x}} \mathcal{M}$ at \mathbf{x} with $\mathcal{O}(\varepsilon^4)$ in Lemma S13. Combining this Lemma with Lemma S12 concludes the proof. ■

Proposition 2 implies δ should decay faster than ε . So one can choose $\delta = \mathcal{O}(\varepsilon^{3/2})$. Now we can analyze the pointwise bias of the estimator.

Theorem 3. *Under the assumptions of Proposition 2, let $\delta = \mathcal{O}(\varepsilon^{3/2})$, then, for any fixed $x, y \in \mathcal{M}$, we have*

$$\mathbb{E} [(\mathcal{L}_1^{\text{up}})_{[x,y]}] = \frac{2}{3} \varepsilon^2 \frac{C_2}{C_0} \int_0^1 [\delta \text{d}v(\gamma_{\mathcal{M}}(t))]^\top \gamma'_{\mathcal{M}}(t) \text{d}t + \mathcal{O}(\varepsilon^4) + \mathcal{O}(\varepsilon^2 \delta n^{-1}). \quad (5)$$

where we define $C_0 = \frac{1}{\varepsilon^d} \int_{\mathbf{z} \in \mathbb{R}^d} \exp\left(-\frac{2\|\mathbf{z}\|^2}{\varepsilon^2}\right) \text{d}\mathbf{z}$. In the above, the expectation is taken over samples \mathbf{X} of size n , to which the points \mathbf{x}, \mathbf{y} are added.

Sketch of proof. The proof follows from the *Monte Carlo* approximation [NLCK06, BS19] of the RHS of Lemma 1, i.e.,

$$\mathbb{E} \left[\frac{1}{n} \sum_{\mathbf{z}} w_T(\mathbf{x}, \mathbf{y}, \mathbf{z}) f_{xyz} \right] = \int_{\mathcal{M}} w_T(\mathbf{x}, \mathbf{y}, \mathbf{z}) f_{xyz} \text{d}\mu(\mathbf{z}).$$

Combining the result of Proposition 2 (the ε bias) and the standard ratio estimator (the n^{-1} bias) completes the proof. The proof details are in E.4. ■

Note that the rate for ε for the Δ_0 estimator (\mathcal{L}_0) is slower than n^{-1} , see e.g., [Sin06, BS19]. One can thus drop the n^{-1} term in (5) using the similar bandwidth parameter as the Δ_0 estimator.

Pointwise convergence of the down Laplacian $\mathcal{L}_1^{\text{down}}$ For the pointwise convergence of the down Helmholtzian, the following proposition shows the asymptotic expansion for the integral when n is large

Proposition 4. *If Assumptions 1–2 hold, v is of class $C^4(\mathcal{M})$, then*

$$\begin{aligned} & \int_{\mathbf{z} \in \mathcal{M}} (w_E(\mathbf{y}, \mathbf{z}) f_{yz} - w_E(\mathbf{x}, \mathbf{z}) f_{xz}) \text{d}\mathbf{z} \\ &= \frac{8}{3} \varepsilon^{2d+2} C_0 C_1 \int_0^1 (\text{d}\delta v)(\gamma'_{\mathcal{M}}(t))^\top \gamma'_{\mathcal{M}}(t) \text{d}t + \mathcal{O}(\varepsilon^{4+2d}) + \mathcal{O}(\varepsilon^{1+2d} \delta^2), \end{aligned} \quad (6)$$

where $\int_{\mathbf{z} \in \mathbb{R}^d} \exp\left(-\frac{\|\mathbf{z}-\mathbf{x}\|^2}{2\varepsilon^2}\right) (\mathbf{z}-\mathbf{x})_j^2 \text{d}\mathbf{z} = 4\varepsilon^{d+2} C_1$.

With this proposition, now we can analyze the pointwise convergence of the down Helmholtzian

Theorem 5. *Under the assumptions of Proposition 4, let $\delta = \mathcal{O}(\varepsilon^{3/2})$, then, for any fixed $x, y \in \mathcal{M}$, we have*

$$\mathbb{E} [(\mathcal{L}_1^{\text{down}})_{[x,y]}] = \frac{2}{3} \varepsilon^2 \frac{C_1}{C_0} \int_0^1 [\text{d}\delta v(\gamma_{\mathcal{M}}(t))]^\top \gamma'_{\mathcal{M}}(t) \text{d}t + \mathcal{O}(\varepsilon^4) + \mathcal{O}(\varepsilon \delta^2) + \mathcal{O}(n^{-1} \varepsilon^2 \delta). \quad (7)$$

In the above, the expectation is taken over samples \mathbf{X} of size n , to which the points \mathbf{x}, \mathbf{y} are added.

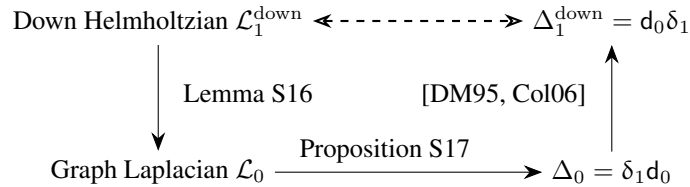


Figure 1: Outline of the (spectral) consistency proof of $\mathcal{L}_1^{\text{down}}$.

Spectral consistency of the down Laplacian $\mathcal{L}_1^{\text{down}}$ The proof for spectral consistency of the 1 down-Laplacian is outlined in Figure 1. In short, by linking the spectra/eigenforms of Δ_1^{down} to Δ_0 as well as their discrete counterparts (two vertical arrows), one can show the consistency of $\mathcal{L}_1^{\text{down}}$ (horizontal dashed line) using the known spectral convergence of the discrete graph Laplacian \mathcal{L}_0 to

the the Laplace-Beltrami operator Δ_0 [CL06, BS19] (horizontal solid arrow). The details and proofs are in Supplement G.

Here we have derived the continuous operator limits of the up and down Laplacian terms. We have shown that $\mathcal{L}_1^{\text{down}}$ converges to (a constant times) Δ_1^{down} spectrally. For $\mathcal{L}_1^{\text{up}}$ and $\mathcal{L}_1^{\text{down}}$, we have shown that the pointwise limit exists, and that it equals Δ_1^{up} and Δ_1^{down} multiplied with a constant.

Since the limits of $\mathcal{L}_1^{\text{up}}$ and $\mathcal{L}_1^{\text{down}}$ have different scalings, the estimator \mathcal{L}_1 of Δ_1 is a weighted sum of the two terms with coefficients a, b as in (1). From (S23), we use $a = \frac{1}{4}; b = 1$ based on the pointwise limit, and empirical observations on the synthetic datasets validate it. Please refer to Section 7 and Supplement H for more details.

5 Related works and discussion

Consistency results of Laplace type operators on a manifold Numerous *non-linear dimensionality reduction* algorithms from point cloud data, e.g., [CL06, BN07, THJ10], investigated the consistency of functions (0-forms) on \mathcal{M} . Spectral exterior calculus (SEC) [BG20] extended the existing consistency results of 0-forms to 1-forms by building a frame (overcomplete set) to approximate the spectrum of Δ_1 from \mathcal{L}_0 . The SEC only has $\mathcal{O}(n^3)$ dependency in computing the eigenvectors of \mathcal{L}_0 . Therefore, it is well-suited for topological feature discovery when large number of points are sampled from \mathcal{M} . Nevertheless, the algorithm involves several fourth order *dense* tensor computations with size m , the number of the eigenvectors of 1-Laplacian to estimate, and results in a $\mathcal{O}(m^4)$ dependency in memory and $\mathcal{O}(m^6)$ in runtime. These dependencies may cause difficulties in applying SEC to the edge flow learning scenarios in real datasets, since higher frequency terms of the 1-Laplacian are oftentimes needed ($m \geq 100$). On the other end, [SW11] studied the discrete approximation of the *Connection Laplacian*, a differential operator acting on tensor bundles of a manifold. This is intrinsically different from the 1 Hodge Laplacian we discussed.

Random walks on discrete k -Laplacian operator [SBH⁺20] studied random walks on the edges of normalized 1-Hodge Laplacian of the pre-determined graph. For points sampled from \mathcal{M} , they proposed an *ad hoc* hexagonal binning method to construct the SC_2 from the trajectories; theoretical aspects of the binning method were not discussed. On the theoretical front, frameworks of random walks on simplices of down [MS16] and up [PR17] k -Laplacian have also been visited. These works focused on the connection between random walks on a simplicial complex and spectral graph theory. Our graph Helmholtzian \mathcal{L}_1^s based on pairwise triangle weights makes it possible to extend their frameworks to the point cloud datasets.

Persistent homology Persistent Homology (PH) theory enables us to study the topological features of a point cloud in multiple spatial resolutions. The direct application of PH is the estimation of the k -th Betti number, i.e., the number of k dimensional *holes*, from $\mathbf{X} \subseteq \mathcal{M}$. PH algorithms applied to real data typically output large numbers of k -holes with low persistences. Therefore, one selects the statistically significant topological features by some bootstrapping-based methods, e.g., the quantile of the *bottleneck distances* between estimated *persistent diagram* (PD) and the bootstrapped PDs. Readers are encouraged to refer to [Was18, CM17] for more details. The PH theories are powerful in finding β_k when $k \geq 2$; in contrast, the Laplacian based methods are found effective in edge flow learning and smoothing for their abilities to keep track of the orientations (see Section 6).

Edge flow learning [JSSB19] proposed a graph based edge flow SSL algorithm for divergence free flows using the unnormalized down-Laplacian $\mathbf{B}_1^\top \mathbf{B}_1$. Another method, [GR13], transforms the edge data into node space via line graph transformation; the problem is thus turned into a vertex based SSL and solved by well studied tools, e.g., [ZGL03, BNS06]. These algorithms assume the data is a graph, and therefore special techniques are needed to convert the point clouds to graphs. Moreover, both methods are designed for flows that are (approximately) divergence free. We provide experimental evaluations of these algorithms in Supplement K.

6 Applications of the constructed graph Helmholtzian

k -th Betti number The spectrum of \mathcal{L}_1 contains information about the manifold topology. Since $\mathbf{B}_k \mathbf{B}_{k+1} = 0$ [Lim20], $\text{im}(\mathbf{B}_{k+1})$ is a subspace of $\ker(\mathbf{B}_k)$. One can define the k -th homology vector space \mathcal{H}_k as the space of k dimensional simplices that are not the face of any $k + 1$ -simplex in SC_ℓ . In mathematical terms, $\mathcal{H}_k := \ker(\mathbf{B}_k) / \text{im}(\mathbf{B}_{k+1})$. The dimension of the k -th homology space, or the number of the k dimensional *holes*, is defined to be the k -th *Betti number* β_k . It can be shown that β_k is the dimension of the null space of k -th Laplacian, i.e., $\beta_k = \dim(\ker(\mathbf{L}_k))$. Note that $\beta_0 = \dim(\ker(\mathbf{L}_0))$, the number of zero eigenvalues of the graph Laplacian, corresponds to the number of connected components in the graph. Similarly, β_1 , the dimension of the null space of the Helmholtzian, represents the number of loops in SC_ℓ (for $l \geq 2$). The k -th Betti number β_k can also be obtained from the *random walk* k Laplacian \mathcal{L}_k as $\beta_k = \dim(\ker(\mathcal{L}_k))$, or by persistent homology (PH) theories [Was18, CM17].

Edge flow smoothing and graph signal processing from point cloud data The graph Laplacian has long been used in node-based signal smoothing on graphs [OFK⁺18]. [SS18] proposed an edge flow smoothing algorithm using only the *unnormalized down Laplacian* $\mathbf{L}_1^{\text{down}} = \mathbf{B}_1^\top \mathbf{B}_1$. These ideas apply naturally to the regularization with \mathcal{L}_1^s as follows. The smoothed flow $\hat{\omega}$ is obtained by projecting the noisy flow ω to the low frequency eigenspace of \mathcal{L}_1^s , i.e., by solving the damped least squares problem

$$\hat{\omega} = \underset{\mathbf{v}}{\text{argmin}} \|\mathbf{v} - \omega\|^2 + \alpha \mathbf{v}^\top \mathcal{L}_1^s \mathbf{v}. \quad (8)$$

The optimal solution to the aforementioned minimization problem is $\hat{\omega} = (\mathbf{I}_{n_1} + \alpha \mathcal{L}_1^s)^{-1} \omega$. Note that the $\mathbf{L}_1^{\text{down}}$ -based smoothing algorithm proposed by [SS18] would fail to filter noise in the *curl* space, for curl flows are in the space of $\ker(\mathbf{L}_1^{\text{down}})$. In contrast, the proposed algorithm can successfully smooth out the high frequency noise in either the *curl* or the *gradient* spaces by using the weighted Laplacian \mathcal{L}_1^s , which encodes the information from both the up and down Laplacians.

Semi-supervised edge flow learning by 1-Laplacian regularizer Similar to the SSL by *Laplacian Regularized Least Squares* (LaplacianRLS) on 0-forms (node-based SSL) [BNS06], here we propose a framework for SSL on discrete 1-cochains (edge-based SSL). Define the kernel between two edges to be $\mathcal{K}(e_i, e_j) = 1$ if e_i, e_j share the same coface (triangle) or face (node), and 0 otherwise. Let \mathfrak{H} be the corresponding reproducing kernel Hilbert space (RKHS). Given the set of known edges $S \subset [n_1]$ (training set), we optimize over edge flows $g \in \mathfrak{H}$ with the loss function

$$\frac{1}{|S|} \sum_{e \in S} (g(e) - \omega_e)^2 + \lambda_1 \|g\|_{\mathfrak{H}}^2 + \frac{\lambda_2}{n_1^2} g^\top \mathcal{L}_1^s g. \quad (9)$$

From the *representer theorem*, the optimal solution is $g^*(e) = \sum_{e' \in E} \alpha_{e'}^* \mathcal{K}(e', e)$, with $\alpha^* = \left(\text{diag}(\mathbf{1}_S) \mathcal{K} + \lambda_1 |S| \mathbf{I}_{n_1} + \frac{\lambda_2 |S|}{n_1^2} \mathcal{L}_1^s \mathcal{K} \right)^{-1} \omega$, where \mathcal{K} is a $n_1 \times n_1$ kernel matrix with $[\mathcal{K}]_{e_i, e_j} = \mathcal{K}(e_i, e_j)$. A possible extension of the proposed \mathcal{L}_1 -RLS is to use HHD as in (2). More specifically, the eigenspace of \mathcal{L}_1 can be decomposed into two subspaces corresponding to the gradient and curl spaces, respectively. One can weight differently the importance between $\mathcal{L}_1^{\text{up}}$ and $\mathcal{L}_1^{\text{down}}$. To achieve this, we apply a slight change to the second regularization term, i.e., $\frac{\lambda_2^{\text{up}}}{n_1^2} g^\top \mathcal{L}_1^{s, \text{up}} g + \frac{\lambda_2^{\text{down}}}{n_1^2} g^\top \mathcal{L}_1^{s, \text{down}} g$. We call the proposed variant UpDownLaplacianRLS, which will become to LaplacianRLS if $\lambda_2^{\text{down}} = \lambda_2^{\text{up}}$. Note that it is possible to extend other variants of node-based SSL algorithms (e.g., the label propagation algorithm [ZG02] for classification) to edge-based SSL; or introduce more powerful kernels \mathcal{K} that capture the orientations and similarities of edges. Here we simply use manifold regularization regression with a simple binary \mathcal{K} to illustrate the effectiveness of the proposed Helmholtzian.

7 Experiments

We demonstrate the proposed manifold Helmholtzian construction and its applications to edge flow learning (SSL and smoothing) on four synthetic datasets: *circle*, *torus*, *flat torus*, and *2 dimensional strip*. Additionally, we analyze several real datasets from chemistry, oceanography, and RNA single

cell sequencing. All datasets are described in Supplement J. We use $a = \frac{1}{4}$; $b = 1$ everywhere, except in the experiments involving UpDownLaplacianRLS, where the scaling constants are set by cross validation.

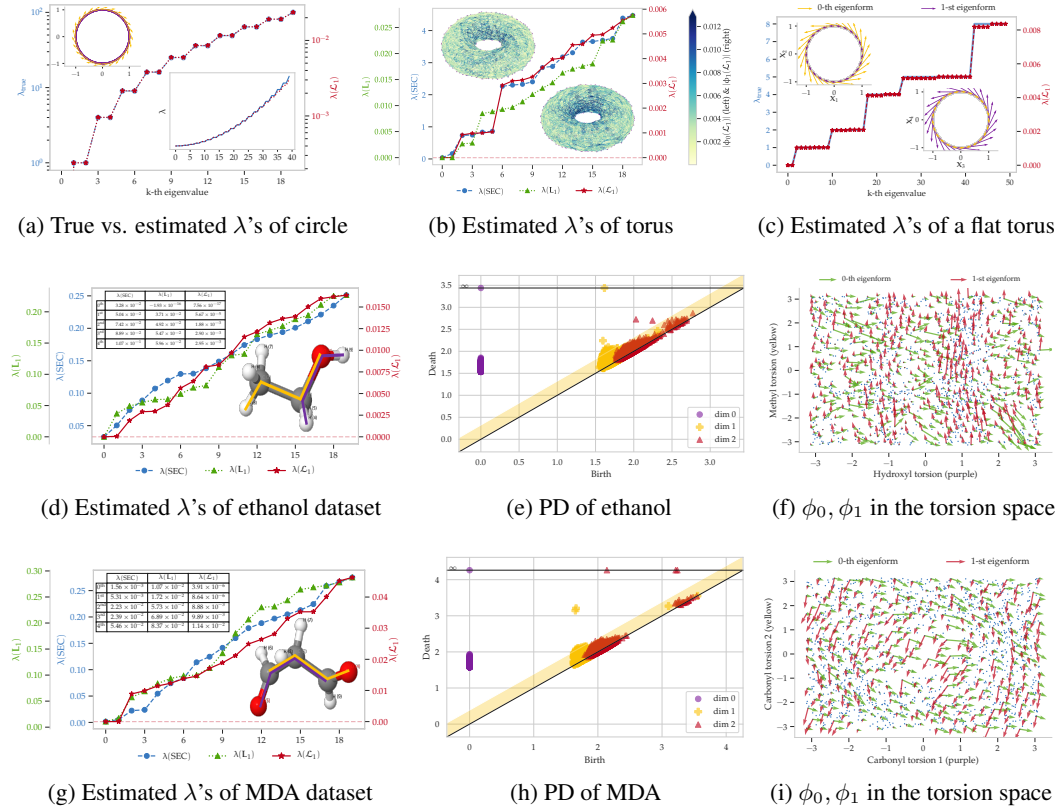


Figure 2: The first Betti number β_1 estimation for the synthetic manifolds (first row, left to right are unit circle, torus, and flat torus), ethanol (second row), and malondialdehyde (third row) datasets. The estimated harmonic eigenforms of the synthetic datasets can be found in the inset plots of (a–c). Readers are encouraged to zoom in on these plots for better views of the vector fields and cochains. For the second and the third row, subfigures from left to right correspond to the estimated λ 's from different methods, persistent diagram of the point cloud data, and the two harmonic flows in the torsion space, respectively.

7.1 Dimension of loop space β_1

For the first Betti number β_1 , we report the eigenvalues of Δ_1 estimated by SEC [BG20] (in blue), unweighted random walk Laplacian by letting $\mathbf{W}_2 = \mathbf{I}_{n_2}$ (green curve in Figure 2), and the proposed weighted 1-Laplacian \mathcal{L}_1 (in red). Betti numbers can also be estimated from a *Persistence Diagram* (PD). We present the PD with 95% confidence interval estimated from 7,000 bootstrap samples (see also [Was18] and Algorithm S3) for two chemistry datasets, i.e., the ethanol and malondialdehyde (MDA) data. All experiments are replicated at least 5 times with very similar results. The eigenvalues of the circle Δ_1 are $\lambda_k = (\lceil k/2 \rceil)^2$ for $k = 0, 1, \dots$. In Figure 2a we overlay the ground truth eigenvalues (blue) and the estimated eigenvalues (red) in log scale. The zeroth eigenvalue of \mathcal{L}_1^s is close to zero, and therefore is clipped from the plot. The lower right inset plot shows the first 40 eigenvalues in linear scale. The spectrum started to diverge when $k \approx 30$. The upper left inset plot is the original data (purple) and the estimated vector field¹ (yellow arrow) corresponding to the first eigenflow, which is a harmonic flow. Figure 2b shows the computed eigenvalues of different

¹To estimate a vector field from a 1 co-chain, one can solve a linear system as in (S45) in Supplement I in the Least-Squares sense.

algorithms on the synthetic torus dataset. A torus has two 1 dimensional loops. The first two eigenvalues of \mathbf{L}_1 or \mathcal{L}_1 are close to zero, but the null space estimated by SEC has dimension 1. Inset plots show the SC_2 edges colored with the intensity of the first two eigenflows of \mathcal{L}_1 , indicating that the first eigenflow (upper left) is along the outer (bigger) circle while the second eigenvector (lower right) belongs to the inner (smaller) circle. Figure 2c shows the first fifty estimated spectrum (red) of the flat torus dataset overlaid with the ground truth (blue). The first two eigenflows correspond to harmonic flows ($\beta_1 = 2$). The spectrum of *flat torus* is piecewise constant, with half of the eigenflows for each distinct eigenvalue corresponding to gradient and the other half to curl flows. The two inset plots present the first two harmonic flows in the original space, which are shown to be parameterizing two different loops in the flat torus.

The second row of Figure 2 shows the experiment on the ethanol dataset, whose ambient and (estimated) intrinsic dimension are $D = 102$ and $d = 2$, respectively. The dataset is known to be a noisy non-uniformly sampled torus (see e.g., Figure S5a) with the second (inner) loop difficult to detect due to an asymmetric topological structure. The two harmonic eigenflows correspond to the relative rotations of the Hydroxyl (purple) and Methyl (yellow) functional groups as shown in the inset plot of Figure 2d. To remove the non-uniformity effect, we subsample $n = 1,500$ points that are farthest to each other. However, as shown in Figure S5a, the non-uniformity sampling effect is still drastic. For this dataset, only the spectrum of the proposed Helmholtzian \mathcal{L}_1 captures the correct $\beta_1 = 2$, which can be confirmed in Figure 2d (see Supplement J.2 for the discussion on the first 10 eigenflows); by contrast, SEC, \mathbf{L}_1 and the PD estimate β_1 to 1, 1, and more than 2, respectively. Due to the proposed triangle weight as in (3), one can successfully remove the topological noise while preserving the true signal (smaller inner loop) in the weighted \mathcal{L}_1^s . Without the weighting function with exponential decay, the SEC and \mathbf{L}_1 fail to detect the second inner loop thus reporting $\beta_1 = 1$. Apart from β_1 , one can also obtain estimates of the two harmonic eigenflows from the first two eigenvectors of \mathcal{L}_1^s . These two harmonic flows correspond to the two independent loops of this manifold. The first two eigenforms estimated from the eigenvectors cochain can be found in Figures S5a and S5b in Supplement. With our prior knowledge that the purple and yellow rotors parametrize the loops in the dataset, we map the two eigenforms that reside in the PCA space \mathbf{X} to the torsion space using (S47) (see more discussions in Supplement I.3) as illustrated in Figure 2f. As clearly shown in the figure, the zeroth eigenform (green) aligns with the direction of increase of the Hydroxyl rotor (purple in the inset of 2d), while the first eigenform (red) matches perfectly with the derivative of Methyl rotor (yellow in the inset of 2d). Note also that one can clearly see the non-uniform sampling effect in Figure 2f. More specifically, more points are sampled when Hydroxyl torsion value is around -1 or 1 compared to other values.

The third row of Figure 2 shows the β_1 estimation result on the MDA dataset. This dataset has similar topological structure as the ethanol dataset; that is to say, they are both non-uniformly sampled tori. The two loops are parametrized by the two Carbonyl bond torsions as illustrated in the inset plot of Figure 2g. Compared to the ethanol dataset, the MDA dataset is easier in a sense that the two loops are more symmetric to each other. However, this dataset is harder to visualize for the torus is embedded in a 4 dimensional space. A clear separation between the zeroth and the first eigenvalues of \mathcal{L}_1 can be seen in the estimated spectrum (Figure 2d, see also the inset table) with the help of triangle weights (3). Even though the estimated dimensions of the null space of SEC and \mathbf{L}_1 are both two, we do not observe such clear gaps between the first two estimated eigenvalues compared to that of \mathcal{L}_1 . The bootstrapped PD with 95% confidence interval shows that there are at least two loops. However, statistically significant loops generated by the topological noise, which are close to the diagonal of the PD, are still visible. Similar to the ethanol dataset, we map the first two eigenforms to the two Carbonyl torsion space, as shown in Figure 2i. It confirms our prior knowledge that these two eigenforms parametrize the yellow and the purple torsions.

7.2 Edge flow prediction by semi-supervised learning

For each of the datasets in Figure 3, we construct the $\mathcal{L}_1^{\text{up}}$, $\mathcal{L}_1^{\text{down}}$, and the symmetrized Laplacian \mathcal{L}_1^s as described in Section 6. We then predict the flows on a fraction of the edges (test set) from the flows of the remaining edges (training set), with edges randomly split into train and test set, for train set ratio ranges from 0.05 to 0.95. We report the coefficient of determination, R^2 , as our performance metrics. The hyperparameters (all in range $[10^{-5}, 10^5]$) of the LaplacianRLS (in purple) and UpDownLaplacianRLS (in yellow) on the 2D strip and ocean datasets are selected by a 5-fold cross validation (CV) for each train/test split. To reduce the computation time, the hyperparameters

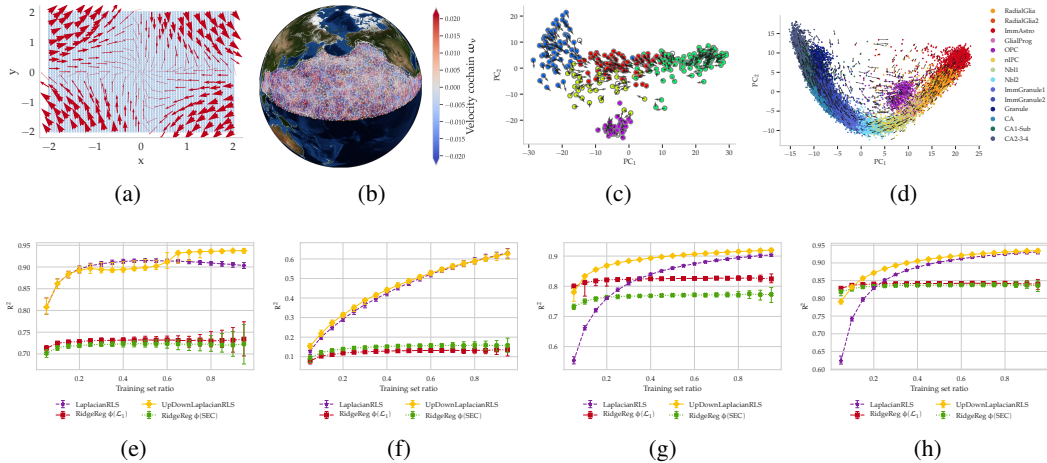


Figure 3: Edge flow SSL results for (columns from left to right) synthetic field on 2D strip, velocity field of ocean buoy, RNA velocity field of the chromaffin cells, and RNA velocity of the mouse hippocampus cell differentiation dataset. The first row is the velocity field/1-cochain overlaid on the original point cloud data, while the second row represents the R^2 score of different edge flow SSL algorithms.

for the larger datasets (RNA velocity datasets) are chosen by a 5-fold CV when the train set ratio is 0.2, and are used for all the other train sample sizes. Two other baselines are ridge regression on the first 100 eigenvectors estimated by \mathcal{L}_1^s (in red) and by SEC (in green). The ℓ_2 regularization parameter (in range $[10^{-5}, 10^5]$) for these two baselines is chosen by a 5-fold CV for different train set size. The experiments are repeated fifty times and we report the median R^2 value. The lower and upper error bars correspond to the 5th and 95th percentile of the R^2 values for different train/test split, respectively.

Figure 3e shows the results of predicting the simple synthetic field shown in Figure 3a, which composed of 70% curl flow and 30% gradient flow. The results of ridge regression on the low frequency eigenvectors indicate that 100 eigenvectors estimated by either \mathcal{L}_1^s (red) or SEC (green) are not enough even for predicting a simple field in Figure 3a.

The first real dataset we used contains ocean buoy trajectories across the globe.² The ambient dimension of the data is $D = 3$ (earth surface) and intrinsic dimension is $d = 2$. In this paper we subsample $n = 1,500$ farthest buoys located in the North Pacific ocean. The SC_2 is constructed in the *earth-centered, earth-fixed* (ECEF) coordinate system. Supplement J.3 has more details about the data and how to preprocess the edge flow. Figure 3b shows the constructed SC_2 of the buoys, with edges colored by the velocity cochain ω . Figure 3f reports the R^2 scores of the edge flow prediction. As clearly shown in the plot, higher frequency terms are needed to successfully predict the edge flow. However, this is clearly infeasible using the SEC approach as discussed in Section 5.

Next, we investigate the edge flow SSL on the RNA single cell sequencing manifold equipped with the RNA velocity [LMSZ⁺18]³, as shown in the third and the fourth column of Figure 3. These datasets have non-trivial manifold structures, which make the SSL problem more challenging. The Chromaffin cell differentiation dataset has $n = 384$ and $D = 5$, while the mouse hippocampus dataset has 18,140 cells in total and $D = 10$ in the PCA space. We subsample the farthest $n = 800$ cells in the mouse hippocampus while using all the cells in the chromaffin dataset. The RNA velocity fields of the Chromaffin and the mouse hippocampus datasets in the first two principal components are presented in Figure 3c and 3d, respectively. As expected, the LaplacianRLS and UpDownLaplacianRLS algorithms outperform the SSL algorithms using only low frequency terms of the estimated Δ_1 . Note also that compared with the SSL in the simple manifold structure in the first two columns, the UpDownLaplacianRLS for the RNA velocity data has more performance gains when the training set sizes are small.

²Data from the AOML/NOAA Drifter Data Assembly <http://www.aoml.noaa.gov/envids/gld/>

³All RNA datasets are from <http://velocityto.org> (with preprocessing codes)

7.3 Inverse problem: estimate the underlying velocity field from the trajectory data using SSL

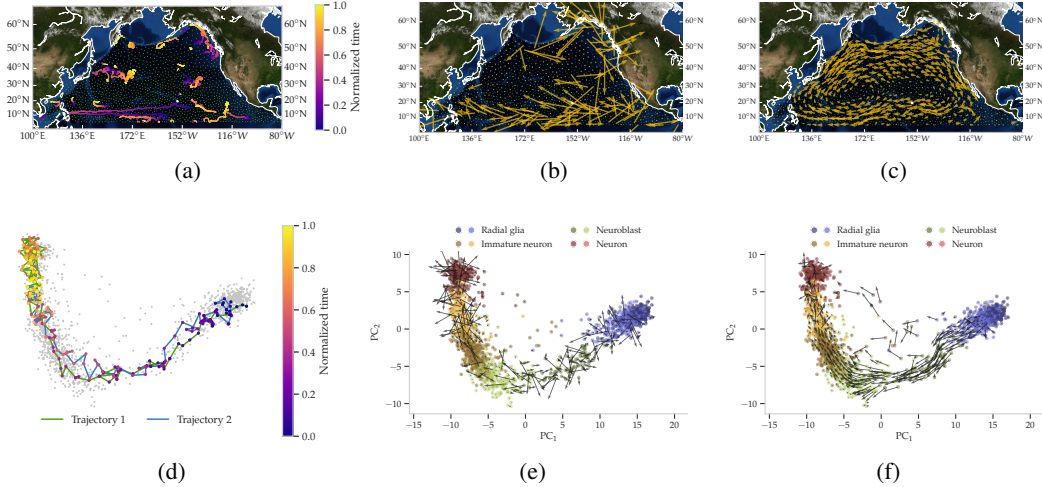


Figure 4: Results of estimating underlying velocity field from the partially observed trajectories. The first and second row are the ocean and the human glutamatergic neuron cell differentiation dataset, respectively. Columns from left to right present the observed trajectories, the estimated velocity field from a zero-padded 1-cochain, and the estimated field from the SSL interpolated 1-cochain.

One application of the Edge flow SSL is to estimate the underlying velocity field given a sparse set of observations (trajectories). A trajectory can be thought of as a partially observed 1-cochain with the value of $e = (i, j)$ constructed by counting number of times the trajectory goes from node i to node j (counted as negative if pass from j to i). We use the UpDownLaplacianRLS algorithm described in Section 6 and show the estimated fields from the interpolated 1-cochains in Figure 4. The parameters of the SSL algorithm are chosen using a 5-fold CV when test set ratio is 0.6 of all the observed edges. For comparison, we also present the velocity fields estimated by the zero-padded 1-cochains. The ocean drifter data themselves are trajectories, we sampled 20 trajectories from the dataset as shown in Figure 4a. Since we subsample the furthest $n = 1,500$ points from the original dataset to construct the $SC_2 = (V, E, T)$, the trajectories will contain points that are not in the vertex set V . To address this issue, one can treat the vertex set V as landmarks of the original dataset and map each point in the sampled trajectories to its nearest point in V . The 1-cochain is then constructed from the mapped trajectories. The figure shows that we can obtain a highly interpretable velocity field that corresponds to the North pacific Gyre as in Figure 4c, compared with the estimated velocity field from the zero-padded 1-cochain (Figure 4b). The algorithm is surprisingly powerful in the sense that the sampled trajectories do not even cover the west-traveling buoys at 40° N nor the south-bounding drifters near the west coast of the U.S.

The human glutamatergic neuron cell differentiation dataset do not have the temporal information. To illustrate our method, we estimate the transition probability matrix of a Markov chain from the RNA velocity field, which is computed from a 550-nearest neighbor (NN) graph. We then sampled two random walk trajectories (Figure 4d) from the constructed Markov chain on the 550-NN graph. Note that the k -NN graph above, which is used to estimate the RNA velocity field, can be different from the 1-skeleton of the SC_2 constructed in Algorithm 1. The estimated field using the UpDownLaplacianRLS in Figure 4c shows a smooth velocity field compared with the field estimated from the zero-padded 1-cochain in Figure 4b.

7.4 Edge flow smoothing

Figure 5 shows the result $\hat{\omega}$ of edge flow smoothing presented in (8). Figure 5a and 5b–5d show the original and the smoothed vector fields with different smoothing parameters α , respectively. Several patterns, e.g., North Equatorial and Kuroshio currents, are visible in the original velocity field. However, a well known North Pacific current at 40° N is not as apparent as the aforementioned currents. By contrast, the smoothed flow with $\alpha = 50$ makes the North Pacific Gyre visible. The

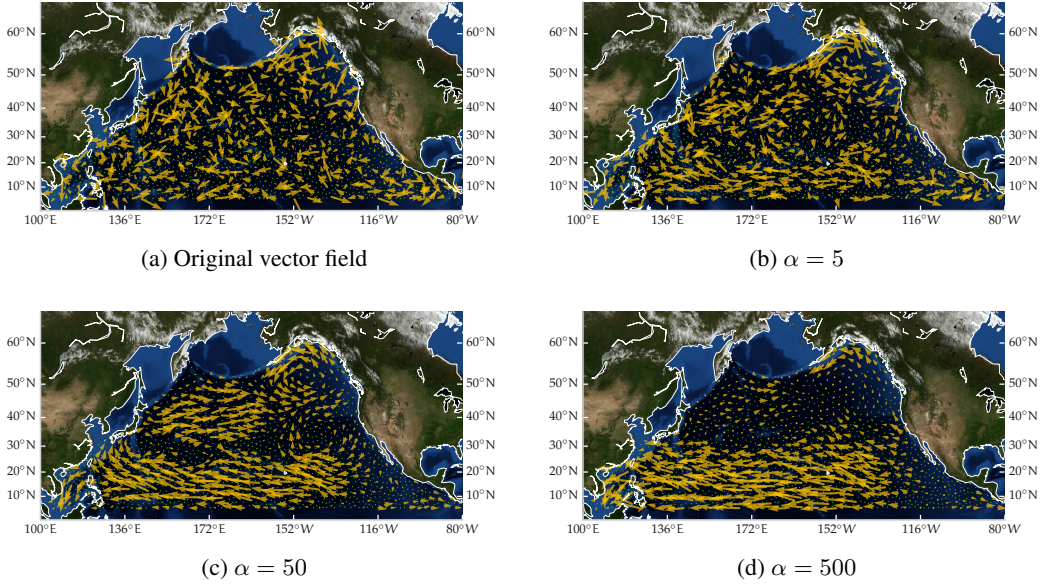


Figure 5: Edge flow smoothing on the ocean buoys velocity field dataset with different smoothing constant α .

model with $\alpha = 5$ in Figure 5b corresponds to the case of “under-smoothing”, while that with $\alpha = 500$ represents the case of “over-smoothing”. Note that the vector fields are plotted on the Mercator projection purely for visualization purposes. The SC_2 are constructed on the ECEF system similar as before.

8 Conclusion

The main contribution of the paper is to (i) propose an estimator of the Helmholtzian Δ_1 of a manifold in the form of a weighted 1-Laplacian of a two dimensional simplicial complex SC_2 , whose vertex set includes points sampled from a manifold. With the proposed kernel function for triangles, which is a core part of the construction of this estimator, (ii) we further derive (Section 4) the infinite sample limit of 1 up-Laplacian $\mathcal{L}_1^{\text{up}}$ and 1 down-Laplacian $\mathcal{L}_1^{\text{down}}$ under the assumption that the points are sampled from a constant density supported on \mathcal{M} , which proves the pointwise consistency and $a = \frac{1}{4}$ in $b = 1$ in the Helmholtzian. The spectral consistency of the corresponding $\mathcal{L}_1^{\text{down}}$ is also shown using the spectral dependency to the well-studied graph Laplacian. (iii) This work opens up avenues for the extensions of the well-studied node based Laplacian based algorithms to edge flow learning. This includes, but is not limited to, semi-supervised learning (SSL) [BNS06] on edge flows and smoothing/noise reduction for vector fields [SS18]. The classical Laplacian-type SSL and graph signal processing algorithms are thus applied to edge flow learning scenarios with the constructed weighted Helmholtzian \mathcal{L}_1^s . Furthermore, (iv) the effectiveness of the proposed weighted Helmholtzian are shown by comprehensive experiments on synthetic and real-world datasets. The proposed framework is a significant building block for new applications and algorithms in other domains of study, such as language datasets [Zhu13] with word2vec embedding [MSC⁺13], (multivariate) time series [GGB16], and 3D motion datasets [ABS07].

Acknowledgements

The authors acknowledge partial support from the U.S. Department of Energy’s Office of Energy Efficiency and Renewable Energy (EERE) under the Solar Energy Technologies Office Award Number DE-EE0008563 (M.M. and Y.C.), from the NSF DMS PD 08-1269 (M.M. and Y.C.), and an ARO MURI (I.G.K.). Part of this research was performed while the three authors were visiting the Institute for Pure and Applied Mathematics (IPAM), which is supported by the National Science

Foundation (Grant No. DMS-1925919). In addition, M.M. gratefully acknowledges an IPAM Simons Fellowship. This work was facilitated through the use of advanced computational, storage, and networking infrastructure provided by the Hyak supercomputer system and funded by the STF at the University of Washington. M.M. and Y.C. thank the Tkatchenko and Pfaendtner labs and in particular to Stefan Chmiela and Chris Fu for providing the molecular dynamics data and for many hours of brainstorming and advice, some of which took place at IPAM.

Disclaimer

The views expressed herein do not necessarily represent the views of the U.S. Department of Energy or the United States Government.

References

- [ABS07] Saad Ali, Arslan Basharat, and Mubarak Shah. Chaotic Invariants for Human Action Recognition. In *2007 IEEE 11th International Conference on Computer Vision*, pages 1–8, October 2007.
- [AFW10] Douglas Arnold, Richard Falk, and Ragnar Winther. Finite element exterior calculus: From Hodge theory to numerical stability. *Bulletin of the American Mathematical Society*, 47(2):281–354, 2010.
- [BG20] Tyrus Berry and Dimitrios Giannakis. Spectral exterior calculus. *Communications on Pure and Applied Mathematics*, 73(4):689–770, 2020.
- [BN07] Mikhail Belkin and Partha Niyogi. Convergence of laplacian eigenmaps. In B. Schölkopf, J. C. Platt, and T. Hoffman, editors, *Advances in Neural Information Processing Systems 19*, pages 129–136. MIT Press, 2007.
- [BNPB13] H. Bhatia, G. Norgard, V. Pascucci, and P. Bremer. The Helmholtz-Hodge Decomposition—A Survey. *IEEE Transactions on Visualization and Computer Graphics*, 19(8):1386–1404, August 2013.
- [BNS06] Mikhail Belkin, Partha Niyogi, and Vikas Sindhwani. Manifold regularization: A geometric framework for learning from labeled and unlabeled examples. *Journal of machine learning research*, 7(Nov):2399–2434, 2006.
- [BS19] Tyrus Berry and Timothy Sauer. Consistent manifold representation for topological data analysis. *Foundations of Data Science*, 1(1):1, 2019.
- [Chu96] Fan Chung. *Spectral Graph Theory*, volume 92 of *CBMS Regional Conference Series in Mathematics*. American Mathematical Society, December 1996.
- [CL06] Ronald R. Coifman and Stéphane Lafon. Diffusion maps. *Applied and Computational Harmonic Analysis*, 21(1):5–30, July 2006.
- [Cle17] Jeanne N. Clelland. *From Frenet to Cartan: The Method of Moving Frames*, volume 178. American Mathematical Soc., 2017.
- [CLM13] Guangliang Chen, Anna V. Little, and Mauro Maggioni. *Multi-Resolution Geometric Analysis for Data in High Dimensions*, pages 259–285. Birkhäuser Boston, Boston, 2013.
- [CM17] Frédéric Chazal and Bertrand Michel. An introduction to Topological Data Analysis: Fundamental and practical aspects for data scientists. *arXiv:1710.04019 [cs, math, stat]*, October 2017.
- [CMOP11] Ozan Candogan, Ishai Menache, Asuman Ozdaglar, and Pablo A. Parrilo. Flows and Decompositions of Games: Harmonic and Potential Games. *Mathematics of Operations Research*, 36(3):474–503, August 2011.
- [Col06] Bruno Colbois. Spectral Theory and Geometry. pp.34:cel-00392158, 2006.
- [CTS⁺17] Stefan Chmiela, Alexandre Tkatchenko, Huziel E Sauceda, Igor Poltavsky, Kristof T Schütt, and Klaus-Robert Müller. Machine learning of accurate energy-conserving molecular force fields. *Science advances*, 3(5):e1603015, 2017.

- [DFW13] Tamal K. Dey, Fengtao Fan, and Yusu Wang. Graph Induced Complex on Point Data. *arXiv:1304.0662 [cs, math]*, April 2013.
- [DKT08] Mathieu Desbrun, Eva Kanso, and Yiyang Tong. Discrete Differential Forms for Computational Modeling. In Alexander I. Bobenko, John M. Sullivan, Peter Schröder, and Günter M. Ziegler, editors, *Discrete Differential Geometry*, Oberwolfach Seminars, pages 287–324. Birkhäuser, Basel, 2008.
- [DM95] Józef Dodziuk and Jeffrey McGowan. The Spectrum of the Hodge Laplacian for a Degenerating Family of Hyperbolic Three Manifolds. *Transactions of the American Mathematical Society*, 347(6):1981–1995, 1995.
- [Dod76] Jozef Dodziuk. Finite-Difference Approach to the Hodge Theory of Harmonic Forms. *American Journal of Mathematics*, 98(1):79–104, 1976.
- [Eck44] Beno Eckmann. Harmonische Funktionen und Randwertaufgaben in einem Komplex. *Commentarii mathematici Helvetici*, 17:240–255, 1944.
- [FP15] Gary Froyland and Kathrin Padberg-Gehle. A rough-and-ready cluster-based approach for extracting finite-time coherent sets from sparse and incomplete trajectory data. *Chaos: An Interdisciplinary Journal of Nonlinear Science*, 25(8):087406, July 2015.
- [GGB16] Chad Giusti, Robert Ghrist, and Danielle S. Bassett. Two’s company, three (or more) is a simplex. *Journal of Computational Neuroscience*, 41(1):1–14, August 2016.
- [GP10] Leo J. Grady and Jonathan Polimeni. *Discrete Calculus: Applied Analysis on Graphs for Computational Science*. Springer-Verlag, London, 2010.
- [GR13] Chris Godsil and Gordon F. Royle. *Algebraic Graph Theory*. Springer Science & Business Media, December 2013.
- [HJ13] Danijela Horak and Jürgen Jost. Spectra of combinatorial Laplace operators on simplicial complexes. *Advances in Mathematics*, 244:303–336, September 2013.
- [JLYY11] Xiaoye Jiang, Lek-Heng Lim, Yuan Yao, and Yinyu Ye. Statistical ranking and combinatorial Hodge theory. *Mathematical Programming*, 127(1):203–244, March 2011.
- [JMM17] Dominique Joncas, Marina Meila, and James McQueen. Improved graph laplacian via geometric Self-Consistency. In I Guyon, U V Luxburg, S Bengio, H Wallach, R Fergus, S Vishwanathan, and R Garnett, editors, *Advances in Neural Information Processing Systems 30*, pages 4457–4466. Curran Associates, Inc., 2017.
- [JSSB19] Junteng Jia, Michael T. Schaub, Santiago Segarra, and Austin R. Benson. Graph-based Semi-Supervised & Active Learning for Edge Flows. In *KDD*, 2019.
- [KS13] Michael Kerber and R. Sharathkumar. Approximate Čech Complex in Low and High Dimensions. In Leizhen Cai, Siu-Wing Cheng, and Tak-Wah Lam, editors, *Algorithms and Computation*, Lecture Notes in Computer Science, pages 666–676, Berlin, Heidelberg, 2013. Springer.
- [Lee06] John M. Lee. *Riemannian Manifolds: An Introduction to Curvature*, volume 176. Springer Science & Business Media, 2006.
- [Lim20] Lek-Heng Lim. Hodge laplacians on graphs. *Siam Review*, 62(3):685–715, 2020.
- [LMSZ⁺18] Gioele La Manno, Ruslan Soldatov, Amit Zeisel, Emelie Braun, Hannah Hochgerner, Viktor Petukhov, Katja Lidschreiber, Maria E. Kastriiti, Peter Lönnerberg, and Alessandro Furlan. RNA velocity of single cells. *Nature*, 560(7719):494–498, 2018.
- [LPS15] Siu Kwan Lam, Antoine Pitrou, and Stanley Seibert. Numba: A LLVM-based Python JIT compiler. In *Proceedings of the Second Workshop on the LLVM Compiler Infrastructure in HPC, LLVM ’15*, pages 1–6, Austin, Texas, November 2015. Association for Computing Machinery.
- [LSW09] Chuanjiang Luo, Issam Safa, and Yusu Wang. Approximating gradients for meshes and point clouds via diffusion metric. In *Computer Graphics Forum*, volume 28, pages 1497–1508. Wiley Online Library, 2009.
- [MBGY14] Clément Maria, Jean-Daniel Boissonnat, Marc Glisse, and Mariette Yvinec. The gudhi library: Simplicial complexes and persistent homology. In *International Congress on Mathematical Software*, pages 167–174. Springer, 2014.

- [MS16] Sayan Mukherjee and John Steenbergen. Random walks on simplicial complexes and harmonics. *Random structures & algorithms*, 49(2):379–405, 2016.
- [MSC⁺13] Tomas Mikolov, Ilya Sutskever, Kai Chen, Greg S Corrado, and Jeff Dean. Distributed Representations of Words and Phrases and their Compositionality. In C. J. C. Burges, L. Bottou, M. Welling, Z. Ghahramani, and K. Q. Weinberger, editors, *Advances in Neural Information Processing Systems 26*, pages 3111–3119. Curran Associates, Inc., 2013.
- [MW06] Sayan Mukherjee and Qiang Wu. Estimation of gradients and coordinate covariation in classification. *Journal of Machine Learning Research*, 7(Nov):2481–2514, 2006.
- [NLCK06] Boaz Nadler, Stéphane Lafon, Ronald R. Coifman, and Ioannis G. Kevrekidis. Diffusion maps, spectral clustering and reaction coordinates of dynamical systems. *Applied and Computational Harmonic Analysis*, 21(1):113–127, 2006.
- [OFK⁺18] Antonio Ortega, Pascal Frossard, Jelena Kovačević, José M. F. Moura, and Pierre Vandergheynst. Graph Signal Processing: Overview, Challenges, and Applications. *Proceedings of the IEEE*, 106(5):808–828, May 2018.
- [OPT⁺17] Nina Otter, Mason A. Porter, Ulrike Tillmann, Peter Grindrod, and Heather A. Harrington. A roadmap for the computation of persistent homology. *EPJ Data Science*, 6(1):17, December 2017.
- [Pos09] Olaf Post. First Order Approach and Index Theorems for Discrete and Metric Graphs. *Annales Henri Poincaré*, 10(5):823–866, August 2009.
- [PR17] Ori Parzanchevski and Ron Rosenthal. Simplicial complexes: Spectrum, homology and random walks. *Random Structures & Algorithms*, 50(2):225–261, March 2017.
- [SBH⁺20] Michael T. Schaub, Austin R. Benson, Paul Horn, Gabor Lippner, and Ali Jadbabaie. Random walks on simplicial complexes and the normalized Hodge 1-Laplacian. *SIAM Review*, 62(2):353–391, 2020.
- [She13] Donald R. Sheehy. Linear-size approximations to the Vietoris–Rips filtration. *Discrete & Computational Geometry*, 49(4):778–796, 2013.
- [Sin06] A. Singer. From graph to manifold Laplacian: The convergence rate. *Applied and Computational Harmonic Analysis*, 21(1):128–134, July 2006.
- [SS18] M. T. Schaub and S. Segarra. Flow Smoothing And Denoising: Graph Signal Processing In The Edge-Space. In *2018 IEEE Global Conference on Signal and Information Processing (GlobalSIP)*, pages 735–739, November 2018.
- [SW11] Amit Singer and Hau-tieng Wu. Vector Diffusion Maps and the Connection Laplacian. *arXiv:1102.0075 [math, stat]*, January 2011.
- [THJ10] Daniel Ting, Ling Huang, and Michael Jordan. An Analysis of the Convergence of Graph Laplacians. In *Proceedings of the 27th International Conference on Machine Learning (ICML)*, 2010.
- [Was18] Larry Wasserman. Topological data analysis. *Annual Review of Statistics and Its Application*, 5:501–532, 2018.
- [Whi05] Hassler Whitney. *Geometric Integration Theory*. Dover Publications, Mineola, N.Y, December 2005.
- [ZG02] Xiaojin Zhu and Zoubin Ghahramani. Learning from labeled and unlabeled data with label propagation. 2002.
- [ZGL03] Xiaojin Zhu, Zoubin Ghahramani, and John Lafferty. Semi-supervised learning using Gaussian fields and harmonic functions. In *Proceedings of the Twentieth International Conference on International Conference on Machine Learning, ICML’03*, pages 912–919, Washington, DC, USA, August 2003. AAAI Press.
- [Zhu13] Xiaojin Zhu. Persistent Homology: An Introduction and a New Text Representation for Natural Language Processing. In *Twenty-Third International Joint Conference on Artificial Intelligence*, June 2013.

Supplementary Material of Helmholtzian Eigenmap: Topological feature discovery & edge flow learning from point cloud data

Table of Contents

A	Notational table	1
B	Pseudocodes	1
C	Rigorous definitions	2
D	Technical lemmas of exterior calculus	3
E	Proofs of the pointwise convergence of the <i>up</i> Helmholtzian	6
	E.1 Outline of the proof	6
	E.2 Proof of Lemma 1	6
	E.3 Proof of Proposition 2	7
	E.4 Proof of Theorem 3	16
F	Proofs of the pointwise convergence of the <i>down</i> Helmholtzian	17
	F.1 Proof of Proposition 4	17
	F.2 proof of theorem 5	19
G	Proofs of the spectral consistency of down Laplacian	20
	G.1 Outline of the proof	20
	G.2 Spectral dependency and related corollaries	20
	G.3 Proof of Proposition S17	21
H	Effects of the weights a, b between up/down Laplacians	23
I	Velocity field and cochain processing	24
	I.1 Obtaining a 1-cochain	24
	I.2 Smoother vector field from the 1-cochain by a damped least square	24
	I.3 Velocity field mapping between representations	27
J	Datasets	27
	J.1 Synthetic datasets	27
	J.2 Small molecule datasets	28
	J.3 Ocean drifter dataset	28
	J.4 Single cell RNA velocity data	30
K	SSL experiments on the divergence free flows	30

L Choice of regularization parameter λ for estimating point-wise velocity field from 1-cochain—vector field from all experiments **31**

A Notational table

Table S1: Notational table	
Matrix operation	
\mathbf{M}	Matrix
\mathbf{m}_i	Vector represents the i -th row of \mathbf{M}
$\mathbf{m}_{:,j}^T$	Vector represents the j -th column of \mathbf{M}
m_{ij}	Scalar represents ij -th element of \mathbf{M}
$[\mathbf{M}]_{ij}$	Scalar, alternative notation for m_{ij}
$\mathbf{M}[\alpha, \beta]$	Submatrix of \mathbf{M} of index sets α, β
\mathbf{v}	Column vecor
v_i	Scalar represents i -th element of vecor \mathbf{v}
$[\mathbf{v}]_i$	Scalar, alternative notation for v_i
Scalars	
n	Number of samples (nodes) ($= n_0$)
n_k	Dimension of k co-chain ($= \Sigma_k $)
d	Intrinsic dimension
δ	Bandwidth parameter for \mathbf{L}
ε	Bandwidth parameter for \mathbf{W}_2
Vectors & Matrices	
\mathbf{X}	Data matrix
\mathbf{x}_i	Point i in ambient space
\mathbf{B}_k	Boundary operator of k chain
\mathbf{L}	Graph Laplacian
\mathbf{L}_k	k unnormalized Hodge Laplacian
\mathbf{w}_k	$\in \mathbb{R}^{n_k}$, weights of k (co)chain
\mathbf{W}_k	$= \text{diag}(\mathbf{w}_k)$
\mathcal{L}_k	k random walk Hodge Laplacian
\mathcal{L}_k^s	k symmetrized Hodge Laplacian
\mathbf{I}_n	Identity matrix $\in \mathbb{R}^{n \times n}$
$\mathbf{1}_n$	All one vecor $\in \mathbb{R}^n$
$\mathbf{1}_S$	$[\mathbf{1}_S]_i = 1$ if $i \in S$ 0 otherwise
$\mathbf{0}_n$	All zero vecor $\in \mathbb{R}^n$
Miscellaneous	
Σ_k	Set of k -simplices
$V = \Sigma_0$	Set of nodes
$E = \Sigma_1$	Set of edges
$T = \Sigma_2$	Set of triangles
SC_ℓ	$= (\Sigma_k)_{k=0}^\ell = (\Sigma_0, \Sigma_1, \dots, \Sigma_\ell)$ simplicial complex up to dimension ℓ
$G(V, E)$	Graph with vertex set V and edge set E $= \text{SC}_1 = (\Sigma_0, \Sigma_1)$
\mathcal{M}	Data manifold
$[s]$	Set $\{1, \dots, s\}$
ϵ_π	Levi-Civita symbol for permutation π
d	Exterior derivative
δ	Co-differential operator

B Pseudocodes

Algorithm S1: BOUNDARYMAP

Input : Set of $k-1$ and k simplices Σ_{k-1}, Σ_k

- 1 $\mathbf{B}_k \leftarrow \mathbf{0}_{n_{k-1}} \mathbf{0}_{n_k}^\top \in \mathbb{R}^{n_{k-1} \times n_k}$
- 2 **for** every $\sigma_{k-1} \in \Sigma_{k-1}$ **do**
- 3 **for** every $\sigma_k \in \Sigma_k$ **do**
- 4 **if** σ_{k-1} is a face of σ_k **then**
- 5 $[\mathbf{B}_k]_{\sigma_{k-1}, \sigma_k} \leftarrow \epsilon_{i_j, i_0 \dots \hat{i}_j \dots i_k}$
 ▷ See (S3).
- 6 **else**
- 7 $[\mathbf{B}_k]_{\sigma_{k-1}, \sigma_k} \leftarrow 0$
- 8 **end**
- 9 **end**
- 10 **end**

Return : Boundary map for k -chain \mathbf{B}_k

Algorithm S2: VRCOMPLEX

Input : Data matrix $\mathbf{X} \in \mathbb{R}^{n \times D}$, radius $\text{max_dist } \delta$, $\text{max_dim } k$

- 1 Build graph $G(V, E)$ with $V = [n]$ and
 $E = \{(i, j) \in V^2 : \|\mathbf{x}_i - \mathbf{x}_j\| < \delta\}$
- 2 **for** $\ell = 2 \rightarrow k$ **do**
- 3 $\Sigma_\ell = \{(i_0, \dots, i_\ell) \in V^\ell : e \in E \forall e \in \binom{(i_0, \dots, i_\ell)}{2}\}$ ▷ Clique complex of G
- 4 **end**

Return : VR complex
 $\text{SC}_k = (V, E, \dots, \Sigma_k)$

Algorithm S3: BOOTSTRAPPD

Input : Data matrix $\mathbf{X} \in \mathbb{R}^{n \times D}$, $\text{max_dim } k$, $\text{num_bootstrap_samples } B$, significance level α

- 1 Compute persistent diagram $\mathcal{P} \leftarrow \text{PD}(\mathbf{X}, k)$
- 2 **for** $i = 1 \rightarrow B$ **do**
- 3 Sample $[\tilde{\mathbf{x}}_i]_{i=1}^n$ with replacement from \mathbf{X}
- 4 Bootstrapped PD $\tilde{\mathcal{P}}_i \leftarrow \text{PD}(\tilde{\mathbf{X}}, k)$
- 5 **for** $\ell = 0 \rightarrow k$ **do**
- 6 $\mathcal{D}_i^\ell \leftarrow \text{BOTTLENECKDIST}(\mathcal{P}, \tilde{\mathcal{P}}_i, \ell)$
- 7 **end**
- 8 **end**
- 9 **for** $\ell = 0 \rightarrow k$ **do**
- 10 $b_\alpha^\ell \leftarrow \text{PERCENTILE}(\mathcal{D}_i^\ell, 1 - \alpha)$
- 11 **end**

Return : Confidence band $\{b_\alpha^\ell\}_{\ell=0}^k$

C Rigorous definitions

First we define the Levi-Civita notation and permutation parity. This is useful for the definition of boundary operator \mathbf{B}_k .

Definition S1 (Permutation parity). Given a finite set $\{j_0, j_1, \dots, j_k\}$ with $k \geq 1$ and $j_\ell < j_m$ if $\ell < m$, the parity of a permutation $\varsigma(\{j_0, \dots, j_k\}) = \{i_0, i_1, \dots, i_k\}$ is defined to be

$$\epsilon_{i_0, \dots, i_k} = -1^{N(\varsigma)}. \quad (\text{S1})$$

Here $N(\varsigma)$ is the *inversion number* of ς . The inversion number is the cardinality of the inversion set, i.e., $N(\varsigma) = \#\{(\ell, m) : i_\ell > i_m \text{ if } \ell < m\}$. We say ς is an even permutation if $\epsilon_{i_0, \dots, i_k} = 1$ and an odd permutation otherwise.

Remark. When $k = 1$, the Levi-Civita symbol is

$$\epsilon_{ij} = \begin{cases} +1 & \text{if } (i, j) = (1, 2), \\ -1 & \text{if } (i, j) = (2, 1). \end{cases}$$

For $k = 2$, the Levi-Civita symbol is

$$\epsilon_{ijk} = \begin{cases} +1 & \text{if } (i, j, k) \in \{(1, 2, 3), (2, 3, 1), (3, 1, 2)\}, \\ -1 & \text{if } (i, j, k) \in \{(3, 2, 1), (1, 3, 2), (2, 1, 3)\}. \end{cases}$$

With this in hand, one can define the boundary map as follows.

Definition S2 (Boundary map & boundary matrix). Let $i_0 \cdots \hat{i}_j \cdots i_k := i_0, \dots, i_{j-1}, i_{j+1}, \dots, i_k$, and $i_0 \cdots \check{i}_j \cdots i_k$ denote i_j insert into i_0, \dots, i_k with proper order, we define a *boundary map (operator)* $\mathcal{B}_k : \mathcal{C}_k \rightarrow \mathcal{C}_{k-1}$, which maps a simplex to its face, by

$$\mathcal{B}_k([i_0, \dots, i_k]) = \sum_{j=0}^k (-1)^j [i_0 \cdots \hat{i}_j \cdots i_k] = \sum_{j=0}^k \epsilon_{i_j, i_0 \cdots \hat{i}_j \cdots i_k} [i_0 \cdots \check{i}_j \cdots i_k]. \quad (\text{S2})$$

Here $i_j, i_0 \cdots \hat{i}_j \cdots i_k := i_j, i_0, \dots, i_{j-1}, i_{j+1}, \dots, i_k$.

The corresponding *boundary matrix* $\mathbf{B}_k \in \{0, \pm 1\}^{n_{k-1} \times n_k}$ can be defined as follows.

$$(\mathbf{B}_k)_{\sigma_{k-1}, \sigma_k} \begin{cases} \epsilon_{i_j, i_0 \cdots \hat{i}_j \cdots i_k} & \text{if } \sigma_k = [i_0, \dots, i_k], \sigma_{k-1} = [i_0 \cdots \check{i}_j \cdots i_k], \\ 0 & \text{otherwise.} \end{cases} \quad (\text{S3})$$

$(\mathbf{B}_k)_{\sigma_{k-1}, \sigma_k}$ represents the orientation of σ_{k-1} as a face of σ_k , or equals 0 when the two are not adjacent.

Example. For the simplicial complex SC_2 in Figure S1, the corresponding \mathbf{B}_1 is in Table S3 while \mathbf{B}_2 is in Table S2.

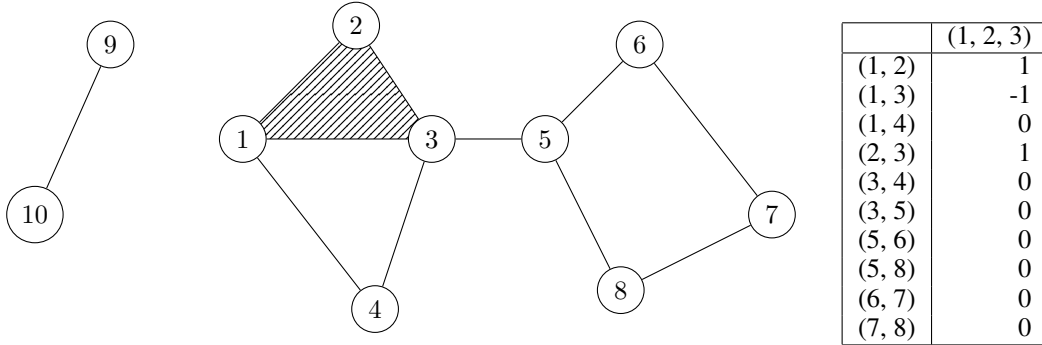


Figure S1: Illustration of a $\text{SC}_2 = (\Sigma_0, \Sigma_1, \Sigma_2)$, shaded region denotes that the triangle $t \in \Sigma_2$.

Table S2: \mathbf{B}_2 of SC_2

In this example, triangle is not always filled, e.g., $[1, 3, 4] \notin \Sigma_2$. However, for the construction of VR complex described in Algorithm 1, every triangle in SC_2 is filled.

	(1, 2)	(1, 3)	(1, 4)	(2, 3)	(3, 4)	(3, 5)	(5, 6)	(5, 8)	(6, 7)	(7, 8)	(9, 10)
1	1	1	1	0	0	0	0	0	0	0	0
2	-1	0	0	1	0	0	0	0	0	0	0
3	0	-1	0	-1	1	1	0	0	0	0	0
4	0	0	-1	0	-1	0	0	0	0	0	0
5	0	0	0	0	0	-1	1	1	0	0	0
6	0	0	0	0	0	0	-1	0	1	0	0
7	0	0	0	0	0	0	0	0	-1	1	0
8	0	0	0	0	0	0	0	-1	0	-1	0
9	0	0	0	0	0	0	0	0	0	0	1
10	0	0	0	0	0	0	0	0	0	0	-1

Table S3: Boundary matrix \mathbf{B}_1 (incident matrix) of SC_2 in Figure S1.

Below we provide the definition of the Hodge star operator and d , δ .

Definition S3 (Hodge star). Hodge star on 1 form (dual of basis function) is defined as follow,

$$\star(ds_{i_1} \wedge \cdots \wedge ds_{i_k}) = \epsilon_{IJ} ds_{j_1} \wedge \cdots \wedge ds_{j_{d-k}} \quad (\text{S4})$$

Here $J = \{j_1 \cdots, j_{d-k}\}$ is the (ordered) complement of $I = \{i_1, \cdots, i_k\}$. E.g., if $I = \{1, 5\}$ in $d = 7$ dimensional space, we have $J = \{2, 3, 4, 6, 7\}$. ϵ_{IJ} is the Levi-Civita symbol of the permutation $IJ = \{i_1 \cdots i_k, j_1 \cdots, j_{n-k}\}$.

Definition S4 (Differential & Co-differential). The differential of k form ζ_k with $\zeta_k = f ds_{i_1} \wedge \cdots \wedge ds_{i_k}$ is

$$d\zeta = \sum_{j=1}^d \frac{\partial f}{\partial s_j} ds_j \wedge (ds_{i_1} \wedge \cdots \wedge ds_{i_k}). \quad (\text{S5})$$

The co-differential δ on a k form is defined as

$$\delta = (-1)^{d(k-1)+1} \star d \star. \quad (\text{S6})$$

D Technical lemmas of exterior calculus

In this section, we derive the closed form of 1-Laplacian $\Delta_1 = d\delta + \delta d$ on local coordinate system (tangent plane) when metric tensor at each point is identity. Note that the assumption is sufficient for current work since the Simplicial complex SC_2 is built in the *ambient space*. We start with some useful identities list as follows.

Lemma S5 (Identities of permutation parity). *Given the Levi-Civita symbol ϵ , one has the following two identities.*

$$\epsilon_{\{i\}\{-i, -j\}} = \epsilon_{ij} \epsilon_{i, -i}. \quad (\text{S7})$$

Proof. Consider the case when $j > i$, i.e., $\epsilon_{ij} = 1$. We have $\epsilon_{\{i\}\{-i, -j\}} = \epsilon_{i, -i}$, for the inversion number of $\{i\}\{-i, -j\}$ is $i - 1$, which is identical to the inversion number of permutation $i, -i$. This implies the parity of the permutation is $\epsilon_{i, -i}$. Consider the case $i > j$, i.e., $\epsilon_{ij} = -1$, the inversion number of the permutation $\{i\}\{-i, -j\}$ is $i - 2$ since there is $i - 2$ elements (excluding j) that is smaller than i in $\{-i, -j\}$. This implies that the parity of $\{i\}\{-i, -j\}$ is $-1 \cdot \epsilon_{i, -i}$. This completes the proof. ■

Let $i' < j'$, the second identity states that,

$$\epsilon_{\{i', j'\}\{-i', -j'\}} = -\epsilon_{i', -i'} \epsilon_{j', -j'}. \quad (\text{S8})$$

Proof. The inversion number of the permutation $\{i', j'\}\{-i', -j'\}$ is $(j' - 2) + (i' - 1) = i' + j' - 3$; the inversion numbers of the permutations $\{j'\}\{-i', -j'\}$ and $i', -i'$ are $j' - 2$ and $i' - 1$, respectively. One can show that $\epsilon_{\{i', j'\}\{-i', -j'\}} = \epsilon_{\{j'\}\{-i', -j'\}} \cdot \epsilon_{i', -i'}$. From (S7), we have $\epsilon_{\{j'\}\{-i', -j'\}} = \epsilon_{j' i'} \epsilon_{j', -j'} = -\epsilon_{j', -j'}$. This completes the proof. ■

The following lemma presents the codifferential of a 2-form.

Lemma S6 (Codifferential of a 2-form). *Let $\zeta_2 = \sum_i \sum_{j \neq i} A_{ij} ds_j \wedge ds_i$ be a 2-form. The codifferential operator δ acting on ζ_2 is*

$$\delta \zeta_2 = \sum_i \sum_{j \neq i} \left(\frac{\partial A_{ji}}{\partial s_j} - \frac{\partial A_{ij}}{\partial s_j} \right) ds_i. \quad (\text{S9})$$

Proof.

$$\star d \star \zeta_2 = \sum_i \sum_{j \neq i} \star d A_{ij} \star (ds_j \wedge ds_i) = \sum_i \sum_{j \neq i} \sum_{k \in \{i, j\}} \frac{\partial A_{ij}}{\partial s_k} \star (ds_k \wedge \star (ds_j \wedge ds_i)).$$

The last summation is over $k \in \{i, j\}$ otherwise it will produce zero. Next step is to derive the exact form of $\star (ds_k \wedge \star (ds_j \wedge ds_i))$. Consider the case when $k = i$, we have

$$\begin{aligned} \star (ds_i \wedge \star (ds_j \wedge ds_i)) &= \epsilon_{ji} \cdot \star (ds_i \wedge \star (ds_{i'} \wedge ds_{j'})) \\ &= \epsilon_{ji} \epsilon_{\{i', j'\} \{-i', -j'\}} \star \left(ds_i \wedge \bigwedge_{\ell \in \{-i', -j'\}} ds_\ell \right) \\ &= \epsilon_{ji} \epsilon_{\{i', j'\} \{-i', -j'\}} \epsilon_{\{i\} \{-i, -j\}} \epsilon_{-j, j} ds_j = \underbrace{\epsilon_{j, -j} \epsilon_{-j, j}}_{=(-1)^{d+1}} ds_j. \end{aligned}$$

Last equality holds from Lemma S5 and $\epsilon_{j, -j} \epsilon_{-j, j} = (-1)^{d+1}$. Consider the case when $k = j$,

$$\begin{aligned} \star (ds_j \wedge \star (ds_j \wedge ds_i)) &= \epsilon_{ji} \cdot \star (ds_j \wedge \star (ds_{i'} \wedge ds_{j'})) \\ &= \epsilon_{ji} \epsilon_{(\{i', j'\} \{-i', -j'\})} \star \left(ds_j \wedge \bigwedge_{\ell \in \{-i', -j'\}} ds_\ell \right) \\ &= \epsilon_{ji} \underbrace{\epsilon_{\{i', j'\} \{-i', -j'\}}}_{=-\epsilon_{i, -i} \epsilon_{j, -j}} \underbrace{\epsilon_{\{j\} \{-i, -j\}}}_{=\epsilon_{ji} \epsilon_{j, -j}} \epsilon_{-i, i} ds_i = (-1)^{d+1} \cdot (-ds_i). \end{aligned}$$

Putting things together, we have

$$\begin{aligned} \delta \zeta_2 &= (-1)^{d+1} \star d \star \zeta_2 = \sum_i \sum_{j \neq i} \frac{\partial A_{ij}}{\partial s_i} ds_j - \frac{\partial A_{ij}}{\partial s_j} ds_i \\ &= \sum_i \sum_{j \neq i} \left(\frac{\partial A_{ji}}{\partial s_j} - \frac{\partial A_{ij}}{\partial s_j} \right) ds_i. \end{aligned}$$

Last equality holds by changing the index of summing. ■

With Lemma S6 in hand, we can start deriving the closed for of Δ_1 in the local coordinate system.

Proposition S7 (1-Laplacian in local coordinate system). *Let $\zeta_1 = \sum_{i=1}^d f_i ds_i$ be a 1-form. The up-Laplacian $\Delta_1^{\text{down}} = \delta d$ operates on ζ_1 (in local coordinate system) is*

$$\delta d \zeta_1 = \sum_i \sum_{j \neq i} \left(\frac{\partial^2 f_j}{\partial s_j \partial s_i} - \frac{\partial^2 f_i}{\partial s_j^2} \right) ds_i. \quad (\text{S10})$$

The down-Laplacian $\Delta_1^{\text{down}} = d \delta$ operates on ζ_1 (in local coordinate system) is

$$d \delta \zeta_1 = - \sum_i \sum_j \frac{\partial^2 f_j}{\partial s_i \partial s_j} ds_i. \quad (\text{S11})$$

Proof. We first consider the up-Laplacian $\delta d\zeta_1 = \delta\zeta_2$ on 1 form ζ_1 with

$$\zeta_2 = d\zeta_1 = d\left(\sum_{i=1}^d f_i ds_i\right) = \sum_i \sum_{j \neq i} \frac{\partial f_i}{\partial s_j} ds_j \wedge ds_i.$$

From Lemma S6 and let $A_{ij} = \frac{\partial f_i}{\partial s_j}$, we have

$$\delta d\zeta_1 = \sum_i \sum_{j \neq i} \left(\frac{\partial^2 f_j}{\partial s_j \partial s_i} - \frac{\partial^2 f_i}{\partial s_j^2} \right) ds_i.$$

Consider the case of the down-Laplacian and note that $\delta = -\star d\star$. Since the co-differential is now act on 1 form rather than $k = 2$, we have

$$\begin{aligned} d\delta\zeta_1 &= -d\star d\star\zeta_1 = -\sum_i d\star d(f_i \star ds_i) = -\sum_i d\star \sum_j \frac{\partial f_i}{\partial s_j} ds_j \wedge \star ds_i \\ &\stackrel{(i)}{=} -\sum_i d\star \frac{\partial f_i}{\partial s_i} \bigwedge_{\ell=1}^d ds_\ell \stackrel{(ii)}{=} -\sum_i \sum_j \frac{\partial^2 f_i}{\partial s_i \partial s_j} ds_j. \end{aligned}$$

Equality (i) holds since $ds_j \wedge \star ds_i = 1$ if $i = j$ and 0 otherwise. Equality (ii) holds for $\star \bigwedge_{\ell=1}^d ds_\ell = 1$ (a 0-form). \blacksquare

Remark (Sanity check on 3D). Note that in 3D, $\text{curl} = \star d$, therefore $\delta d = \star d \star d = \text{curl curl}$. For a vector field (1-form) $\zeta_1 = f_1 ds_1 + f_2 ds_2 + f_3 ds_3$, one has

$$\begin{aligned} \nabla \times \zeta_1 &= \left(\frac{\partial f_3}{\partial s_2} - \frac{\partial f_2}{\partial s_3} \right) ds_1 + \left(\frac{\partial f_1}{\partial s_3} - \frac{\partial f_3}{\partial s_1} \right) ds_2 + \left(\frac{\partial f_2}{\partial s_1} - \frac{\partial f_1}{\partial s_2} \right) ds_3. \\ \nabla \times (\nabla \times \zeta_1) &= \left(\frac{\partial^2 f_2}{\partial s_1 \partial s_2} - \frac{\partial^2 f_1}{\partial s_2^2} - \frac{\partial^2 f_1}{\partial s_3^2} + \frac{\partial^2 f_3}{\partial s_1 \partial s_3} \right) ds_1 \\ &= \left(\frac{\partial^2 f_3}{\partial s_2 \partial s_3} - \frac{\partial^2 f_2}{\partial s_3^2} - \frac{\partial^2 f_2}{\partial s_1^2} + \frac{\partial^2 f_1}{\partial s_1 \partial s_2} \right) ds_2 \\ &= \left(\frac{\partial^2 f_1}{\partial s_1 \partial s_3} - \frac{\partial^2 f_3}{\partial s_1^2} - \frac{\partial^2 f_3}{\partial s_2^2} + \frac{\partial^2 f_2}{\partial s_2 \partial s_3} \right) ds_3 \\ &= \sum_i \sum_{j \neq i} \left(\frac{\partial^2 f_j}{\partial s_j \partial s_i} - \frac{\partial^2 f_i}{\partial s_j^2} \right) ds_i. \end{aligned}$$

Corollary S8 (Relation to Laplace-Beltrami). *We have the following,*

$$\Delta_1 f = (\delta d + d\delta)\zeta_1 = -\sum_i \sum_j \frac{\partial^2 f_i}{\partial s_j^2} ds_i = -\sum_i \Delta_0 f_i ds_i. \quad (\text{S12})$$

Here $\Delta_0 f_i = \sum_j \frac{\partial^2 f_i}{\partial s_j^2}$ is the Laplacian on 0-form.

Proof. Can be obtained by applying the result from Proposition S7. \blacksquare

Remark (Vector Laplacian in 3D). Note that in 3D case, $\Delta_1 \zeta_1 = -\sum_i \Delta_0 f_i ds_i = -\nabla^2 f$. Here ∇^2 is vector Laplacian. This implies that vector Laplacian in 3D is essentially 1-Laplacian up to a sign change.

Corollary S9 (1-Laplacian on pure curl & gradient vector fields). *If the vector field ζ_1 is a pure curl or gradient vector field, then*

$$\Delta_1 \zeta_1 = (\delta d + d\delta)f = -\sum_i \sum_j \frac{\partial^2 f_i}{\partial s_j^2} ds_i = -\sum_i \Delta_0 f_i ds_i. \quad (\text{S13})$$

Proof. Consider the case when ζ_1 is curl flow ($d\delta\zeta_1 = 0$). This implies

$$\sum_j \frac{\partial^2 f_j}{\partial s_i \partial s_j} = 0 \forall i \in [d].$$

Hence we have $\sum_{j \neq i} \frac{\partial^2 f_j}{\partial s_i \partial s_j} = -\frac{\partial^2 f_i}{\partial s_i^2}$. Plugging into (S10), we have

$$\Delta_1 \zeta_1 = \delta d \zeta_1 = -\sum_i \sum_j \frac{\partial^2 f_i}{\partial s_j^2} ds_i = -\sum_i \Delta_0 f_i ds_i.$$

Consider the case when ζ_1 is gradient flow, which implies $\delta d f = 0$, or

$$\sum_{j \neq i} \left(\frac{\partial^2 f_j}{\partial s_j \partial s_i} - \frac{\partial^2 f_i}{\partial s_j^2} \right) = 0 \forall i \in [d].$$

Therefore the identity $\sum_{j \neq i} \frac{\partial^2 f_j}{\partial s_j \partial s_i} = \sum_{j \neq i} \frac{\partial^2 f_i}{\partial s_j^2}$ holds. Plugging into (S11), one has

$$\Delta_1 \zeta_1 = d\delta \zeta_1 = -\sum_i \left(\left(\sum_{j \neq i} \frac{\partial^2 f_i}{\partial s_j^2} \right) + \frac{\partial^2 f_i}{\partial s_i^2} \right) ds_i = -\sum_i \Delta_0 f_i ds_i.$$

This completes the proof. ■

E Proofs of the pointwise convergence of the *up* Helmholtzian

E.1 Outline of the proof

This section investigates the continuous limit of the discrete operator $\mathcal{L}_1^{\text{up}} = \mathbf{B}_T \mathbf{W}_T \mathbf{B}_T^\top \mathbf{W}_E^{-1}$.

E.2 Proof of Lemma 1

Proof. First, note that

$$[\mathbf{B}_T \mathbf{W}_T \mathbf{B}_T^\top \omega]_{[x,y]} = w_E(\mathbf{x}, \mathbf{y}) \omega_{[x,y]} + (\dots),$$

where $w_E(\mathbf{x}, \mathbf{y}) = [\mathbf{W}_E]_{xy,xy}$. There are six different cases to consider in the (\dots) part above. Assume $[x', y', z']$ is the canonical permutation/ordering of x, y, z , i.e., $x' < y' < z'$. Note that by the definition of $w_T(\mathbf{x}, \mathbf{y}, \mathbf{z})$, one has $w_T(\mathbf{x}', \mathbf{y}', \mathbf{z}') = w_T(\mathbf{x}, \mathbf{y}, \mathbf{z})$. Therefore, each part of the (\dots) term is

1. $[x', y'] \times [x', z'] \rightarrow w_T(\mathbf{x}, \mathbf{y}, \mathbf{z}) \cdot -1 \cdot \omega_{[x', z']}$
2. $[x', y'] \times [y', z'] \rightarrow w_T(\mathbf{x}, \mathbf{y}, \mathbf{z}) \cdot 1 \cdot \omega_{[y', z']}$
3. $[x', z'] \times [x', y'] \rightarrow w_T(\mathbf{x}, \mathbf{y}, \mathbf{z}) \cdot -1 \cdot \omega_{[x', y']}$
4. $[x', z'] \times [y', z'] \rightarrow w_T(\mathbf{x}, \mathbf{y}, \mathbf{z}) \cdot -1 \cdot \omega_{[y', z']}$
5. $[y', z'] \times [x', y'] \rightarrow w_T(\mathbf{x}, \mathbf{y}, \mathbf{z}) \cdot 1 \cdot \omega_{[x', y']}$
6. $[y', z'] \times [x', z'] \rightarrow w_T(\mathbf{x}, \mathbf{y}, \mathbf{z}) \cdot -1 \cdot \omega_{[x', z']}$

Grouping 1 and 2 together, one obtains

$$w_T(\mathbf{x}, \mathbf{y}, \mathbf{z})(\omega_{[y', z']} - \omega_{[x', z']}) = w_T(\mathbf{x}, \mathbf{y}, \mathbf{z})(f_{x'y'z'} - \omega_{[x', y]}).$$

Similarly, for 3 and 4 as well as 5 and 6, we have

$$\begin{aligned} w_T(\mathbf{x}, \mathbf{y}, \mathbf{z})(-\omega_{[x', y']} - \omega_{[y', z']}) &= w_T(\mathbf{x}, \mathbf{y}, \mathbf{z})(-f_{x'y'z'} - \omega_{[x', z]}); \\ w_T(\mathbf{x}, \mathbf{y}, \mathbf{z})(\omega_{[x', y']} - \omega_{[x', z']}) &= w_T(\mathbf{x}, \mathbf{y}, \mathbf{z})(f_{x'y'z'} - \omega_{[y', z]}). \end{aligned}$$

Here, $f_{x'y'z'} = \omega_{[x',y']} + \omega_{[y',z']} - \omega_{[x',z']}$. To sum up, the (\dots) part becomes

$$w_T(x, y, z)(\sigma_{xy,xyz} f_{x'y'z'} - f_{[x,y]}).$$

Note that $\sigma_{xy,xyz} f_{x'y'z'} = \omega_{xy} + \omega_{yz} + \omega_{zx} = f_{xyz}$, therefore,

$$\begin{aligned} [\mathbf{B}_T \mathbf{W}_T \mathbf{B}_T^\top \omega]_{[x,y]} &= w_E(\mathbf{x}, \mathbf{y}) \omega_{[x,y]} + \sum_{z \notin \{x,y\}} w_T(\mathbf{x}, \mathbf{y}, \mathbf{z})(\sigma_{xy,xyz} f_{x'y'z'} - \omega_{[x,y]}) \\ &= \cancel{w_E(\mathbf{x}, \mathbf{y}) \omega_{[x,y]}} - \sum_{z \notin \{x,y\}} \cancel{w_T(\mathbf{x}, \mathbf{y}, \mathbf{z}) \omega_{[x,y]}} + \dots \\ &= \sum_{z \notin \{x,y\}} w_T(\mathbf{x}, \mathbf{y}, \mathbf{z}) f_{xyz}. \end{aligned}$$

In the above, we use the fact that $\mathbf{W}_E = \text{diag}(|\mathbf{B}_T| \mathbf{W}_T \mathbf{1}_{n_T})$. This completes the proof. \blacksquare

E.3 Proof of Proposition 2

We are interested in the asymptotic expansion of $\int_{\mathcal{M}} w_T(\mathbf{x}, \mathbf{y}, \mathbf{z}) f_{xyz} d\mu(\mathbf{z})$. Specifically, our goal is to show the following expansion given some constant $c = c(\mathbf{x}, \mathbf{y})$.

$$\int_{\mathcal{M}} w_T(\mathbf{x}, \mathbf{y}, \mathbf{z}) f_{xyz} d\mu(\mathbf{z}) = c \int_{x \rightarrow y} (\Delta_1 f(\gamma(t))) \gamma'(t) dt + \mathcal{O}(\varepsilon^4). \quad (\text{S14})$$

Here, $\gamma(t)$ is the parameterization of the geodesic curve connecting \mathbf{x} and \mathbf{y} on the manifold \mathcal{M} . From Corollary S9 in D, one has $\Delta_1 v = \sum_i \sum_j \frac{\partial^2 f_i}{\partial s_j^2} ds_i = \sum_i \Delta_0 f_i ds_i$ in local coordinate (s_1, \dots, s_d) with $v = \sum_i f_i ds_i$. Therefore, it is sufficient to show that the LHS of (S14) can be expanded to terms consisting of only the coordinate-wise Δ_0 .

First, we show the upper bound for the error by integrating the integral operator around ε^γ balls around x and y . This lemma is the modification of a similar technique that appeared in Lemma 8 of [CL06].

Lemma S10 (Error bound for the localization of an exponential decay kernel). *Let $0 < \gamma < 1$ and g be a bounded function, the integration of the integral operator $\int_{\mathcal{M}} \kappa_\varepsilon(\mathbf{x}, \mathbf{z}) \kappa_\varepsilon(\mathbf{y}, \mathbf{z}) g(\mathbf{z}) d\mathbf{z}$ over \mathbf{z} that is ε^γ far away from points $x, y \in \mathcal{M}$ can be bounded above by $\mathcal{O}(\varepsilon^{4+d})$.*

Proof. First, we focus on the domain of the integral. Points $\mathbf{z} \in \mathcal{M}$ that are ε^γ far away from both \mathbf{x} and \mathbf{y} form a set $\{\mathbf{z} \in \mathcal{M} : \min(\|\mathbf{z} - \mathbf{x}\|, \|\mathbf{z} - \mathbf{y}\|) > \varepsilon^\gamma\}$. Because the kernel has exponential decay, one can follow the same technique of Lemma 8 in [CL06] to bound the integration by

$$\begin{aligned} & \left| \frac{1}{\varepsilon^d} \int_{\substack{\mathbf{z} \in \mathcal{M} \\ \min(\|\mathbf{z} - \mathbf{x}\|, \|\mathbf{z} - \mathbf{y}\|) > \varepsilon^\gamma}} \kappa\left(\frac{\|\mathbf{z} - \mathbf{x}\|^2}{\varepsilon^2}\right) \kappa\left(\frac{\|\mathbf{z} - \mathbf{y}\|^2}{\varepsilon^2}\right) g(\mathbf{z}) d\mathbf{z} \right| \\ & \leq \frac{\|g\|_\infty}{\varepsilon^d} \int_{\substack{\mathbf{z} \in \mathcal{M} \\ \min(\|\mathbf{z} - \mathbf{x}\|, \|\mathbf{z} - \mathbf{y}\|) > \varepsilon^\gamma}} \left| \kappa\left(\frac{\|\mathbf{z} - \mathbf{x}\|^2}{\varepsilon^2}\right) \right| \left| \kappa\left(\frac{\|\mathbf{z} - \mathbf{y}\|^2}{\varepsilon^2}\right) \right| d\mathbf{z} \\ & \leq \frac{\|g\|_\infty \|\kappa\|_\infty}{\varepsilon^d} \int_{\substack{\mathbf{z} \in \mathcal{M} \\ \|\mathbf{z} - \mathbf{x}\| > \varepsilon^\gamma}} \left| \kappa\left(\frac{\|\mathbf{z} - \mathbf{x}\|^2}{\varepsilon^2}\right) \right| d\mathbf{z} \\ & \leq \|g\|_\infty \|\kappa\|_\infty \int_{\substack{\mathbf{z} \in \mathcal{M} \\ \|\mathbf{z}\| > \varepsilon^{\gamma-1}}} |\kappa_\varepsilon(\|\mathbf{z}\|^2)| d\mathbf{z} \leq C \|g\|_\infty Q(\varepsilon^{1-\gamma}) \exp(-\varepsilon^{\gamma-1}). \end{aligned}$$

The last inequality holds by using the exponential decay of the kernel. Here, Q is some polynomial. Since $0 < \gamma < 1$, the term is exponentially small and is bounded by $\mathcal{O}(\varepsilon^{4+d})$. \blacksquare

Therefore, the original integral operator (LHS of (S14)) becomes

$$\varepsilon^{-d} \mathcal{L}_1^{\text{up}} f_{xy} = \varepsilon^{-d} \int_{\substack{\mathbf{z} \in \mathcal{M} \\ \max(\|\mathbf{z}-\mathbf{y}\|, \|\mathbf{z}-\mathbf{x}\|) \leq \varepsilon^\gamma}} \left(\kappa \left(\frac{\|\mathbf{z}-\mathbf{x}\|^2}{\varepsilon^2} \right) \kappa \left(\frac{\|\mathbf{z}-\mathbf{y}\|^2}{\varepsilon^2} \right) \oint_{\Gamma(x,y,z)} v \right) d\mathbf{z} + \mathcal{O}(\varepsilon^4).$$

We introduce the last lemma that is useful in removing the bias term in the line integral before proving Proposition 2.

Lemma S11 (Line integral approximation). *Assume $f \in \mathcal{C}^2$ and let $\mathbf{u}(t) = \mathbf{x} + (\mathbf{y} - \mathbf{x})t$ be a parameterization of the straight line connecting nodes x and y . We have the following error bound*

$$f(\mathbf{u}(t)) = f(\mathbf{x}) + ((f(\mathbf{y}) - f(\mathbf{x}))t + \mathcal{O}(\|\mathbf{y} - \mathbf{x}\|^2)). \quad (\text{S15})$$

Proof. Note that $\mathbf{u}(t) = \mathbf{x} + (\mathbf{y} - \mathbf{x})t$. By Taylor expansion on f , one has

$$f(\mathbf{x} + (\mathbf{y} - \mathbf{x})t) = f(\mathbf{x}) + (\mathbf{y} - \mathbf{x})^\top \nabla f(\mathbf{x}) \cdot t + \mathcal{O}(\|\mathbf{y} - \mathbf{x}\|^2).$$

Additionally, $(\mathbf{y} - \mathbf{x})^\top \nabla f(\mathbf{x})$ is the directional derivative, which can be approximate by $f(\mathbf{y}) - f(\mathbf{x}) + \mathcal{O}(\|\mathbf{y} - \mathbf{x}\|^2)$ by Taylor expansion. Therefore

$$f(\mathbf{u}(t)) = f(\mathbf{x} + (\mathbf{y} - \mathbf{x})t) = f(\mathbf{x}) + (f(\mathbf{y}) - f(\mathbf{x}))t + \mathcal{O}(\|\mathbf{y} - \mathbf{x}\|^2).$$

This completes the proof. ■

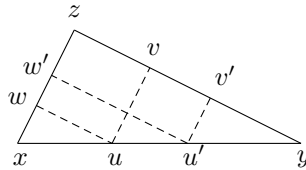
The outline of the proof is as follows. We first prove the asymptotic expansion of the integral operator $\int w_T(\mathbf{x}, \mathbf{y}, \mathbf{z}) f_{xyz} d\mu(\mathbf{z})$. Later on, we bound the error of approximating the manifold by tangent bundles. Lastly, the asymptotic expansion of the integral operator is obtained by incorporating the error terms of tangent plane approximation and the expansion in \mathbb{R}^d . The following lemma is the first step, i.e., the asymptotic expansion in \mathbb{R}^d .

Lemma S12 (Asymptotic expansion of $\mathcal{L}_1^{\text{up}}$ in \mathbb{R}^d). *Under Assumption 1–2, and further assume With the choice of exponential kernel $\kappa_\varepsilon(u) = \exp(-u)$ and $v = (f_1, \dots, f_d) \in \mathcal{C}^4(\mathcal{M})$. Let $\mathbf{u}(t) = \mathbf{x} + (\mathbf{y} - \mathbf{x})t$ for t in $[0, 1]$ be a parameterization of the straight line between nodes x, y and $\mathbf{u}'(t) = d\mathbf{u}(t)/dt$. With the choice of exponential kernel $\kappa(u) = \exp(-u)$, one has the following asymptotic expansion*

$$\begin{aligned} & \int_{\mathbf{z} \in \mathbb{R}^d} w_T(\mathbf{x}, \mathbf{y}, \mathbf{z}) f_{xyz} d\mu(\mathbf{z}) \\ &= \frac{2}{3} \varepsilon^{2+d} C_2 \int_0^1 \sum_i \sum_j \left(\frac{\partial^2 f_j(\mathbf{u}(t))}{\partial S_i \partial S_j} - \frac{\partial^2 f_i(\mathbf{u}(t))}{\partial S_j^2} \right) (\mathbf{y} - \mathbf{x})_i dt + \mathcal{O}(\varepsilon^d \delta^3) + \mathcal{O}(\varepsilon^{4+d}) + \mathcal{O}(\varepsilon^{2+d} \delta^2) \\ &= \frac{2}{3} \varepsilon^{2+d} C_2 \int_0^1 [(\delta d v(\mathbf{u}(t)))]^\top \mathbf{u}'(t) dt + \mathcal{O}(\varepsilon^d \delta^3) + \mathcal{O}(\varepsilon^{4+d}) + \mathcal{O}(\varepsilon^{2+d} \delta^2). \end{aligned} \quad (\text{S16})$$

Here, $C_2 = \varepsilon^{-(4+d)} \int_{\mathbf{z} \in \mathbb{R}^d} \kappa^2 \left(\frac{\|\mathbf{z}\|^2}{\varepsilon^2} \right) \mathbf{z}_1^2 \mathbf{z}_2^2 d\mathbf{z}$ and z_i is the i -th coordinate of \mathbf{z} .

Proof. First, we define $\mathbf{u}(t), \mathbf{v}(t), \mathbf{w}(t)$ as in the diagram below with $\mathbf{u}(0) = \mathbf{x}, \mathbf{u}(1) = \mathbf{y}, \mathbf{v}(0) = \mathbf{y}, \mathbf{v}(1) = \mathbf{z}$, and $\mathbf{w}(0) = \mathbf{z}, \mathbf{w}(1) = \mathbf{x}$.



For notational simplicity, we do not use the conventional (*unit speed*) parametrization of a curve in our analysis. One can always use the convention without changing any conclusions. Further

define $\Gamma(x, y, z)$ be the loop connecting nodes x, y, z , i.e., $\Gamma(x, y, z) = \{\mathbf{u}(t), \mathbf{v}(t), \mathbf{w}(t)\}$. The loop integral f_{xyz} becomes

$$\oint_{\Gamma(x,y,z)} v = \int_0^1 \mathbf{f}(\mathbf{u}(t))^\top (\mathbf{y} - \mathbf{x}) dt + \int_0^1 \mathbf{f}(\mathbf{v}(t))^\top (\mathbf{z} - \mathbf{y}) dt + \int_0^1 \mathbf{f}(\mathbf{w}(t))^\top (\mathbf{x} - \mathbf{z}) dt.$$

One can do the following coordinate-wise expansion up to second-order terms. With slight abuse of notation, let $\mathbf{v} = \mathbf{v}(t)$, $\mathbf{u} = \mathbf{u}(1-t)$, and s_1, \dots, s_d represent the coordinate system. Expanding $f_i(\mathbf{v})$ and $f_i(\mathbf{w})$ from $f_i(\mathbf{u})$ results in

$$\begin{aligned} f_i(\mathbf{v}(t)) &= f_i(\mathbf{u}(1-t)) + \sum_j \frac{\partial f_i(\mathbf{u})}{\partial s_j} (\mathbf{v} - \mathbf{u})_j + \sum_j \sum_k \frac{\partial^2 f_i(\mathbf{u})}{\partial s_j \partial s_k} (\mathbf{v} - \mathbf{u})_j (\mathbf{v} - \mathbf{u})_k + \mathcal{O}(\|\mathbf{z} - \mathbf{y}\|^3); \\ f_i(\mathbf{w}(t)) &= f_i(\mathbf{u}(1-t)) + \sum_j \frac{\partial f_i(\mathbf{u})}{\partial s_j} (\mathbf{w} - \mathbf{u})_j + \sum_j \sum_k \frac{\partial^2 f_i(\mathbf{u})}{\partial s_j \partial s_k} (\mathbf{w} - \mathbf{u})_j (\mathbf{w} - \mathbf{u})_k + \mathcal{O}(\|\mathbf{z} - \mathbf{x}\|^3). \end{aligned} \quad (\text{S17})$$

With the above expansion, we denote the 0th-, 1st-, and 2nd-order terms to be the following

$$\int_{\mathbf{z} \in \mathbb{R}^d} w^{(2)}(\mathbf{x}, \mathbf{y}, \mathbf{z}) f_{xyz} dz = \int_{\mathbf{z} \in \mathbb{R}^d} w^{(2)}(\mathbf{x}, \mathbf{y}, \mathbf{z}) (f_{xyz}^{(0)} + f_{xyz}^{(1)} + f_{xyz}^{(2)}) dz + \mathcal{O}(\varepsilon^{4+d}). \quad (\text{S18})$$

Claim. The loop integral of the constant (0th-order) term $f_{xyz}^{(0)}$ is zero.

The above claim is true because

$$\begin{aligned} f_{xyz}^{(0)} &= \int_0^1 \sum_i f_i(\mathbf{u}(t)) (\mathbf{y} - \mathbf{x})_i dt + \int_0^1 \sum_i f_i(\mathbf{u}(1-t)) (\mathbf{z} - \mathbf{y})_i dt + \int_0^1 \sum_i f_i(\mathbf{u}(1-t)) (\mathbf{x} - \mathbf{z})_i dt \\ &= \int_0^1 \sum_i f_i(\mathbf{u}(t)) (\mathbf{y} - \mathbf{x})_i dt - \int_1^0 \sum_i f_i(\mathbf{u}(t)) (\mathbf{z} - \mathbf{y})_i dt - \int_1^0 \sum_i f_i(\mathbf{u}(t)) (\mathbf{x} - \mathbf{z})_i dt \\ &= \int_0^1 \sum_i f_i(u) \cdot (\mathbf{y} - \mathbf{x} + \mathbf{z} - \mathbf{y} + \mathbf{x} - \mathbf{z})_i dt = 0. \end{aligned}$$

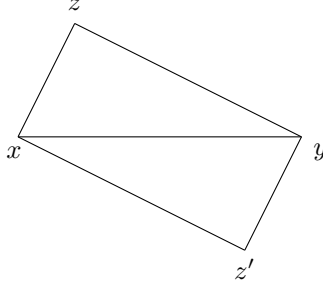
The second equation holds by changing the variable $1-t \rightarrow t$ for the second and third terms.

Claim. The integral of the first-order term $\int_{\mathbf{z} \in \mathbb{R}^d} w^{(2)}(\mathbf{x}, \mathbf{y}, \mathbf{z}) f_{xyz}^{(1)} dz$ is $\mathcal{O}(\varepsilon^{2+d}\delta)$.

The integral of the first order term is

$$\begin{aligned} \int_{\mathbf{z} \in \mathbb{R}^d} w^{(2)}(\mathbf{x}, \mathbf{y}, \mathbf{z}) f_{xyz}^{(1)} dz &= \int_{\mathbf{z} \in \mathbb{R}^d} w^{(2)}(\mathbf{x}, \mathbf{y}, \mathbf{z}) \int_0^1 \sum_i \sum_j \frac{\partial f_i(\mathbf{u}(1-t))}{\partial s_j} (\mathbf{v} - \mathbf{u}(1-t))_j (\mathbf{z} - \mathbf{y})_i dt \\ &\quad + \int_{\mathbf{z} \in \mathbb{R}^d} w^{(2)}(\mathbf{x}, \mathbf{y}, \mathbf{z}) \int_0^1 \sum_i \sum_j \frac{\partial f_i(\mathbf{u}(1-t))}{\partial s_j} (\mathbf{w} - \mathbf{u}(1-t))_j (\mathbf{x} - \mathbf{z})_i dt \\ &= \int_{\mathbf{z} \in \mathbb{R}^d} w^{(2)}(\mathbf{x}, \mathbf{y}, \mathbf{z}) \int_0^1 \sum_i \sum_j \frac{\partial f_i(\mathbf{u}(t))}{\partial s_j} (\mathbf{z} - \mathbf{x})_j (\mathbf{z} - \mathbf{y})_i (1-t) dt \\ &\quad - \int_{\mathbf{z} \in \mathbb{R}^d} w^{(2)}(\mathbf{x}, \mathbf{y}, \mathbf{z}) \int_0^1 \sum_i \sum_j \frac{\partial f_i(\mathbf{u}(1-t))}{\partial s_j} (\mathbf{z} - \mathbf{y})_j (\mathbf{z} - \mathbf{x})_i (1-t) dt. \end{aligned}$$

We can introduce a mirror node z' of z as follows.



The mirroring node has a property that $\mathbf{z}' - \mathbf{x} = -(\mathbf{z} - \mathbf{y})$ and $\mathbf{z}' - \mathbf{y} = -(\mathbf{z} - \mathbf{x})$. Using mirror node, the integral of the first-order term is

$$\begin{aligned} \int_{\mathbf{z} \in \mathbb{R}^d} w^{(2)}(\mathbf{x}, \mathbf{y}, \mathbf{z}) f_{xyz}^{(1)} d\mathbf{z} &= \int_{\mathbf{z} \in \mathbb{R}^d} w^{(2)}(\mathbf{x}, \mathbf{y}, \mathbf{z}) \int_0^1 \sum_i \sum_j \frac{\partial f_i(\mathbf{u}(t))}{\partial S_j} (\mathbf{z} - \mathbf{x})_j (\mathbf{z} - \mathbf{y})_i (1-t) dt \\ &\quad - \int_{\mathbf{z} \in \mathbb{R}^d} w^{(2)}(\mathbf{x}, \mathbf{y}, \mathbf{z}) \int_0^1 \sum_i \sum_j \frac{\partial f_i(\mathbf{u}(1-t))}{\partial S_j} (\mathbf{z} - \mathbf{x})_j (\mathbf{z} - \mathbf{y})_i (1-t) dt \\ &= \int_{\mathbf{z} \in \mathbb{R}^d} w^{(2)}(\mathbf{x}, \mathbf{y}, \mathbf{z}) \int_0^1 \sum_i \sum_j \left(\frac{\partial f_i(\mathbf{u}(t))}{\partial S_j} - \frac{\partial f_i(\mathbf{u}(1-t))}{\partial S_j} \right) (\mathbf{z} - \mathbf{x})_j (\mathbf{z} - \mathbf{y})_i (1-t) dt. \end{aligned}$$

Since $\frac{\partial f_i(\mathbf{u}(t))}{\partial S_j} - \frac{\partial f_i(\mathbf{u}(1-t))}{\partial S_j} = -\sum_k \frac{\partial^2 f_i(\mathbf{u}(t))}{\partial S_j \partial S_k} (\mathbf{y} - \mathbf{x})_k (1-2t) + \mathcal{O}(\delta^2)$, then the integral becomes

$$- \int_{\mathbf{z} \in \mathbb{R}^d} w^{(2)}(\mathbf{x}, \mathbf{y}, \mathbf{z}) \int_0^1 \sum_i \sum_j \sum_k \frac{\partial^2 f_i(\mathbf{u}(t))}{\partial S_j \partial S_k} (\mathbf{z} - \mathbf{x})_j (\mathbf{z} - \mathbf{y})_i (\mathbf{y} - \mathbf{x})_k (1-t)(1-2t) dt + \mathcal{O}(\varepsilon^{2+d}\delta^2).$$

We can decompose

$$\begin{aligned} \sum_i \sum_j \sum_k (\mathbf{z} - \mathbf{x})_j (\mathbf{z} - \mathbf{y})_i (\mathbf{y} - \mathbf{x})_k &= \sum_i \sum_{j \neq i} \sum_k (\mathbf{z} - \mathbf{x})_j (\mathbf{z} - \mathbf{x})_i (\mathbf{y} - \mathbf{x})_k \\ &\quad + \sum_i \sum_k (\mathbf{z} - \mathbf{x})_i^2 (\mathbf{y} - \mathbf{x})_k + \sum_i \sum_j \sum_k (\mathbf{z} - \mathbf{x})_j (\mathbf{x} - \mathbf{y})_i (\mathbf{y} - \mathbf{x})_k. \end{aligned}$$

(1) we firstly consider $\sum_i \sum_{j \neq i} \sum_k (\mathbf{z} - \mathbf{x})_j (\mathbf{z} - \mathbf{x})_i (\mathbf{y} - \mathbf{x})_k$ term.

When δ a relative small term for ε . The Taylor expansion of $k(\|\mathbf{z} - \mathbf{y}\|^2/\varepsilon^2)$ is

$$k(\|\mathbf{z} - \mathbf{y}\|^2/\varepsilon^2) = k(\|\mathbf{z} - \mathbf{x}\|^2/\varepsilon^2) + 2\varepsilon^{-2} k'(\|\mathbf{z} - \mathbf{x}\|^2/\varepsilon^2) (\mathbf{z} - \mathbf{x})^T (\mathbf{x} - \mathbf{y}) + \mathcal{O}\left(\frac{\delta^2 \|\mathbf{z} - \mathbf{x}\|^2}{\varepsilon^4}\right).$$

Since $\int_{\mathbf{z} \in \mathbb{R}^d} k^2(\|\mathbf{z} - \mathbf{x}\|^2/\varepsilon^2) (\mathbf{z} - \mathbf{x})_i (\mathbf{z} - \mathbf{x})_j (\mathbf{y} - \mathbf{x})_k = 0$ when $i \neq j$.

Additionally, $\int_{\mathbf{z} \in \mathbb{R}^d} k(\|\mathbf{z} - \mathbf{x}\|^2/\varepsilon^2) k'(\|\mathbf{z} - \mathbf{x}\|^2/\varepsilon^2) (\mathbf{z} - \mathbf{x})_i (\mathbf{z} - \mathbf{x})_j \sum_k (\mathbf{z} - \mathbf{x})_k (\mathbf{x} - \mathbf{y})_k = 0$ since it is odd function.

The last term $\int_{\mathbf{z} \in \mathbb{R}^d} k(\|\mathbf{z} - \mathbf{x}\|^2/\varepsilon^2) (\mathbf{z} - \mathbf{x})_i (\mathbf{z} - \mathbf{x})_j (\mathbf{y} - \mathbf{x})_k \mathcal{O}\left(\frac{\delta^2 \|\mathbf{z} - \mathbf{x}\|^2}{\varepsilon^4}\right) = \mathcal{O}(\varepsilon^d \delta^3)$.

(2) Then consider $\sum_i \sum_j \sum_k (\mathbf{z} - \mathbf{x})_j (\mathbf{x} - \mathbf{y})_i (\mathbf{y} - \mathbf{x})_k$ term, which is $\mathcal{O}(\varepsilon^d \delta^3)$, the second term in the expansion of $k(\|\mathbf{z} - \mathbf{y}\|^2/\varepsilon^2)$ will result in $\mathcal{O}(\varepsilon^d \delta^3)$.

$$\int_{\mathbf{z} \in \mathbb{R}^d} k(\|\mathbf{z} - \mathbf{x}\|^2/\varepsilon^2) \frac{2}{\varepsilon^2} \sum_{l,i,j,k} (\mathbf{z} - \mathbf{x})_l (\mathbf{x} - \mathbf{y})_l (\mathbf{z} - \mathbf{x})_j (\mathbf{x} - \mathbf{y})_i (\mathbf{y} - \mathbf{x})_k dt d\mathbf{z} = \mathcal{O}(\varepsilon^d \delta^3).$$

And the first term of the expansion will result in 0 and the second term will also result in $\mathcal{O}(\varepsilon^d \delta^3)$.

(3) Next, we consider

$$\int_{\mathbf{z} \in \mathbb{R}^d} w^{(2)}(\mathbf{x}, \mathbf{y}, \mathbf{z}) \int_0^1 \sum_i \sum_k \frac{\partial^2 f_i(\mathbf{u}(t))}{\partial S_j \partial S_k} (\mathbf{z} - \mathbf{x})_i^2 (\mathbf{y} - \mathbf{x})_k (1-t)(1-2t) dt d\mathbf{z}.$$

We can define

$$C_1 = \frac{1}{\varepsilon^{2+d}} \int_{\mathbf{z} \in \mathbb{R}^d} k^2(\|\mathbf{z} - \mathbf{x}\|^2/\varepsilon^2) (\mathbf{z} - \mathbf{x})_i^2 d\mathbf{z}.$$

And the second term of expansion of $k(\|\mathbf{z} - \mathbf{y}\|^2/\varepsilon^2)$ would result in 0 and third term will result in $\mathcal{O}(\varepsilon^d \delta^3)$. Hence,

$$\begin{aligned} & \int_{z \in \mathbb{R}^d} w^{(2)}(x, y, z) \int_0^1 \sum_i \sum_k \frac{\partial^2 f_i(u(t))}{\partial S_j \partial S_k} (z-x)_i^2 (y-x)_k (1-t)(1-2t) dt dz \\ &= \varepsilon^{2+d} C_1 \int_0^1 \sum_i \sum_j \frac{\partial^2 f_j(u(t))}{\partial S_i \partial S_j} (y-x)_i (1-t)(1-2t) dt + \mathcal{O}(\varepsilon^d \delta^3). \end{aligned}$$

In short, the first order term

$$\int_{\mathbf{z} \in \mathbb{R}^d} w^{(2)}(\mathbf{x}, \mathbf{y}, \mathbf{z}) f_{xyz}^1 dz = -\varepsilon^{2+d} C_1 \int_0^1 \sum_i \sum_j \frac{\partial^2 f_j(\mathbf{u}(t))}{\partial S_i \partial S_j} (\mathbf{y} - \mathbf{x})_i (1-t)(1-2t) dt + \mathcal{O}(\varepsilon^d \delta^3).$$

Claim. The integral of the second-order term $\int_{\mathbf{z} \in \mathbb{R}^d} w^{(2)}(\mathbf{x}, \mathbf{y}, \mathbf{z}) f_{xyz}^{(2)} d\mathbf{z}$ is $\mathcal{O}(\varepsilon^{2+d} \delta)$.

The integral of the second-order term is

$$\begin{aligned} & \int_{\mathbf{z} \in \mathbb{R}^d} w^{(2)}(\mathbf{x}, \mathbf{y}, \mathbf{z}) f_{xyz}^{(2)} d\mathbf{z} \\ &= \int_{\mathbf{z} \in \mathbb{R}^d} w^{(2)}(\mathbf{x}, \mathbf{y}, \mathbf{z}) \int_0^1 \sum_i \sum_j \sum_k \frac{\partial^2 f_i(\mathbf{u}(1-t))}{\partial S_j \partial S_k} (\mathbf{v} - \mathbf{u}(1-t))_j (\mathbf{v} - \mathbf{u}(1-t))_k (\mathbf{z} - \mathbf{y})_i dt d\mathbf{z} \\ &+ \int_{\mathbf{z} \in \mathbb{R}^d} w^{(2)}(\mathbf{x}, \mathbf{y}, \mathbf{z}) \int_0^1 \sum_i \sum_j \sum_k \frac{\partial^2 f_i(\mathbf{u}(1-t))}{\partial S_j \partial S_k} (\mathbf{w} - \mathbf{u}(1-t))_j (\mathbf{w} - \mathbf{u}(1-t))_k (\mathbf{x} - \mathbf{z})_i dt d\mathbf{z} \\ &= \int_{\mathbf{z} \in \mathbb{R}^d} w^{(2)}(\mathbf{x}, \mathbf{y}, \mathbf{z}) \int_0^1 \sum_i \sum_j \sum_k \frac{\partial^2 f_i(\mathbf{u}(t))}{\partial S_j \partial S_k} (\mathbf{z} - \mathbf{x})_j (\mathbf{z} - \mathbf{x})_k (\mathbf{z} - \mathbf{y})_i (1-t)^2 dt d\mathbf{z} \\ &- \int_{\mathbf{z} \in \mathbb{R}^d} w^{(2)}(\mathbf{x}, \mathbf{y}, \mathbf{z}) \int_0^1 \sum_i \sum_j \sum_k \frac{\partial^2 f_i(\mathbf{u}(t))}{\partial S_j \partial S_k} (\mathbf{z} - \mathbf{y})_j (\mathbf{z} - \mathbf{y})_k (\mathbf{z} - \mathbf{x})_i t^2 dt d\mathbf{z}. \end{aligned}$$

We can decompose the second-order term into the following terms

$$= \int_{\mathbf{z} \in \mathbb{R}^d} w^{(2)}(\mathbf{x}, \mathbf{y}, \mathbf{z}) \int_0^1 \sum_i \sum_j \sum_k \frac{\partial^2 f_i(\mathbf{u}(t))}{\partial S_j \partial S_k} (\mathbf{z} - \mathbf{x})_j (\mathbf{z} - \mathbf{x})_k (\mathbf{z} - \mathbf{x})_i (1-t)^2 dt d\mathbf{z} \quad (\text{S19})$$

$$- \int_{\mathbf{z} \in \mathbb{R}^d} w^{(2)}(\mathbf{x}, \mathbf{y}, \mathbf{z}) \int_0^1 \sum_i \sum_j \sum_k \frac{\partial^2 f_i(\mathbf{u}(t))}{\partial S_j \partial S_k} (\mathbf{z} - \mathbf{x})_j (\mathbf{z} - \mathbf{x})_k (\mathbf{y} - \mathbf{x})_i (1-t)^2 dt d\mathbf{z} \quad (\text{S20})$$

$$- \int_{\mathbf{z} \in \mathbb{R}^d} w^{(2)}(\mathbf{x}, \mathbf{y}, \mathbf{z}) \int_0^1 \sum_i \sum_j \sum_k \frac{\partial^2 f_i(\mathbf{u}(t))}{\partial S_j \partial S_k} (\mathbf{z} - \mathbf{y})_j (\mathbf{z} - \mathbf{y})_k (\mathbf{z} - \mathbf{y})_i t^2 dt d\mathbf{z} \quad (\text{S21})$$

$$- \int_{\mathbf{z} \in \mathbb{R}^d} w^{(2)}(\mathbf{x}, \mathbf{y}, \mathbf{z}) \int_0^1 \sum_i \sum_j \sum_k \frac{\partial^2 f_i(\mathbf{u}(t))}{\partial S_j \partial S_k} (\mathbf{z} - \mathbf{y})_j (\mathbf{z} - \mathbf{y})_k (\mathbf{y} - \mathbf{x})_i t^2 dt d\mathbf{z}. \quad (\text{S22})$$

Using property of mirror nodes $\mathbf{z} - \mathbf{y} = -(\mathbf{z}' - \mathbf{x})$, we can combine (S19) and (S21) to get

$$\int_{\mathbf{z} \in \mathbb{R}^d} w^{(2)}(\mathbf{x}, \mathbf{y}, \mathbf{z}) \int_0^1 \sum_i \sum_j \sum_k \frac{\partial^2 f_i(\mathbf{u}(t))}{\partial S_j \partial S_k} (\mathbf{z} - \mathbf{x})_j (\mathbf{z} - \mathbf{x})_k (\mathbf{z} - \mathbf{x})_i (t^2 + (1-t)^2) dt d\mathbf{z}.$$

Recall that the Taylor expansion of $\kappa(\|\mathbf{z} - \mathbf{y}\|^2/\varepsilon^2)$, the first term will be 0 and the third term will result in $\mathcal{O}(\delta^2 \varepsilon^{d+1})$, we only need to consider the second term, the sum of (S19) and (S21) becomes

$$2\varepsilon^{-2} \int_{\mathbf{z} \in \mathbb{R}^d} \kappa \kappa' \int_0^1 \sum_{i,j,k,l} \frac{\partial^2 f_i(\mathbf{u}(t))}{\partial S_j \partial S_k} (\mathbf{z} - \mathbf{x})_i (\mathbf{z} - \mathbf{x})_j (\mathbf{z} - \mathbf{x})_k (\mathbf{z} - \mathbf{x})_l (\mathbf{x} - \mathbf{y})_l (t^2 + (1-t)^2) dt d\mathbf{z}.$$

The following four conditions will make the above integral non-zero: (i) $i = j \neq k = l$, (ii) $i = k \neq j = l$, (iii) $i = l \neq j = k$, and (iv) $i = j = k = l$.

Firstly, if $\kappa_\varepsilon(\cdot)$ is the exponential kernel, we define

$$C_2 = \varepsilon^{-(4+d)} \int_{\mathbf{z} \in \mathbb{R}^d} \kappa^2 \left(\frac{\|\mathbf{z}\|^2}{\varepsilon^2} \right) \mathbf{z}_1^2 \mathbf{z}_2^2$$

$$C_3 = \varepsilon^{-(4+d)} \int_{\mathbf{z} \in \mathbb{R}^d} \kappa^2 \left(\frac{\|\mathbf{z}\|^2}{\varepsilon^2} \right) \mathbf{z}_1^4.$$

Since we have

$$\iint \exp(-2x^2 - 2y^2) x^4 dx dy = \frac{3\pi}{32};$$

$$\iint \exp(-2x^2 - 2y^2) x^2 y^2 dx dy = \frac{\pi}{32};$$

$$\iint \exp(-2x^2 - 2y^2) x^2 dx dy = \frac{\pi}{8}.$$

It implies that $C_3 - 3C_2$ is zero when $d = 2$. For general dimensions ($d > 2$), one can use the identity

$$\int_{\mathbf{x} \in \mathbb{R}^d} \exp(-2\|\mathbf{x}\|^2) g(x_1, x_2) d\mathbf{x} = \left(\frac{\sqrt{2\pi}}{4} \right)^{d-2} \iint \exp(-2x_1^2 - 2x_2^2) g(x_1, x_2) dx_1 dx_2.$$

Therefore, $C_3 - 3C_2 = \varepsilon^{-(4+d)} \int_{\mathbf{z} \in \mathbb{R}^d} \exp(-2\|\mathbf{z}\|^2) (z_1^4 - 3z_1^2 z_2^2) d\mathbf{z} = 0$ with the exponential kernel.

Similarly, we have

$$C_1 - 4C_2 = \varepsilon^{-(d+2)} \int_{\mathbf{z} \in \mathbb{R}^d} \exp(-2\|\mathbf{z}\|^2) z_1^2 - 4\varepsilon^{-(d+4)} \int_{\mathbf{z} \in \mathbb{R}^d} \exp(-2\|\mathbf{z}\|^2) z_1^2 z_2^2 = 0. \quad (\text{S23})$$

Then we inspect condition (i). The integration is

$$2\varepsilon^{2+d} C_2 \int_0^1 \sum_i \sum_{j \neq i} \frac{\partial^2 f_j(\mathbf{u}(t))}{\partial S_i \partial S_j} (\mathbf{y} - \mathbf{x})_i (t^2 + (1-t)^2) dt d\mathbf{z}.$$

In (ii), the integral is the same as the integral of (i), so the sum of (i) and (ii) is

$$4\varepsilon^{2+d} C_2 \int_0^1 \sum_i \sum_{j \neq i} \frac{\partial^2 f_j(\mathbf{u}(t))}{\partial S_i \partial S_j} (\mathbf{y} - \mathbf{x})_i (t^2 + (1-t)^2) dt d\mathbf{z}.$$

For condition (iii), the integral is

$$2\varepsilon^{2+d} C_2 \int_0^1 \sum_i \sum_{j \neq i} \frac{\partial^2 f_i(\mathbf{u}(t))}{\partial S_j^2} (\mathbf{y} - \mathbf{x})_i (t^2 + (1-t)^2) dt d\mathbf{z}.$$

For condition (iv), the integral is

$$2\varepsilon^{2+d} C_3 \int_0^1 \sum_i \frac{\partial^2 f_i(\mathbf{u}(t))}{\partial S_i^2} (\mathbf{y} - \mathbf{x})_i (t^2 + (1-t)^2) dt d\mathbf{z}.$$

From the fact $C_3 = 3C_2$, the sum of (S19) and (S21) is

$$4\varepsilon^{2+d}C_2 \int_0^1 \sum_i \sum_j \frac{\partial^2 f_j(\mathbf{u}(t))}{\partial S_i \partial S_j} (\mathbf{y} - \mathbf{x})_i (t^2 + (1-t)^2) dt d\mathbf{z}$$

$$+ 2\varepsilon^{2+d}C_2 \int_0^1 \sum_i \sum_j \frac{\partial^2 f_i(\mathbf{u}(t))}{\partial S_j^2} (\mathbf{y} - \mathbf{x})_i (t^2 + (1-t)^2) dt d\mathbf{z}.$$

The sum of (S20) and (S22) is

$$- \int_{\mathbf{z} \in \mathbb{R}^d} w^{(2)}(\mathbf{x}, \mathbf{y}, \mathbf{z}) \int_0^1 \sum_i \sum_j \sum_k \frac{\partial^2 f_i(\mathbf{u}(t))}{\partial S_j \partial S_k} (\mathbf{z} - \mathbf{x})_j (\mathbf{z} - \mathbf{x})_k (\mathbf{y} - \mathbf{x})_i ((1-t)^2 + t^2) dt d\mathbf{z}.$$

Similar to what we do in the first order term, we can get the sum of (S20) and (S22) is

$$-\varepsilon^{2+d}C_1 \int_0^1 \sum_i \sum_j \frac{\partial^2 f_i(\mathbf{u}(t))}{\partial S_j^2} (\mathbf{y} - \mathbf{x})_i (t^2 + (1-t)^2) dt d\mathbf{z}.$$

Therefore, sum the first order and second order term up, we obtain

$$2\varepsilon^{2+d}C_2 \int_0^1 \sum_i \sum_j \frac{\partial^2 f_j(\mathbf{u}(t))}{\partial S_i \partial S_j} (\mathbf{y} - \mathbf{x})_i (t^2 + (1-t)^2) dt d\mathbf{z}$$

$$+ \varepsilon^{2+d}C_2 \int_0^1 \sum_i \sum_j \frac{\partial^2 f_i(\mathbf{u}(t))}{\partial S_j^2} (\mathbf{y} - \mathbf{x})_i (t^2 + (1-t)^2) dt d\mathbf{z}$$

$$- \frac{1}{2}\varepsilon^{2+d}C_1 \int_0^1 \sum_i \sum_j \frac{\partial^2 f_i(\mathbf{u}(t))}{\partial S_j^2} (\mathbf{y} - \mathbf{x})_i (t^2 + (1-t)^2) dt d\mathbf{z}$$

$$- \varepsilon^{2+d}C_1 \int_0^1 \sum_i \sum_j \frac{\partial^2 f_j(\mathbf{u}(t))}{\partial S_i \partial S_j} (\mathbf{y} - \mathbf{x})_i (1-t)(1-2t) dt.$$

Note that

$$C_1 - 4C_2 = \varepsilon^{-(d+2)} \int_{\mathbf{z} \in \mathbb{R}^d} \exp(-2\|\mathbf{z}\|^2) z_1^2 - 4\varepsilon^{-(d+4)} \int_{\mathbf{z} \in \mathbb{R}^d} \exp(-2\|\mathbf{z}\|^2) z_1^2 z_2^2 = 0.$$

The $t^2 + (1-t)^2 = 1 - 2t(1-t)$ term and $(1-t)(1-2t)$ term in the line integral can be removed with the following technique. Let $g_{ij}(\mathbf{u}(t)) = \frac{\partial^2 f_i(\mathbf{u}(t))}{\partial S_j^2}$ and $\tau = t - 1/2$. Considering the integral term contains $t(1-t)$, we have

$$\int_0^1 g_{ij}(\mathbf{u}(t)) t(1-t) dt = \int_0^1 g_{ij} \left(\frac{\mathbf{x} + \mathbf{y}}{2} + (\mathbf{y} - \mathbf{x})\tau \right) \left(\frac{1}{4} - \tau^2 \right) d\tau.$$

The $1/4$ terms become an unbiased line integral, i.e., $\frac{1}{4} \int_0^1 g_{ij}(\mathbf{u}(t)) dt$. Therefore, we can focus only on the τ^2 part. Taylor expanding the g_{ij} yields

$$\int_{-1/2}^{1/2} \tau^2 \left[g_{ij} \left(\frac{\mathbf{x} + \mathbf{y}}{2} \right) + \tau (\mathbf{y} - \mathbf{x})^\top \nabla g_{ij} + \mathcal{O}(\|\mathbf{y} - \mathbf{x}\|^2) \right] d\tau = \frac{1}{12} \cdot g_{ij} \left(\frac{\mathbf{x} + \mathbf{y}}{2} \right).$$

The first-order term becomes zero using the odd function symmetry, and the term $1/12$ comes from $\int_{-1/2}^{1/2} \tau^2 d\tau$. By Jensen's inequality, we have $g_{ij}((\mathbf{x} + \mathbf{y})/2) = \frac{1}{2}(g_{ij}(\mathbf{x}) + g_{ij}(\mathbf{y})) + \mathcal{O}(\|\mathbf{y} - \mathbf{x}\|^2)$. Therefore,

$$\begin{aligned} \sum_i \int_{-1/2}^{1/2} g_{ij}(\mathbf{u}(\tau)) (\mathbf{y} - \mathbf{x})_i \tau^2 d\tau &= \frac{1}{12} \cdot \frac{1}{2} (g_{ij}(\mathbf{x}) + g_{ij}(\mathbf{y})) (\mathbf{y} - \mathbf{x})_i + \mathcal{O}(\delta^2) \\ &= \frac{1}{12} \sum_i \int_0^1 [g_{ij}(\mathbf{x}) + (g_{ij}(\mathbf{y}) - g_{ij}(\mathbf{x}))t] (\mathbf{y} - \mathbf{x})_i dt + \mathcal{O}(\delta^2) \\ &= \frac{1}{12} \sum_i \int_0^1 g_{ij}(\mathbf{u}(t)) (\mathbf{y} - \mathbf{x})_i dt + \mathcal{O}(\delta^2). \end{aligned}$$

The last equality holds from Lemma S11. Now we have,

$$\int_0^1 \sum_i g_{ij}(\mathbf{u}(t))(\mathbf{y} - \mathbf{x})_i t(1-t) dt = \left(\frac{1}{4} - \frac{1}{12}\right) \int_0^1 \sum_i g_{ij}(\mathbf{u}(t))(\mathbf{y} - \mathbf{x})_i dt + \mathcal{O}(\delta^2).$$

Finally, using the fact that $t^2 + (1-t)^2 = 1 - 2t(1-t)$, we get

$$\begin{aligned} & \varepsilon^{2+d} C_2 \int_0^1 \sum_i \sum_j \frac{\partial^2 f_i}{\partial S_j^2}(\mathbf{u}(t))(\mathbf{y} - \mathbf{x})_i (t^2 + (1-t)^2) dt \\ &= \frac{2}{3} \varepsilon^{2+d} C_2 \int_0^1 \sum_i \sum_j \frac{\partial^2 f_i}{\partial S_j^2}(\mathbf{u}(t))(\mathbf{y} - \mathbf{x})_i dt + \mathcal{O}(\varepsilon^{2+d} \delta^2). \end{aligned}$$

Similarly, we can remove $(1-t)(1-2t)$ term by

$$\begin{aligned} & \varepsilon^{2+d} C_1 \int_0^1 \sum_i \sum_j \frac{\partial^2 f_j}{\partial S_i \partial S_j}(\mathbf{u}(t))(\mathbf{y} - \mathbf{x})_i (1-t)(1-2t) dt \\ &= \frac{1}{6} \varepsilon^{2+d} C_2 \int_0^1 \sum_i \sum_j \frac{\partial^2 f_j}{\partial S_i \partial S_j}(\mathbf{u}(t))(\mathbf{y} - \mathbf{x})_i dt + \mathcal{O}(\varepsilon^{2+d} \delta^2). \end{aligned}$$

Remark. Note that the $2/3$ term corresponds to $\int_0^1 t^2 + (1-t)^2 dt$. The result can be interpreted as follows. When \mathbf{x} is sufficiently close to \mathbf{y} , the $g_{ij}(\mathbf{u}(t))$ term is roughly a constant. Therefore, the integral can be approximately done separately, i.e., $\int_0^1 g_{ij}(\mathbf{u}(t))(t^2 + (1-t)^2) dt \approx \int_0^1 (t^2 + (1-t)^2) dt \int_0^1 g_{ij}(\mathbf{u}(t)) dt = \frac{2}{3} \int_0^1 g_{ij}(\mathbf{u}(t)) dt$.

The proof is thus completed by putting things together.

$$\begin{aligned} \int_{\mathbf{z} \in \mathbb{R}^d} w_T(\mathbf{x}, \mathbf{y}, \mathbf{z}) f_{xyz} d\mu(\mathbf{z}) &= \frac{2}{3} \varepsilon^{2+d} C_2 \int_0^1 \sum_i \sum_j \left(\frac{\partial^2 f_j}{\partial S_i \partial S_j}(\mathbf{u}(t)) - \frac{\partial^2 f_i}{\partial S_j^2}(\mathbf{u}(t)) \right) (\mathbf{y} - \mathbf{x})_i dt \\ &\quad + \mathcal{O}(\varepsilon^d \delta^3) + \mathcal{O}(\varepsilon^{4+d}) + \mathcal{O}(\varepsilon^{2+d} \delta^2). \end{aligned}$$

Using Proposition S7 $\delta d\zeta_1 = \sum_i \sum_{j \neq i} \left(\frac{\partial^2 f_j}{\partial S_i \partial S_j} - \frac{\partial^2 f_i}{\partial S_j^2} \right) ds_i$, one can get following asymptotic expansion

$$\begin{aligned} \int_{\mathbf{z} \in \mathbb{R}^d} w_T(\mathbf{x}, \mathbf{y}, \mathbf{z}) f_{xyz} d\mu(\mathbf{z}) &= \frac{2}{3} \varepsilon^{2+d} C_2 \int_0^1 [(\delta d v(\mathbf{u}(t)))]^\top \mathbf{u}'(t) dt \\ &\quad + \mathcal{O}(\varepsilon^d \delta^3) + \mathcal{O}(\varepsilon^{4+d}) + \mathcal{O}(\varepsilon^{2+d} \delta^2). \end{aligned}$$

This completes the proof. ■

The second step is to provide the error terms induced by the change of variables from the ambient space $\mathcal{M} \subseteq \mathbb{R}^D$ to the local tangent coordinate $\mathcal{T}_x \mathcal{M} \in \mathbb{R}^d$ defined by \mathbf{x} . In the following, there are two coordinate systems that we mainly focus on: the *normal coordinate* and *tangent plane coordinate* at \mathbf{x} . First, we define $\mathbf{x}, \mathbf{y}, \mathbf{z} \in \mathcal{M} \subseteq \mathbb{R}^D$ to be the points in the *ambient space*. We then let $\mathbf{x}_s, \mathbf{y}_s, \mathbf{z}_s \in \mathbb{R}^d$ be the same set of points in the *normal coordinate* in the neighborhood of point \mathbf{x} . Points in the *tangent plane coordinate* defined by tangent plane $\mathcal{T}_x \mathcal{M}$ of \mathbf{x} are denoted $\mathbf{x}_p, \mathbf{y}_p, \mathbf{z}_p \in \mathbb{R}^d$. Note that by definition, the origin of these two coordinate systems is \mathbf{x} , implying that $\mathbf{x}_s, \mathbf{x}_p$ are zero vectors. The following lemma generalizes the result in [CL06] for triangular relations $\mathbf{x}, \mathbf{y}, \mathbf{z}$.

Lemma S13 (Error terms induced from the change of coordinates). *Define $Q_{\mathbf{x}, m}(\cdot)$ be a homogenous polynomial of order m with coefficient defined by \mathbf{x} . Further, let γ be a geodesic curve in \mathcal{M} connecting two points $\mathbf{a} \in \{\mathbf{x}, \mathbf{y}, \mathbf{z}\}$ and $\mathbf{b} \in \{\mathbf{x}, \mathbf{y}, \mathbf{z}\}$. If $\mathbf{y}, \mathbf{z} \in \mathcal{M}$ are in a Euclidean ball of radius ε around \mathbf{x} , then for ε sufficiently small, we have the following four approximations.*

$$[\mathbf{z}_s]_i = [\mathbf{z}_p]_i + \mathcal{O}(\varepsilon^3); \tag{S24a}$$

$$\det \left(\frac{d\mathbf{z}}{d\mathbf{z}_p} \right) = 1 + Q_{\mathbf{x}, 2}(\mathbf{z}_p) + \mathcal{O}(\varepsilon^3); \tag{S24b}$$

$$\|\mathbf{a} - \mathbf{b}\|^2 = \|\mathbf{a}_p - \mathbf{b}_p\|^2 + Q_{\mathbf{x}, 4}(\mathbf{a}_p, \mathbf{b}_p) + \mathcal{O}(\varepsilon^5); \tag{S24c}$$

$$\gamma(t) = \mathbf{a}_p + (\mathbf{b}_p - \mathbf{a}_p)t + \mathcal{O}(\varepsilon^3). \tag{S24d}$$

Proof. (S24a) and (S24b) follow naturally from Lemma 6 and 7 of [CL06] since there is no triplet-wise $(\mathbf{x}, \mathbf{y}, \mathbf{z})$ relationship.

For (S24c), if either $\mathbf{a} = \mathbf{x}$ or $\mathbf{b} = \mathbf{x}$ the result follows from Lemma 7 of [CL06]. Now we consider the case that neither \mathbf{a} nor \mathbf{b} are equal to \mathbf{x} . Without loss of generality, let $\mathbf{a} = \mathbf{z}$ and $\mathbf{b} = \mathbf{y}$. Note that the submanifold in the ambient space is locally parameterized by $(\mathbf{v}_p, g(\mathbf{v}_p)) \in \mathbb{R}^D$ for $g : \mathbb{R}^d \rightarrow \mathbb{R}^{D-d}$. Since \mathbf{z} is not the original of the normal coordinate system, one can do a Taylor expansion of g from \mathbf{x}_p . Denote by $\mathbf{s} = (s_1, \dots, s_d)$ the local coordinate of $\mathcal{T}_x\mathcal{M}$ at point \mathbf{x} . By definition, we have $g_i(\mathbf{x}_p) = 0$ and $\frac{\partial g_i(\mathbf{x}_p)}{\partial s_j} = 0$ for $i, j \in [d]$. We write $g_i(\mathbf{z}_p) = H_{i,\mathbf{x}}(\mathbf{z}_p) + \mathcal{O}(\varepsilon^3)$, and $g_i(\mathbf{y}) = H_{i,\mathbf{x}}(\mathbf{y}_p) + \mathcal{O}(\varepsilon^3)$ by Taylor expansion. Here, H is the Hessian of g_i at the origin. Hence, we have $\|\mathbf{z} - \mathbf{y}\|^2 = \|\mathbf{z}_p - \mathbf{y}_p\|^2 + \sum_{i=d+1}^D (g_i(\mathbf{z}_p) - g_i(\mathbf{y}_p))^2 = \|\mathbf{z} - \mathbf{y}\|^2 + Q_{\mathbf{x},4}(\mathbf{y}_p, \mathbf{z}_p) + \mathcal{O}(\varepsilon^5)$.

To prove (S24d), first, note that one can project the geodesic onto $\mathcal{T}_x\mathcal{M}$ with $\mathcal{O}(\varepsilon^3)$ by (S24a), i.e., $\gamma = \gamma_{\mathcal{T}_x\mathcal{M}}(t) + \mathcal{O}(\varepsilon^3)$. Therefore, we only need to consider the error term caused by approximating the projected geodesic $\gamma_{\mathcal{T}_x\mathcal{M}}(t)$ by a straight line $\mathbf{a}_p + (\mathbf{b}_p - \mathbf{a}_p)t$. Denote $\gamma_{\mathcal{T}_x\mathcal{M}} = \gamma_{\mathcal{T}}$ for simplicity, further let $\text{dist}_{\mathcal{T}}(\mathbf{y}, \mathbf{z})$ be the arc length of the projected geodesic $\gamma_{\mathcal{T}}$ connecting $\mathbf{a}_p, \mathbf{b}_p$, from Taylor expansion, one has

$$\gamma_{\mathcal{T}}(t) = \gamma_{\mathcal{T}}(0) + t\gamma'_{\mathcal{T}}(0)\text{dist}_{\mathcal{T}}(\mathbf{a}_p, \mathbf{b}_p) + \frac{1}{2}t^2\text{dist}_{\mathcal{T}}^2(\mathbf{a}_p, \mathbf{b}_p)\gamma''_{\mathcal{T}}(0) + \mathcal{O}(\varepsilon^3). \quad (\text{S25})$$

The first step is to show that $\gamma''_{\mathcal{T}}(0) = \mathcal{O}(\varepsilon)$. Since $\text{dist}_{\mathcal{T}}(\mathbf{a}_p, \mathbf{b}_p) = \mathcal{O}(\varepsilon)$, if $\gamma''_{\mathcal{T}}(0) = \mathcal{O}(\varepsilon)$, one can bound the second-order term by $\mathcal{O}(\varepsilon^3)$. Note that if $\mathbf{a} = \mathbf{x}$, by the definition of geodesic (covariant derivative is normal to \mathcal{M}), we have $\gamma''_{\mathcal{T}}(0) = 0$. Hence, the error term is bounded by $\mathcal{O}(\varepsilon^3)$. If $\mathbf{b} = \mathbf{x}$, one can switch \mathbf{b} with \mathbf{a} , and the same proof can go through. We now deal with the situation when $\mathbf{a}, \mathbf{b} \neq \mathbf{x}$. One can show that the *Levi-Civita connection* of the local (orthonormal) basis vector can be written as a linear combination of the basis vectors by the *method of moving frame* [Cle17], with coefficients determined by the local curvature/torsion at that point. The first-order approximation of the local basis vector $[\mathbf{e}_a]_i \in \mathbb{R}^D$ for $i \in [d]$ at \mathbf{a} can be approximated by $[\mathbf{e}_a]_i = [\mathbf{e}_x]_i + \mathcal{O}(\varepsilon)$ using the *method of moving frame* along the geodesic connecting $\mathbf{x} \rightarrow \mathbf{a}$. By the Gram-Schmidt process, the basis of the normal space $[\mathbf{n}_a]_j \in \mathbb{R}^D$ at \mathbf{a} for $j = d+1, \dots, D$ can also be written as a first-order approximation of the normal basis at \mathbf{x} , i.e., $[\mathbf{n}_a]_j = [\mathbf{n}_x]_j + \mathcal{O}(\varepsilon)$. Since the second derivate of geodesic $\gamma''_{\mathcal{M}}(0)$ at \mathbf{a} is in the normal space $\mathcal{T}_a^\perp\mathcal{M}$, the covariant derivative of the projected geodesic $\gamma''(0)$ at \mathbf{a} onto $\mathcal{T}_x\mathcal{M}$ can be bounded by $\mathcal{O}(\varepsilon)$ if the manifold \mathcal{M} has bounded curvature. The term including $\gamma''(0)$ can thus be bounded by $\mathcal{O}(\varepsilon^3)$, given that \mathbf{a} and \mathbf{b} are sufficiently close to \mathbf{x} . Hence, (S25) becomes

$$\gamma_{\mathcal{T}}(t) = \gamma_{\mathcal{T}}(0) + t\gamma'_{\mathcal{T}}(0)\text{dist}_{\mathcal{T}}(\mathbf{a}_p, \mathbf{b}_p) + \mathcal{O}(\varepsilon^3).$$

Plugging in $t = 1$ gives us $\gamma'(0)\text{dist}_{\mathcal{T}}(\mathbf{a}_p, \mathbf{b}_p) = \mathbf{b}_p - \mathbf{a}_p + \mathcal{O}(\varepsilon^3)$. The following approximation of $\gamma(t)$ thus holds.

$$\gamma(t) = \mathbf{a}_p + (\mathbf{b}_p - \mathbf{a}_p)t + \mathcal{O}(\varepsilon^3).$$

This completes the proof. ■

With the above two lemmas in hand, we can finally start to prove Proposition 2.

Proof of Proposition 2. Note that from (S24d), the geodesic curve can be approximated by a straight line in the local tangent plane $\mathcal{T}_x\mathcal{M}$ with error $\mathcal{O}(\varepsilon^3)$. Therefore, $f_{xyz} = \oint_{\mathcal{M}} v = f_{x_p y_p z_p} + \mathcal{O}(\varepsilon^4)$. A similar expansion as in Lemma S12 thus holds. Let $\kappa_\varepsilon(\mathbf{z}, \mathbf{x}) = \kappa\left(\frac{\|\mathbf{z} - \mathbf{x}\|^2}{\varepsilon^2}\right)$, from a similar

analysis as Lemma S12, we have

$$\begin{aligned}
& \int_{\mathbf{z} \in \mathcal{M}} w_T(\mathbf{x}, \mathbf{y}, \mathbf{z}) f_{xyz} d\mathbf{z} \stackrel{(i)}{=} \int_{\substack{\mathbf{z} \in \mathcal{M} \\ \max(\|\mathbf{z}-\mathbf{y}\|, \|\mathbf{z}-\mathbf{x}\|) < \varepsilon^\gamma}} w_T(\mathbf{x}, \mathbf{y}, \mathbf{z}) f_{xyz} d\mathbf{z} + \mathcal{O}(\varepsilon^{4+d}) \\
& \stackrel{(ii)}{=} \int_{\mathbf{z} \in \mathbb{R}^d} \left[\left(\kappa_\varepsilon(\mathbf{z}, \mathbf{x}) \kappa_\varepsilon(\mathbf{z}, \mathbf{y}) + \left(\frac{Q_{\mathbf{x},4}(\mathbf{z}, \mathbf{y})}{\varepsilon^2} \right) (\kappa'_\varepsilon(\mathbf{z}, \mathbf{x}) \kappa_\varepsilon(\mathbf{z}, \mathbf{y}) + \kappa_\varepsilon(\mathbf{z}, \mathbf{x}) \kappa'_\varepsilon(\mathbf{z}, \mathbf{y})) \right) \right. \\
& \quad \left. \cdot f_{xyz} \cdot ((1 + Q_{\mathbf{x},2}(\mathbf{z}))) \right] d\mathbf{z} + \mathcal{O}(\varepsilon^{4+d}) \\
& = \frac{2}{3} \varepsilon^{2+d} C_2 \int_0^1 [(\delta d v(\mathbf{u}(t)))]^\top \mathbf{u}'(t) dt + \mathcal{O}(\varepsilon^d \delta^3) + \mathcal{O}(\varepsilon^{4+d}) + \mathcal{O}(\varepsilon^{2+d} \delta^2).
\end{aligned}$$

Equality (i) holds by Lemma S10. Equality (ii) is valid by first projecting $\mathbf{x}, \mathbf{y}, \mathbf{z}$ to $\mathcal{T}_{\mathbf{x}}\mathcal{M}$, changing the variables $\mathbf{x}_p, \mathbf{y}_p, \mathbf{z}_p \rightarrow \mathbf{x}, \mathbf{y}, \mathbf{z}$, and using Lemma (S10) again. Terms consisting of $Q_{p,4}(\mathbf{x}, \mathbf{y})$ or $Q_{p,2}(\mathbf{x}, \mathbf{y})$ are in the high order, hence, they can be merged into the last error term $\mathcal{O}(\varepsilon^{4+d})$. In Lemma S12, the differentiation is in the local coordinate residing on $\mathcal{T}_{\mathbf{x}}\mathcal{M}$. One can change the differentiation to the partial derivative on the normal coordinate system by (S24b). Additionally, one can again approximate the line integral $\int_0^1 (\delta d v)(\mathbf{u}(t))^\top \mathbf{u}'(t) dt = \int_0^1 (\delta d v)(\gamma(t))^\top \gamma'(t) dt + \mathcal{O}(\varepsilon^{3+d} \delta)$ by (S24d), where γ is the geodesic connecting \mathbf{x}, \mathbf{y} . Since δ decays faster than ε , we can merge $\mathcal{O}(\varepsilon^{3+d} \delta)$ to $\mathcal{O}(\varepsilon^{4+d})$. It implies

$$\begin{aligned}
\int_{\mathcal{M}} w_T(\mathbf{x}, \mathbf{y}, \mathbf{z}) f_{xyz} d\mu(\mathbf{z}) &= \frac{2}{3} \varepsilon^{2+d} C_2 \int_0^1 [\delta d v(\gamma_{\mathcal{M}}(t))]^\top \gamma'_{\mathcal{M}}(t) dt \\
&+ \mathcal{O}(\varepsilon^{4+d}) + \mathcal{O}(\varepsilon^{d+2} \delta^2) + \mathcal{O}(\varepsilon^d \delta^3).
\end{aligned}$$

This completes the proof. \blacksquare

E.4 Proof of Theorem 3

Firstly, we need the following lemma to measure $w_E(\mathbf{x}, \mathbf{y})$

Lemma S14 (Kernel weight for edge).

$$\begin{aligned}
w_E(\mathbf{y}, \mathbf{z}) &= \int_{\mathbf{v} \in \mathbb{R}^d} w_T(\mathbf{y}, \mathbf{z}, \mathbf{v}) d\mu(\mathbf{v}) = \int_{\mathbf{z} \in \mathbb{R}^d} \exp\left(-\frac{\|\mathbf{v}-\mathbf{y}\|^2}{\varepsilon^2}\right) \exp\left(-\frac{\|\mathbf{v}-\mathbf{z}\|^2}{\varepsilon^2}\right) d\mathbf{z} \\
&= \int_{\mathbf{z} \in \mathbb{R}^d} \exp\left(-\frac{\sum_i (y_i - v_i)^2 + \sum_i (z_i - v_i)^2}{\varepsilon^2}\right) d\mathbf{z} \\
&= \int_{\mathbf{z} \in \mathbb{R}^d} \exp\left(-\frac{2 \sum_i (v_i - \frac{y_i + z_i}{2})^2 + \frac{1}{2} \sum_i (y_i - z_i)^2}{\varepsilon^2}\right) d\mathbf{z} \\
&= C_0 \exp\left(-\frac{\sum_i (y_i - z_i)^2}{2\varepsilon^2}\right) = \varepsilon^d C_0 \exp\left(-\frac{\|\mathbf{y}-\mathbf{z}\|^2}{2\varepsilon^2}\right),
\end{aligned}$$

where we define $C_0 = \frac{1}{\varepsilon^d} \int_{\mathbf{z} \in \mathbb{R}^d} \exp\left(-\frac{2\|\mathbf{z}\|^2}{\varepsilon^2}\right) d\mathbf{z}$.

Proof of Theorem 3. Using $\mathcal{L}_1^{\text{up}} = \mathbf{W}_E^{-1} \cdot \mathbf{B}_T \mathbf{W}_T \mathbf{B}_T^\top$ and Lemma 1, the expected value becomes

$$\begin{aligned}
\mathbb{E} [(\mathcal{L}_1^{\text{up}})_{[x,y]}] &= \mathbb{E}_{z,v} \left[\frac{\frac{1}{n} \sum_{z \notin \{x,y\}} w_T(\mathbf{x}, \mathbf{y}, \mathbf{z}) f_{xyz}}{\frac{1}{n} \sum_{v \notin \{x,y\}} w_T(\mathbf{x}, \mathbf{y}, \mathbf{v})} \right] \\
&= \mathbb{E}_z \left[\frac{1}{n} \sum_{z \notin \{x,y\}} w_T(\mathbf{x}, \mathbf{y}, \mathbf{z}) f_{xyz} \right] \cdot \mathbb{E}_v \left[\frac{w_E(\mathbf{x}, \mathbf{y})}{\frac{\varepsilon^{-d}}{n} \sum_{v \notin \{x,y\}} w_T(\mathbf{x}, \mathbf{y}, \mathbf{v})} \right] \cdot \frac{1}{w_E(\mathbf{x}, \mathbf{y})}.
\end{aligned} \tag{S26}$$

The last equality holds by the independence of random variables z, v . By *Monte-Carlo* approximation,

$$\begin{aligned}
\mathbb{E} \left[\frac{1}{n} \sum_z w_T(\mathbf{x}, \mathbf{y}, \mathbf{z}) f_{xyz} \right] &= \frac{2}{3} \varepsilon^{2+d} C_2 \int_0^1 [\delta d v(\gamma_{\mathcal{M}}(t))]^\top \gamma'_{\mathcal{M}}(t) dt \\
&+ \mathcal{O}(\varepsilon^{4+d}) + \mathcal{O}(\varepsilon^{d+2} \delta^2) + \mathcal{O}(\varepsilon^d \delta^3).
\end{aligned}$$

The last equality holds by Proposition 2. It is not difficult to show that $\mathbb{E} [\frac{1}{n} \sum_{\mathbf{z}} w_T(\mathbf{x}, \mathbf{y}, \mathbf{z})] = w_E(\mathbf{x}, \mathbf{y})$ following the proof of Proposition 2, implying that the \mathbb{E}_v term in (S26) is $1 + \mathcal{O}(n^{-1})$ using the standard ratio estimator. Therefore, with $w_E(\mathbf{x}, \mathbf{y}) = \varepsilon^d C_0 \exp(-\frac{\|\mathbf{y}-\mathbf{x}\|^2}{2\varepsilon^2})$, one has

$$\begin{aligned} \mathbb{E} [(\mathcal{L}_1^{\text{up}})_{[x,y]}] &= \frac{2}{3} \varepsilon^2 \frac{C_2}{C_0} \int_0^1 [\delta d v(\gamma_{\mathcal{M}}(t))]^\top \gamma'_{\mathcal{M}}(t) dt \\ &\quad + \mathcal{O}(\varepsilon^4) + \mathcal{O}(\varepsilon^2 \delta^2) + \mathcal{O}(\delta^3) + \mathcal{O}(n^{-1} \varepsilon^2 \delta). \end{aligned}$$

Let $\delta = \mathcal{O}(\varepsilon^{\frac{3}{2}})$, one can get

$$\mathbb{E} [(\mathcal{L}_1^{\text{up}})_{[x,y]}] = \frac{2}{3} \varepsilon^2 \frac{C_2}{C_0} \int_0^1 [\delta d v(\gamma_{\mathcal{M}}(t))]^\top \gamma'_{\mathcal{M}}(t) dt + \mathcal{O}(\varepsilon^4) + \mathcal{O}(\varepsilon^{\frac{7}{2}} n^{-1}). \quad (\text{S27})$$

This completes the proof. \blacksquare

F Proofs of the pointwise convergence of the *down* Helmholtzian

F.1 Proof of Proposition 4

Similar to the proof of Proposition 2, we are interested in showing asymptotic expansion

$$\int_{\mathbf{z} \in \mathbb{R}^d} w_E(\mathbf{y}, \mathbf{z}) f_{zy} d\mu(\mathbf{z}) - \int_{\mathbf{z} \in \mathbb{R}^d} w_E(\mathbf{x}, \mathbf{z}) f_{zx} d\mu(\mathbf{z}) \rightarrow c \int_0^1 [d\delta v(\gamma_{\mathcal{M}}(t))]^\top \gamma'_{\mathcal{M}}(t) dt.$$

From Corollary S9 in D, one has $d\delta v = -\sum_i \sum_j \frac{\partial^2 f_j}{\partial S_i \partial S_j} ds_i$ in local coordinate (s_1, \dots, s_d) with $v = \sum_i f_i ds_i$.

Lemma S15 (Asymptotic expansion of $\mathcal{L}_1^{\text{down}}$ in \mathbb{R}^d). *Under Assumption 1–2, and further assume With the choice of exponential kernel $\kappa_\varepsilon(u) = \exp(-u)$ and $v = (f_1, \dots, f_d) \in C^4(\mathcal{M})$. Let $\mathbf{u}(t) = \mathbf{x} + (\mathbf{y} - \mathbf{x})t$ for t in $[0, 1]$ be a parameterization of the straight line between nodes x, y and $\mathbf{u}'(t) = d\mathbf{u}(t)/dt$. With the choice of exponential kernel $\kappa(u) = \exp(-u)$, one has the following asymptotic expansion*

$$\begin{aligned} &\int_{\mathbf{z} \in \mathbb{R}^d} \left[w^{(1)}(\mathbf{y}, \mathbf{z}) f_{yz} - w^{(1)}(\mathbf{x}, \mathbf{z}) f_{xz} \right] dz \\ &= \frac{2}{3} C_0 C_1 \varepsilon^{2d+2} \int_0^1 [(d\delta v(\mathbf{u}(t)))]^\top \mathbf{u}'(t) dt + \mathcal{O}(\varepsilon^{2d+4}) + \mathcal{O}(\varepsilon^{2d+1} \delta^2). \end{aligned} \quad (\text{S28})$$

Proof. Similar to what we have done in Lemma S12, from expansion of S17 of Lemma S12, With the above expansion, we denote the 0th-, 1st-, and 2nd-order terms to be the following

$$f_{yz} = f_{yz}^{(0)} + f_{yz}^{(1)} + f_{yz}^{(2)} + \mathcal{O}(\varepsilon^3).$$

And

$$\begin{aligned} &\int_{\mathbf{z} \in \mathbb{R}^d} w^{(1)}(\mathbf{y}, \mathbf{z}) f_{zy} d\mathbf{z} - \int_{\mathbf{z} \in \mathbb{R}^d} w^{(1)}(\mathbf{x}, \mathbf{z}) f_{zx} d\mathbf{z} \\ &= \int_{\mathbf{z} \in \mathbb{R}^d} [w^{(1)}(\mathbf{y}, \mathbf{z})(f_{yz}^{(0)} + f_{yz}^{(1)} + f_{yz}^{(2)}) - w^{(1)}(\mathbf{x}, \mathbf{z})(f_{xz}^{(0)} + f_{xz}^{(1)} + f_{xz}^{(2)})] dz + \mathcal{O}(\varepsilon^{4+2d}). \end{aligned} \quad (\text{S29})$$

Claim (constant term). *The integral of constant term is 0.*

The above claim is true since

$$\begin{aligned} &\int_{\mathbf{z} \in \mathbb{R}^d} [w^{(1)}(\mathbf{y}, \mathbf{z}) f_{yz}^{(0)} - w^{(1)}(\mathbf{x}, \mathbf{z}) f_{xz}^{(0)}] d\mathbf{z} \\ &= \int_{\mathbf{z} \in \mathbb{R}^d} w^{(1)}(\mathbf{y}, \mathbf{z}) \int_0^1 \sum_i f_i(\mathbf{u}(1-t)) (\mathbf{y} - \mathbf{z})_i dt d\mathbf{z} \\ &\quad - \int_{\mathbf{z} \in \mathbb{R}^d} w^{(1)}(\mathbf{x}, \mathbf{z}) \int_0^1 \sum_i f_i(\mathbf{u}(1-t)) (\mathbf{x} - \mathbf{z})_i dt d\mathbf{z} = 0. \end{aligned} \quad (\text{S30})$$

Claim (First order term). *The integral of the first order term is 0. Since*

$$\begin{aligned} & \int_{\mathbf{z} \in \mathbb{R}^d} w^{(1)}(\mathbf{y}, \mathbf{z}) \int_0^1 \sum_{i,j} \frac{\partial f_i(\mathbf{x} + t(\mathbf{y} - \mathbf{x}))}{\partial S_j} (\mathbf{z} - \mathbf{y} + \mathbf{y} - \mathbf{x})_j (\mathbf{y} - \mathbf{z})_i (1-t) dt d\mathbf{z} \\ & - \int_{\mathbf{z} \in \mathbb{R}^d} w^{(1)}(\mathbf{x}, \mathbf{z}) \int_0^1 \sum_{i,j} \frac{\partial f_i(\mathbf{x} + t(\mathbf{y} - \mathbf{x}))}{\partial S_j} (\mathbf{z} - \mathbf{x} + \mathbf{x} - \mathbf{y})_j (\mathbf{x} - \mathbf{z})_i t dt d\mathbf{z} = 0. \end{aligned}$$

This claim holds from $\int_{\mathbf{z} \in \mathbb{R}^d} w^{(1)}(\mathbf{y}, \mathbf{z}) (\mathbf{y} - \mathbf{x})_j (\mathbf{y} - \mathbf{z})_i (1-t) d\mathbf{z} = 0$ and $\int_{\mathbf{z} \in \mathbb{R}^d} w^{(1)}(\mathbf{y}, \mathbf{z}) (\mathbf{z} - \mathbf{y})_j (\mathbf{y} - \mathbf{z})_i (1-t) d\mathbf{z} = \int_{\mathbf{z} \in \mathbb{R}^d} w^{(1)}(\mathbf{x}, \mathbf{z}) (\mathbf{z} - \mathbf{x})_j (\mathbf{x} - \mathbf{z})_i (1-t) d\mathbf{z}$

Claim (Second order term). *Similar tricks applied to the second order term. The integral is*

$$\begin{aligned} & \int_{\mathbf{z} \in \mathbb{R}^d} w^{(1)}(\mathbf{y}, \mathbf{z}) \int_0^1 \sum_{i,j,k} \frac{\partial^2 f_i(\mathbf{x} + t(\mathbf{y} - \mathbf{x}))}{\partial S_j \partial S_k} (\mathbf{z} - \mathbf{x})_j (\mathbf{z} - \mathbf{x})_k (\mathbf{y} - \mathbf{z})_i (1-t)^2 dt d\mathbf{z} \\ & - \int_{\mathbf{z} \in \mathbb{R}^d} w^{(1)}(\mathbf{x}, \mathbf{z}) \int_0^1 \sum_{i,j,k} \frac{\partial^2 f_i(\mathbf{x} + t(\mathbf{y} - \mathbf{x}))}{\partial S_j \partial S_k} (\mathbf{z} - \mathbf{y})_j (\mathbf{z} - \mathbf{y})_k (\mathbf{x} - \mathbf{z})_i t^2 dt d\mathbf{z} \\ & = \int_{\mathbf{z} \in \mathbb{R}^d} w^{(1)}(\mathbf{y}, \mathbf{z}) \int_0^1 \sum_{i,j,k} \frac{\partial^2 f_i(\mathbf{x} + t(\mathbf{y} - \mathbf{x}))}{\partial S_j \partial S_k} (\mathbf{z} - \mathbf{y} + \mathbf{y} - \mathbf{x})_j (\mathbf{z} - \mathbf{y} + \mathbf{y} - \mathbf{x})_k (\mathbf{y} - \mathbf{z})_i (1-t)^2 dt d\mathbf{z} \\ & - \int_{\mathbf{z} \in \mathbb{R}^d} w^{(1)}(\mathbf{x}, \mathbf{z}) \int_0^1 \sum_{i,j,k} \frac{\partial^2 f_i(\mathbf{x} + t(\mathbf{y} - \mathbf{x}))}{\partial S_j \partial S_k} (\mathbf{z} - \mathbf{x} + \mathbf{x} - \mathbf{y})_j (\mathbf{z} - \mathbf{x} + \mathbf{x} - \mathbf{y})_k (\mathbf{x} - \mathbf{z})_i t^2 dt d\mathbf{z}. \end{aligned}$$

We can drop odd function terms since $\int_{\mathbf{z} \in \mathbb{R}^d} w^{(1)}(\mathbf{y}, \mathbf{z}) (\mathbf{z} - \mathbf{y})_j (\mathbf{z} - \mathbf{y})_k (\mathbf{y} - \mathbf{z})_i d\mathbf{z} = 0$. We also have $\int_{\mathbf{z} \in \mathbb{R}^d} w^{(1)}(\mathbf{y}, \mathbf{z}) (\mathbf{y} - \mathbf{x})_j (\mathbf{y} - \mathbf{x})_k (\mathbf{y} - \mathbf{z})_i d\mathbf{z} = \varepsilon^d C_0 \cdot \mathcal{O}(\varepsilon^{d+1} \delta^2) = \mathcal{O}(\varepsilon^{2d+1} \delta^2)$. So the integral of second order term is

$$= \int_{\mathbf{z} \in \mathbb{R}^d} w^{(1)}(\mathbf{y}, \mathbf{z}) \int_0^1 \sum_{i,j,k} \frac{\partial^2 f_i(\mathbf{x} + t(\mathbf{y} - \mathbf{x}))}{\partial S_j \partial S_k} (\mathbf{z} - \mathbf{y})_j (\mathbf{y} - \mathbf{x})_k (\mathbf{y} - \mathbf{z})_i (1-t)^2 dt d\mathbf{z} \quad (\text{S31})$$

$$+ \int_{\mathbf{z} \in \mathbb{R}^d} w^{(1)}(\mathbf{y}, \mathbf{z}) \int_0^1 \sum_{i,j,k} \frac{\partial^2 f_i(\mathbf{x} + t(\mathbf{y} - \mathbf{x}))}{\partial S_j \partial S_k} (\mathbf{y} - \mathbf{x})_j (\mathbf{z} - \mathbf{y})_k (\mathbf{y} - \mathbf{z})_i (1-t)^2 dt d\mathbf{z} \quad (\text{S32})$$

$$- \int_{\mathbf{z} \in \mathbb{R}^d} w^{(1)}(\mathbf{x}, \mathbf{z}) \int_0^1 \sum_{i,j,k} \frac{\partial^2 f_i(\mathbf{x} + t(\mathbf{y} - \mathbf{x}))}{\partial S_j \partial S_k} (\mathbf{z} - \mathbf{x})_j (\mathbf{x} - \mathbf{y})_k (\mathbf{x} - \mathbf{z})_i t^2 dt d\mathbf{z} \quad (\text{S33})$$

$$- \int_{\mathbf{z} \in \mathbb{R}^d} w^{(1)}(\mathbf{x}, \mathbf{z}) \int_0^1 \sum_{i,j,k} \frac{\partial^2 f_i(\mathbf{x} + t(\mathbf{y} - \mathbf{x}))}{\partial S_j \partial S_k} (\mathbf{x} - \mathbf{y})_j (\mathbf{z} - \mathbf{x})_k (\mathbf{x} - \mathbf{z})_i t^2 dt d\mathbf{z} \quad (\text{S34})$$

$$+ \mathcal{O}(\varepsilon^{2d+1} \delta^2).$$

In (S31) and (S33), the integrals do not equal to 0 when $i = j$, in (S32) and (S34), integrals do not equal to 0 when $i = k$. Then the whole second order term becomes

$$- \int_{\mathbf{z} \in \mathbb{R}^d} w^{(1)}(\mathbf{x}, \mathbf{z}) \int_0^1 \sum_{i,j} \frac{\partial^2 f_j(\mathbf{x} + t(\mathbf{y} - \mathbf{x}))}{\partial S_i \partial S_j} (\mathbf{y} - \mathbf{x})_i (t^2 + (1-t)^2) (\mathbf{z} - \mathbf{x})_j^2 dt d\mathbf{z}. \quad (\text{S35})$$

From Lemma S14, we can use following integral

$$\int_{\mathbf{z} \in \mathbb{R}^d} w^{(1)}(\mathbf{z}, \mathbf{x}) (\mathbf{z} - \mathbf{x})_j^2 d\mathbf{z} = \int_{\mathbf{z} \in \mathbb{R}^d} \varepsilon^d C_0 \exp\left(-\frac{\|\mathbf{z} - \mathbf{x}\|^2}{2\varepsilon^2}\right) (\mathbf{z} - \mathbf{x})_j^2 d\mathbf{z} = \varepsilon^d C_0 \cdot 4\varepsilon^{d+2} C_1. \quad (\text{S36})$$

Recall that $d\delta\zeta_1 = -\sum_{i,j} \frac{\partial^2 f_i}{\partial S_i \partial S_j} ds_i$ from Proposition S7, and we can remove $(t^2 + (1-t)^2)$ by using the same method in S12. Therefore, putting things together we can get

$$\begin{aligned} & \int_{\mathbf{z} \in \mathbb{R}^d} [w^{(1)}(\mathbf{y}, \mathbf{z}) f_{yz}^{(0)} - w^{(1)}(\mathbf{x}, \mathbf{z}) f_{xz}^{(0)}] dz \\ &= \frac{8}{3} C_0 C_1 \varepsilon^{2d+2} \int_0^1 [(d\delta v(\mathbf{u}(t)))]^\top \mathbf{u}'(t) dt + \mathcal{O}(\varepsilon^{2d+4}) + \mathcal{O}(\varepsilon^{2d+1} \delta^2). \end{aligned} \quad (\text{S37})$$

■

The second step is to provide the error terms induced by the change of variables with lemma S13. Then we can prove Proposition 4

Proof of Proposition 4. The geodesic curve can be approximated by a straight line in the local tangent plane $\mathcal{T}_x \mathcal{M}$ with error $\mathcal{O}(\varepsilon^3)$. Therefore $f_{yz} = f_{y_p z_p} + \mathcal{O}(\varepsilon^4)$. With choice of exponential kernel, we have

$$\begin{aligned} & \int_{\mathbf{z} \in \mathcal{M}} (w_E(\mathbf{y}, \mathbf{z}) f_{yz} - w_E(\mathbf{x}, \mathbf{z}) f_{xz}) d\mathbf{z} \\ & \stackrel{(i)}{=} \int_{\max(\|\mathbf{z}-\mathbf{y}\|, \|\mathbf{z}-\mathbf{x}\|) < \varepsilon^\gamma} (w_E(\mathbf{y}, \mathbf{z}) f_{yz} - w_E(\mathbf{x}, \mathbf{z}) f_{xz}) d\mathbf{z} + \mathcal{O}(\varepsilon^{4+2d}) \\ & \stackrel{(ii)}{=} \int_{\mathbf{z} \in \mathbb{R}^d} \left[\left(\varepsilon^d C_0 (\exp(-\frac{\|\mathbf{y}-\mathbf{z}\|^2}{2\varepsilon^2}) - \frac{Q_{x,4}(\mathbf{z}, \mathbf{y})}{\varepsilon^2} \exp(-\frac{\|\mathbf{y}-\mathbf{z}\|^2}{2\varepsilon^2})) \right) \cdot f_{yz} \right. \\ & \quad \left. - \left(\varepsilon^d C_0 (\exp(-\frac{\|\mathbf{x}-\mathbf{z}\|^2}{2\varepsilon^2}) - \frac{Q_{x,4}(\mathbf{z}, \mathbf{x})}{\varepsilon^2} \exp(-\frac{\|\mathbf{x}-\mathbf{z}\|^2}{2\varepsilon^2})) \right) \cdot f_{xz} \right] \cdot ((1 + Q_{\mathbf{x},2}(\mathbf{z})) d\mathbf{z} + \mathcal{O}(\varepsilon^{4+2d})) \\ & = \frac{8}{3} \varepsilon^{2+2d} C_0 C_1 \int_0^1 [(d\delta v(\mathbf{u}(t)))]^\top \mathbf{u}'(t) dt + \mathcal{O}(\varepsilon^{4+2d}) + \mathcal{O}(\varepsilon^{1+2d} \delta^2). \end{aligned}$$

Equality (i) holds by Lemma S10. Equality (ii) is valid by first projecting $\mathbf{x}, \mathbf{y}, \mathbf{z}$ to $\mathcal{T}_x \mathcal{M}$, changing the variables $\mathbf{x}_p, \mathbf{y}_p, \mathbf{z}_p \rightarrow \mathbf{x}, \mathbf{y}, \mathbf{z}$, and using Lemma (S10) again. Terms consisting of $Q_{p,4}(\mathbf{x}, \mathbf{y})$ or $Q_{p,2}(\mathbf{x}, \mathbf{y})$ are in the high order, hence, they can be merged into the last error term $\mathcal{O}(\varepsilon^{4+2d})$. Then we can again approximate the line integral $\int_0^1 (d\delta v)(\mathbf{u}(t))^\top \mathbf{u}'(t) dt = \int_0^1 (d\delta v)(\gamma(t))^\top \gamma'(t) dt + \mathcal{O}(\varepsilon^3 \delta)$ by (S24d), where γ is the geodesic connecting \mathbf{x}, \mathbf{y} . Therefore, it implies that

$$\begin{aligned} & \int_{\mathbf{z} \in \mathcal{M}} (w_E(\mathbf{y}, \mathbf{z}) f_{yz} - w_E(\mathbf{x}, \mathbf{z}) f_{xz}) d\mathbf{z} \\ & = \frac{8}{3} \varepsilon^{2d+2} C_0 C_1 \int_0^1 (d\delta v)(\gamma'(t))^\top \gamma'(t) dt + \mathcal{O}(\varepsilon^{4+2d}) + \mathcal{O}(\varepsilon^{1+2d} \delta^2). \end{aligned} \quad (\text{S38})$$

■

F.2 proof of theorem 5

Using $\mathcal{L}_1^{\text{down}} = W_1 \cdot B_1 W_0^{-1} B_1^T$, the expectation becomes

$$\begin{aligned} \mathbb{E} [(\mathcal{L}_1^{\text{down}})_{[x,y]}] &= W_1 \cdot B_1 W_0^{-1} B_1^T = E_{z,v} \left[\frac{\frac{1}{n} \sum_{\mathbf{z} \neq \mathbf{y}} w^{(1)}(\mathbf{z}, \mathbf{y}) f_{yz}}{\frac{1}{n} \sum_{\mathbf{v} \neq \mathbf{x}} w^{(1)}(\mathbf{v}, \mathbf{y})} \right] - E_{z,v} \left[\frac{\frac{1}{n} \sum_{\mathbf{z} \neq \mathbf{x}} w^{(1)}(\mathbf{z}, \mathbf{x}) f_{xz}}{\frac{1}{n} \sum_{\mathbf{v} \neq \mathbf{x}} w^{(1)}(\mathbf{v}, \mathbf{x})} \right] \\ &= E_z \left[\frac{1}{n} \sum_{\mathbf{z} \neq \mathbf{y}} w^{(1)}(\mathbf{z}, \mathbf{y}) f_{yz} \right] \cdot E_v \left[\frac{w^{(0)}(\mathbf{y})}{\frac{1}{n} \sum_{\mathbf{v} \neq \mathbf{y}} w^{(1)}(\mathbf{v}, \mathbf{y})} \right] \cdot \frac{1}{w^{(0)}(\mathbf{y})} \\ &\quad - E_z \left[\frac{1}{n} \sum_{\mathbf{z} \neq \mathbf{x}} w^{(1)}(\mathbf{z}, \mathbf{x}) f_{xz} \right] \cdot E_v \left[\frac{w^{(0)}(\mathbf{x})}{\frac{1}{n} \sum_{\mathbf{v} \neq \mathbf{x}} w^{(1)}(\mathbf{v}, \mathbf{x})} \right] \cdot \frac{1}{w^{(0)}(\mathbf{x})}. \end{aligned}$$

The last equality holds by the independence of random variables \mathbf{z}, \mathbf{v} . By $E[\frac{1}{n} \sum_{\mathbf{v} \neq \mathbf{y}} w^{(1)}(\mathbf{v}, \mathbf{y})] = w^{(0)}(\mathbf{y}) = 4\varepsilon^{2d} C_0^2$ and $w^{(0)}(\mathbf{y}) = w^{(0)}(\mathbf{x})$, we can have similar analysis to Theorem 2. With

Monte-Carlo approximation and Lemma S15, one has

$$\mathbb{E} [(\mathcal{L}_1^{\text{down}})_{[x,y]}] = \frac{2}{3} \varepsilon^2 \frac{C_1}{C_0} \int_0^1 [\text{d}\delta v(\gamma_{\mathcal{M}}(t))]^\top \gamma'_{\mathcal{M}}(t) dt + \mathcal{O}(\varepsilon^4) + \mathcal{O}(\varepsilon \delta^2) + \mathcal{O}(n^{-1} \varepsilon^2 \delta). \quad (\text{S39})$$

G Proofs of the spectral consistency of down Laplacian

G.1 Outline of the proof

The proof for spectral consistency of 1 down-Laplacian is outlined in Figure 1. Instead of directly showing the consistency of 1 down-Laplacian (dashed line), one can use the existing spectral consistency of the Laplace-Beltrami operator Δ_0 to show the spectral consistency of Δ_1 . The first step of the proof is to show the *spectral dependency* of down Helmholtzian $\mathcal{L}_1^{\text{down}} = \mathbf{B}_1^\top \mathbf{W}_0^{-1} \mathbf{B}_1 \mathbf{W}_1$ to the corresponding graph Laplacian, i.e., $\mathcal{L} = \mathbf{W}_0^{-1} \mathbf{B}_1 \mathbf{W}_1 \mathbf{B}_1^\top$; or more generally, the spectral dependency between $k-1$ up and k down Laplacians. Proposition 1.2 of [Pos09] first showed the spectra of $\mathbf{L}_1^{\text{down}}$ and \mathbf{L}_0 away from 0 agree including multiplicity. [HJ13] later pointed out the aforementioned agreement between non-zero spectra could be extended to k unweighted Laplacian ($\mathbf{L}_k^{\text{down}}$ and $\mathbf{L}_{k-1}^{\text{up}}$). Here we provide an extension of the results to the weighted k Laplacians.

Lemma S16 (Spectral dependency of \mathcal{L}_k). *Let $\mathcal{S}(\mathbf{A})$ be the non-zero spectrum of matrix \mathbf{A} . The non-zero spectra of $\mathcal{L}_k^{\text{down}}$ and $\mathcal{L}_{k-1}^{\text{up}}$ agree including multiplicity, i.e., $\mathcal{S}(\mathcal{L}_k^{\text{down}}) = \mathcal{S}(\mathcal{L}_{k-1}^{\text{up}})$.*

Proof of the lemma can be found in Supplement G.2 as well as corollaries on finding the eigenvector of $\mathbf{L}_{k-1}^{\text{up}}$ from $\mathbf{L}_k^{\text{down}}$ (or vice-versa). This lemma points out that the non-zero spectrum of $\mathcal{L}_k^{\text{down}}$ is identical to the non-zero spectrum of $\mathcal{L}_{k-1}^{\text{up}}$. It indicates that the down graph Helmholtzian $\mathcal{L}_1^{\text{down}}$ is consistent if the corresponding *random walk* Laplacian $\mathcal{L} = \mathbf{I}_n - \mathbf{D}^{-1} \mathbf{K} = \mathbf{W}_0^{-1} \mathbf{B}_1 \mathbf{W}_1 \mathbf{B}_1^\top$ is consistent, with $\mathbf{W}_0, \mathbf{W}_1$ constructed from \mathbf{W}_2 as discussed in Section 3. The next Proposition investigates the consistency of \mathcal{L} .

Proposition S17 (Consistency of the random walk Laplacian \mathcal{L} with kernel (3)). *Under Assumption 1–2, same spectral consistency result as in Theorem 5 of [BS19] can be obtained for the corresponding $\mathcal{L} = \mathbf{W}_0^{-1} \mathbf{B}_1 \mathbf{W}_1 \mathbf{B}_1^\top$, with weights calculated by $\mathbf{W}_k = \text{diag}(|\mathbf{B}_{k+1}| \mathbf{W}_{k+1} \mathbf{1}_{n_{k+1}})$ for $k = 0, 1$.*

Sketch of proof. We first investigate the scenario when $w^{(2)}(\mathbf{x}, \mathbf{y}, \mathbf{z})$ is constant, i.e., $w^{(2)}(\mathbf{x}, \mathbf{y}, \mathbf{z}) = \mathbb{1}(\|\mathbf{x} - \mathbf{y}\| < \varepsilon) \mathbb{1}(\|\mathbf{x} - \mathbf{y}\| < \varepsilon) \mathbb{1}(\|\mathbf{x} - \mathbf{y}\| < \varepsilon)$. If $\kappa(\cdot)$ has exponential decay, one can show that the corresponding $w^{(1)}(\mathbf{x}, \mathbf{y})$ has exponential decay, implying the consistency of [BS19]. The above analysis can be naturally extended to general kernel $\kappa(\cdot)$ for $\kappa(\cdot)$ is upper bounded by the indicator kernel. ■

The last part of the proof is to show the agreement in the spectra of the continuous operators Δ_0 and Δ_1 . It was shown by using *Courant-Fischer-Weyl min-max principle* on Δ_1 that the non-zero spectrum of Δ_1^{down} (also known as the spectrum of the *co-exact/curl* 1-form) is a copy of non-zero eigenvalues of Δ_0 [DM95, Col06]. With the right arrow completed in Figure 1, the down Helmholtzian $\mathcal{L}_1^{\text{down}}$ is hence shown to converge *spectrally* to the spectrum of $\Delta_1^{\text{down}} = d_0 \delta_1$.

G.2 Spectral dependency and related corollaries

Proof of Lemma S16. From [SBH⁺20], the spectra of the *random walk* k -Laplacian and of the symmetrized k -Laplacian are identical, implying that one can study the spectrum of \mathcal{L}_k^s (symmetric) instead of \mathcal{L}_k . Following the proof of [Pos09], one has $\mathbf{W}_{k-1}^{-1/2} \mathbf{B}_k \mathbf{W}_k^{1/2} \mathcal{L}_k^{s,\text{down}} = \mathcal{L}_{k-1}^{s,\text{up}} \mathbf{W}_{k-1}^{-1/2} \mathbf{B}_k \mathbf{W}_k^{1/2}$ and $\mathbf{W}_k^{1/2} \mathbf{B}_k^\top \mathbf{W}_{k-1}^{-1/2} \mathcal{L}_{k-1}^{s,\text{up}} = \mathcal{L}_k^{s,\text{down}} \mathbf{W}_k^{1/2} \mathbf{B}_k^\top \mathbf{W}_{k-1}^{-1/2}$. This implies that the mapping between the images of $\mathcal{L}_k^{s,\text{down}}$ and $\mathcal{L}_{k-1}^{s,\text{up}}$ are isomorphisms. In mathematical terms, if $\tilde{\mathbf{B}}_k = \mathbf{W}_{k-1}^{-1/2} \mathbf{B}_k \mathbf{W}_k^{1/2} : \text{im}(\mathcal{L}_k^{s,\text{down}}) \rightarrow \text{im}(\mathcal{L}_{k-1}^{s,\text{up}})$ and $\tilde{\mathbf{B}}_k^* = \mathbf{W}_k^{1/2} \mathbf{B}_k^\top \mathbf{W}_{k-1}^{-1/2} : \text{im}(\mathcal{L}_{k-1}^{s,\text{up}}) \rightarrow \text{im}(\mathcal{L}_k^{s,\text{down}})$, we have $\tilde{\mathbf{B}}_k$ and $\tilde{\mathbf{B}}_k^*$ are isomorphisms. Since $\mathcal{L}_k^{s,\text{down}} = \tilde{\mathbf{B}}_k^* \tilde{\mathbf{B}}_k$ and $\mathcal{L}_{k-1}^{s,\text{up}} = \tilde{\mathbf{B}}_k \tilde{\mathbf{B}}_k^*$, the isomorphism of two operator implies $\dim(\text{im}(\mathcal{L}_k^{s,\text{down}})) = \dim(\text{im}(\mathcal{L}_{k-1}^{s,\text{up}}))$ and $\mathcal{S}(\mathcal{L}_k^{\text{down}}) = \mathcal{S}(\mathcal{L}_{k-1}^{\text{up}})$. This completes the proof. ■

Below are some corollaries of Lemma S16 which are not used in our analysis but are useful in practice. These lemmas connect the eigenvectors of \mathbf{L}_k (or \mathcal{L}_k) with the eigenvectors of \mathbf{L}_{k-1} (or \mathcal{L}_{k-1}).

Corollary S18 (Eigenvectors of \mathbf{L}_k and \mathbf{L}_{k-1}).

C.I Let $\phi_{k-1} \in \mathbb{R}^{n_{k-1}}$ be the eigenvector of \mathbf{L}_{k-1} with eigenvalues λ , then $\mathbf{B}_k^\top \phi_{k-1}$ is the eigenvector of $\mathbf{L}_k^{\text{down}}$ with same eigenvalue.

C.II Let $\phi_k \in \mathbb{R}^{n_k}$ be the eigenvector of \mathbf{L}_k with eigenvalues λ , then $\mathbf{B}_k \phi_k$ is the eigenvector of $\mathbf{L}_{k-1}^{\text{up}}$ with same eigenvalue.

Proof. For C.I, Let ϕ_{k-1} be the non-trivial eigenfunction of \mathbf{L}_{k-1} with eigenvalue λ , this implies $\mathbf{L}_{k-1} \phi_{k-1} = \lambda \phi_{k-1}$, therefore

$$\lambda \mathbf{B}_k^\top \phi_{k-1} = \mathbf{B}_k^\top \mathbf{L}_{k-1} \phi_{k-1} = (\mathbf{B}_k^\top \mathbf{B}_{k-1}^\top \mathbf{B}_{k-1} + \mathbf{B}_k^\top \mathbf{B}_k \mathbf{B}_k^\top) \phi_{k-1} = \mathbf{L}_k^{\text{down}} \mathbf{B}_k^\top \phi_{k-1}.$$

Therefore, $\mathbf{B}_k^\top \phi_{k-1}$ will be the eigenfunction of $\mathbf{L}_k^{\text{down}}$. Similarly, for C.II,

$$\lambda \mathbf{B}_k \phi_k = \mathbf{B}_k \mathbf{L}_k \phi_k = (\mathbf{B}_k \mathbf{B}_k^\top \mathbf{B}_k + \mathbf{B}_k \mathbf{B}_{k+1}^\top \mathbf{B}_{k+1}^\top) \phi_k = \mathbf{L}_{k-1}^{\text{up}} \mathbf{B}_k \phi_k.$$

This completes the proof. \blacksquare

Corollary S19 (Eigenvectors of \mathcal{L}_k and \mathcal{L}_{k-1}).

C.I Let $\phi_{k-1} \in \mathbb{R}^{n_{k-1}}$ be the eigenvector of \mathcal{L}_{k-1} with eigenvalues λ , then $\mathbf{B}_k^\top \phi_{k-1}$ is the eigenvector of $\mathcal{L}_k^{\text{down}}$ with same eigenvalue.

C.II Let $\phi_k \in \mathbb{R}^{n_k}$ be the eigenvector of \mathcal{L}_k with eigenvalues λ , then $\mathbf{W}_{k-1}^{-1} \mathbf{B}_k \mathbf{W}_k \phi_k$ is the eigenvector of $\mathcal{L}_{k-1}^{\text{up}}$ with same eigenvalue.

Proof. For C.I, since ϕ_{k-1} is the non-trivial eigenfunction of \mathcal{L}_{k-1} with eigenvalue λ , we have

$$\lambda \mathbf{B}_k^\top \phi_{k-1} = \mathbf{B}_k^\top \mathcal{L}_{k-1} \phi_{k-1} = (\mathbf{B}_k^\top \mathbf{B}_{k-1}^\top \mathbf{W}_{k-2}^{-1} \mathbf{B}_{k-1} \mathbf{W}_{k-1} + \mathbf{B}_k^\top \mathbf{W}_{k-1}^{-1} \mathbf{B}_k \mathbf{W}_k \mathbf{B}_k^\top) \phi_{k-1} = \mathcal{L}_k^{\text{down}} \mathbf{B}_k^\top \phi_{k-1}.$$

For the case in C.II, we need some little algebraic tricks to get rid of the weights \mathbf{W} before boundary operator.

$$\begin{aligned} \lambda \mathbf{W}_{k-1}^{-1} \mathbf{B}_k \mathbf{W}_k \phi_k &= \mathbf{W}_{k-1}^{-1} \mathbf{B}_k \mathbf{W}_k \mathcal{L}_k \phi_k \\ &= \left(\underbrace{\mathbf{W}_{k-1}^{-1} \mathbf{B}_k \mathbf{W}_k \mathbf{B}_k^\top}_{\mathcal{L}_{k-1}^{\text{up}}} \mathbf{W}_{k-1}^{-1} \mathbf{B}_k \mathbf{W}_k + \mathbf{W}_{k-1}^{-1} \underbrace{\mathbf{B}_k \mathbf{W}_k \mathbf{W}_k^{-1} \mathbf{B}_{k+1}^\top}_{=0} \mathbf{W}_{k+1} \mathbf{B}_{k+1}^\top \right) \phi_k \\ &= \mathcal{L}_{k-1}^{\text{up}} \mathbf{W}_{k-1}^{-1} \mathbf{B}_k \mathbf{W}_k \phi_k. \end{aligned}$$

This completes the proof. \blacksquare

G.3 Proof of Proposition S17

We first start with the following lemma that derives the closed form of $w^{(1)}(\mathbf{x}, \mathbf{y})$ when the weight on the triangles is an indicator function. Note that in the construction below, we ignore the $\kappa(\mathbf{x}, \mathbf{y})$ factor, i.e., we assume that $w^{(2)}(\mathbf{x}, \mathbf{y}, \mathbf{z}) = \kappa(\mathbf{x}, \mathbf{z})\kappa(\mathbf{y}, \mathbf{z})$, for a more concise notation; the $\kappa(\mathbf{x}, \mathbf{y})$ factor will be added back later.

Lemma S20 (The integral form of constant triangular weight). *Let ε be a bandwidth parameter. Further assume a constant triangular weight, i.e., $w^{(2)}(\mathbf{x}, \mathbf{y}, \mathbf{z}) = \mathbb{1}(\|\mathbf{z} - \mathbf{x}\| < \varepsilon) \mathbb{1}(\|\mathbf{z} - \mathbf{y}\| < \varepsilon)$, then*

$$\begin{aligned} w^{(1)}(\mathbf{x}, \mathbf{y}) &= \mathbb{1}(\|\mathbf{x} - \mathbf{y}\| < \delta) \int_{\mathbf{z} \in \mathcal{M}} w^{(2)}(\mathbf{x}, \mathbf{y}, \mathbf{z}) d\mathbf{z} \\ &= \mathbb{1}(\|\mathbf{x} - \mathbf{y}\| < \delta) C \cdot I_{1 - \frac{\|\mathbf{x} - \mathbf{y}\|^2}{4(\gamma\varepsilon)^2}} \left(\frac{d+1}{2}, \frac{1}{2} \right) + \mathcal{O}(\varepsilon^2). \end{aligned} \tag{S40}$$

Where $C = \varepsilon^d \cdot p \cdot C_d$, C_d is the volume of unit d -ball, i.e., $C_d = \pi^{d/2} / \Gamma(d/2 + 1)$, and $I_x(a, b)$ is the regularized incomplete beta function.

Proof. In the continuous limit, with constant sampling density p , we have

$$\begin{aligned} \varepsilon^{-d} \int_{\mathbf{z} \in \mathcal{M}} w^{(2)} d\mathbf{z} &= \varepsilon^{-d} \int_{\mathbf{z} \in \mathbb{R}^d} w^{(2)} d\mathbf{z} + \mathcal{O}(\varepsilon^2) \\ &= p \cdot 2 \cdot \text{Vol}_{\text{cap}} \left(\varepsilon - \frac{\|\mathbf{x} - \mathbf{y}\|_2}{2}; \varepsilon, d \right) = p \cdot C_d I_{1 - \frac{\|\mathbf{x} - \mathbf{y}\|_2}{4\varepsilon^2}} \left(\frac{d+1}{2}, \frac{1}{2} \right). \end{aligned}$$

The first equality holds from projecting $\mathbf{x}, \mathbf{y}, \mathbf{z}$ onto $\mathcal{T}_{\mathbf{x}}\mathcal{M}$ and using Lemma S13, $\mathcal{O}(\varepsilon^2)$ is from $Q_{\mathbf{x},4}(\mathbf{z}, \mathbf{y})$ and $Q_{\mathbf{x},2}(\mathbf{z})$ of (S24c) and (S24b), respectively. Last equality holds because

$$\begin{aligned} \text{Vol}_{\text{cap}}(h; r, d) &= \int_0^\phi C_{d-1} r^{d-1} \sin^{d-1} \theta r \sin \theta d\theta = C_{d-1} r^d \int_0^t \nu^{\frac{d-1}{2}} (1-\nu)^{-\frac{1}{2}} d\nu \\ &= C_{d-1} r^d B \left(\frac{d+1}{2}, \frac{1}{2} \right) I_{(2rh-h^2)/r^2} \left(\frac{d+1}{2}, \frac{1}{2} \right) \\ &= C_d r^d I_{(2rh-h^2)/r^2} \left(\frac{d+1}{2}, \frac{1}{2} \right). \end{aligned}$$

And,

$$C_{d-1} \cdot B \left(\frac{d+1}{2}, \frac{1}{2} \right) = \frac{\pi^{(d-1)/2}}{\Gamma(\frac{d-1}{2} + 1)} \frac{\Gamma(\frac{d+1}{2}) \Gamma(1/2)}{\Gamma(\frac{d}{2} + 1)} = C_d.$$

This completes the proof. ■

Proof of Proposition S17. It suffices to prove that the corresponding $w^{(1)}(\mathbf{x}, \mathbf{y})$ has exponential decay, and the $\mathcal{O}(\varepsilon^2)$ error term can be ignored in the asymptotic expansion of graph Laplacian operator. Let $w_{\mathbb{1}}^{(1)}(\|x - y\|; r)$ be (S40). The integral operator of general kernel κ can be decomposed into two parts, i.e.,

$$\begin{aligned} w^{(1)}(\mathbf{x}, \mathbf{y}) &= \int_{\mathcal{M}} \kappa(\mathbf{x}, \mathbf{z}) \kappa(\mathbf{y}, \mathbf{z}) d\mathbf{z} = \int_{\substack{\mathbf{z} \in \mathcal{M} \\ \max(\|\mathbf{z} - \mathbf{y}\|, \|\mathbf{z} - \mathbf{x}\|) \leq \varepsilon^\gamma}} \kappa(\mathbf{x}, \mathbf{z}) \kappa(\mathbf{y}, \mathbf{z}) d\mathbf{z} \\ &\quad + \int_{\substack{\mathbf{z} \in \mathcal{M} \\ \min(\|\mathbf{z} - \mathbf{y}\|, \|\mathbf{z} - \mathbf{x}\|) > \varepsilon^\gamma}} \kappa(\mathbf{x}, \mathbf{z}) \kappa(\mathbf{y}, \mathbf{z}) d\mathbf{z}. \end{aligned}$$

With $\min(\|\mathbf{z} - \mathbf{x}\|, \|\mathbf{z} - \mathbf{y}\|) < \varepsilon^\gamma$, one has $\kappa(\mathbf{x}, \mathbf{y}) \leq \mathbb{1}(\|\mathbf{x} - \mathbf{y}\| < \varepsilon^\gamma)$. Therefore, the first term can be bounded by $w_{\mathbb{1}}^{(1)}(\mathbf{x}, \mathbf{y}; \varepsilon^\gamma)$. The second term can be bounded by $\mathcal{O}(\varepsilon^3)$ using Lemma S10 with $g(\cdot) = 1$. Note that the result can be generalized to manifold with boundaries by the following. For the points that is ε^γ within the boundary $\partial\mathcal{M}$, the above inequality is still valid, for one can use a modified kernel $\kappa'(\mathbf{x}, \mathbf{y})$ with $\kappa'(\mathbf{x}, \mathbf{y}) = \kappa(\mathbf{x}, \mathbf{y})$ if $\mathbf{y} \in \mathcal{M}$ and 0 otherwise. Putting in $\kappa(\mathbf{x}, \mathbf{y})$, one has,

$$w^{(1)}(\mathbf{x}, \mathbf{y}) \leq \kappa(\mathbf{x}, \mathbf{y}) w_{\mathbb{1}}^{(1)}(\mathbf{x}, \mathbf{y}; \varepsilon^\gamma) + \kappa(\mathbf{x}, \mathbf{y}) \cdot \mathcal{O}(\varepsilon^2) \leq C \kappa(\mathbf{x}, \mathbf{y}) + \kappa(\mathbf{x}, \mathbf{y}) \cdot \mathcal{O}(\varepsilon^2).$$

Last inequality holds since $w_{\mathbb{1}}^{(1)}(\mathbf{x}, \mathbf{y}; \varepsilon^\gamma) \leq C$ from Lemma S20. The above inequality shows that $w^{(1)}(\mathbf{x}, \mathbf{y})$ can be decomposed into a term that has fast enough decay and another term which is bounded by $\mathcal{O}(\varepsilon^2)$. Note that the graph is built with radius δ , the second order expansion of the graph Laplacian integral operator [BS19] has a δ^2 term, implying that $\kappa(\mathbf{x}, \mathbf{y}) \cdot \mathcal{O}(\varepsilon^2)$ term can be bounded by $\mathcal{O}(\varepsilon^2 \delta^2) = \mathcal{O}(\delta^{10/3})$. Hence, spectral consistency as in Theorem 5 of [BS19] with bias & variance determined by $\mathcal{O}(\delta^{4/3}) = \mathcal{O}(\varepsilon^2)$ can be achieved. More specifically, since points are sampled with constant density from the manifold \mathcal{M} , the spectrum of $\mathcal{L} = \mathbf{W}_0^{-1} \mathbf{B}_1 \mathbf{W}_1 \mathbf{B}_1^\top$ with weight $\mathbf{w}_1 = |\mathbf{B}_2| \mathbf{w}_2$ and $\mathbf{w}_0 = |\mathbf{B}_1| \mathbf{w}_1$ converges to the spectrum of Laplace-Beltrami operator Δ_0 with bias & variance in the order of $\mathcal{O}(\varepsilon^2)$. ■

H Effects of the weights a, b between up/down Laplacians

Even though in Section 4 it was established that for the consistency of \mathcal{L}_1 , $a = \frac{1}{4}$ and $b = 1$, here we consider the possibility of choosing other non-negative values for a, b . This can be useful from a machine learning perspective, allowing one to emphasize either the gradient or the curl subspaces of \mathcal{L}_1 .

From HHD, the space of cochains \mathbb{R}^{n_1} can be decomposed into three different orthogonal subspaces: the image of $\mathcal{L}_1^{\text{down}}$ (gradient), the image of $\mathcal{L}_1^{\text{up}}$ (curl), and the kernel of both $\mathcal{L}_1^{\text{down}}$ and $\mathcal{L}_1^{\text{up}}$ (harmonic). Since these subspaces are orthogonal to each other, rescaling $\mathcal{L}_1^{\text{up}}$ and $\mathcal{L}_1^{\text{down}}$ with some constants a, b will only scale the spectra accordingly without altering the eigenvectors. We first investigate the spectrum of the rescaled \mathcal{L}_1 w.r.t. a, b with the following Corollary.

Corollary S21 (Spectrum of new \mathcal{L}_1). *The range of the spectra of \mathcal{L}_1 is $\lambda(\mathcal{L}_1) \in [0, \max(2a, 3b)]$.*

Proof. From [HJ13], $\lambda(\mathbf{W}_k^{-1}\mathbf{B}_{k+1}\mathbf{W}_{k+1}\mathbf{B}_{k+1}^\top) \in [0, k+2]$. From Lemma S16, one has $\mathcal{S}(\mathcal{L}_k^{\text{down}}) = \mathcal{S}(\mathcal{L}_{k-1}^{\text{up}})$. Thus we have $\lambda(\mathbf{B}_1^\top\mathbf{W}_0^{-1}\mathbf{B}_1\mathbf{W}_1) \in [0, 2]$ and $\lambda(\mathbf{W}_1^{-1}\mathbf{B}_2\mathbf{W}_2\mathbf{B}_2^\top) \in [0, 3]$. From HHD, an eigenvector can only be either curl, gradient, or harmonic flow. Thus the non-zero spectrum of \mathcal{L}_1 will simply be the union of two disjoint eigenvalue set. Since rescaling the matrix by a constant will only change the scales of the eigenvalues, the union of the (rescaled) down and up Laplacian will therefore be in the range of $[0, \max(2a, 3b)]$. This completes the proof. ■

Note that by choosing $a = \frac{1}{2}$ and $b = \frac{1}{3}$, the spectra of \mathcal{L}_1 , $\mathcal{L}_1^{\text{down}}$, and $\mathcal{L}_1^{\text{up}}$ are all upper bounded by 1.

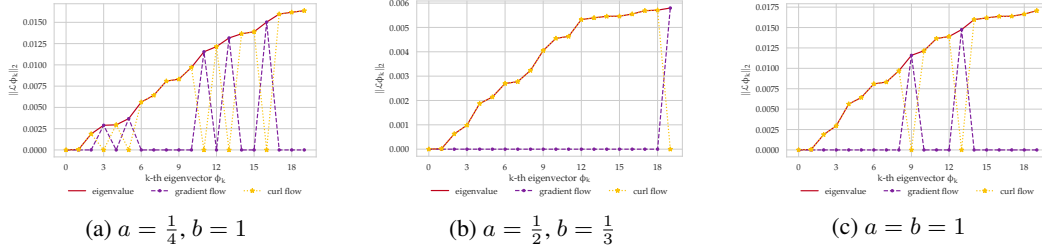


Figure S2: Shift in the rankings of the $\mathcal{L}_1^{\text{up}}$, $\mathcal{L}_1^{\text{down}}$ spectrum with different choices of a, b values for ethanol dataset. The eigenvector corresponds to the third eigenvalue in (a) is identical to that corresponds to the 18th in (b) and the ninth in (c). Note that the rankings within gradient or curl flows will not change by different choices of a, b , which can be shown by comparing the curl flows (yellow) between (a)–(c).

Based on the discussion above, different choices of a, b constants will shift the rankings between the curl flows ($\mathcal{L}_1^{\text{up}}$) and gradients flows ($\mathcal{L}_1^{\text{down}}$). This effect can be seen in Figure S2, with the first two gradient flows (in purple) in Figure S2a corresponds to the ninth and the thirteenth eigenvalues in Figure S2c. Considering the case $a = \frac{1}{2}; b = \frac{1}{3}$ when the spectra of $\mathcal{L}_1^{\text{down}}$ and $\mathcal{L}_1^{\text{up}}$ are both upper bounded by 1. Since there are only $n_0 - \beta_0$ non-zero eigenvalues in $\mathcal{L}_1^{\text{down}}$ (# of edges needed to form a spanning tree) compared to $n_1 - (n_0 - \beta_0) - \beta_1$ non-zero eigenvalues in $\mathcal{L}_1^{\text{up}}$ (# of independent triangles), the density of the gradient flows will be $\mathcal{O}(n_1/n_0)$ less than those of curl flow. That is to say, we will observe more curl flows than gradients flow for a fixed number of eigenvalues as shown in Figure S2b. Choosing a smaller a value increases the density of the gradient flow in the low frequency region (see a smaller choice of a in S2c and an even smaller a in S2a) It creates a more balanced distribution of flows in the low frequency regime. Note that the choice $a = \frac{1}{4}; b = 1$ creates the most balanced spectrum within the first 20 eigenvalues, as shown in Figure S2.

One can also analyze the random walk in the finite simplicial complex as in [SBH⁺20]. By letting $a = \frac{1}{2}; b = \frac{1}{3}$ with $\mathbf{W}_2 = \mathbf{I}_{n_2}$, they showed the constructed Helmholtzian corresponds to a finite random walk with equal probability ($p = \frac{1}{2}$) of performing up (diffuse to upper adjacent edges by common triangle) and down (diffuse to lower adjacent edges by common nodes) random walk. One can easily extend their analysis to non-constant weights \mathbf{W}_2 and different a, b values. This results in a random walk with probability $\frac{2a}{2a+3b}$ in performing lower random walk, while performing upper

random walk with probability $\frac{3a}{2a+3b}$. Similarly, $a = \frac{1}{2}; b = \frac{1}{3}$ will result in an equal probability of upper/lower random walks, as suggested in [SBH⁺20]. However, it might not be optimal for the transition probability when performing lower random walk (depending on w_1), which is much larger than the transition probability of the upper adjacent walk (depending on w_2). Hence, one might need to choose a smaller a value to ensure a more balanced random walk across all neighboring edges.

I Velocity field and cochain processing

I.1 Obtaining a 1-cochain

From the discussion in Section 2, the k -cochain is obtained by $\omega^k(\sigma_i) = \int_{\sigma_i} \zeta_k$. Given only the vector field $\zeta(\mathbf{x}_i) = \mathbf{f}(\mathbf{x}_i) \in \mathbb{R}^D \forall i \in [n]$, the 1-cochain ω on edge $e = (i, j)$ can be computed by $\omega_e = \int_0^1 \mathbf{f}(\gamma(t))\gamma'(t)dt$. With $\gamma(t) \approx \mathbf{x}_i + (\mathbf{x}_j - \mathbf{x}_i)t$, and $\gamma'(t) = d\mathbf{u}(t)/dt \approx (\mathbf{x}_j - \mathbf{x}_i)$, one can approximate $\mathbf{f}(\mathbf{u}(t)) \approx \mathbf{f}(\mathbf{x}_i) + (\mathbf{f}(\mathbf{x}_j) - \mathbf{f}(\mathbf{x}_i))t$ by Lemma S11,

$$\begin{aligned} \omega_e &= \int_0^1 \mathbf{f}^\top(\gamma(t))\gamma'(t)dt \approx \int_0^1 [\mathbf{f}(\mathbf{x}_i) + (\mathbf{f}(\mathbf{x}_j) - \mathbf{f}(\mathbf{x}_i))t]^\top (\mathbf{x}_j - \mathbf{x}_i)dt \\ &= \frac{1}{2}(\mathbf{f}(\mathbf{x}_i) + \mathbf{f}(\mathbf{x}_j))^\top (\mathbf{x}_j - \mathbf{x}_i). \end{aligned} \quad (\text{S41})$$

Note that (S41) can be written in a more concise form using boundary operator \mathbf{B}_1 . Let $\mathbf{F} \in \mathbb{R}^{n \times D}$ with $\mathbf{f}_i = \mathbf{F}_{i,:}; \mathbf{f}(\mathbf{x}_i)$, we have $[\mathbf{B}_1^\top | \mathbf{F}]_{[i,j]} = \mathbf{f}(\mathbf{x}_i) + \mathbf{f}(\mathbf{x}_j)$. Additionally, we have $[-\mathbf{B}_1^\top \mathbf{X}]_{[i,j]} = \mathbf{x}_j - \mathbf{x}_i$. Therefore,

$$\omega = -\frac{1}{2}\text{diag}(\mathbf{B}_1^\top \mathbf{X} \mathbf{F}^\top | \mathbf{B}_1). \quad (\text{S42})$$

One can follow the procedure stated below to obtain the point-wise vector field from 1-cochain. Define $\mathbf{X}_E = -\mathbf{B}_1^\top \mathbf{X}$, and $\chi_E = (\mathbf{X}_E)^{\circ 2} \mathbf{1}_D \in \mathbb{R}^{n_1}$, where $\mathbf{M}^{\circ p}$ is the *Hadamard power* of matrix \mathbf{M} , i.e., $[\mathbf{M}^{\circ p}]_{ij} = M_{ij}^p$. Further let $[\chi_E]_{[i,j]}$ represent the norm of $\mathbf{x}_j - \mathbf{x}_i$, i.e., $[\chi_E]_{[i,j]} = \|\mathbf{x}_j - \mathbf{x}_i\|_2^2$. Given the 1-cochain ω , one can solve the following D least squares problem to estimate the vector field \mathbf{F} on each point \mathbf{x}_i .

$$\hat{\mathbf{v}}_\ell = \underset{\mathbf{v}_\ell \in \mathbb{R}^n}{\text{argmin}} \left\{ \left\| \mathbf{B}_1^\top | \mathbf{v}_\ell - ([\mathbf{X}_E]_{:, \ell} \circ \chi_E) \circ \omega \right\|_2^2 \right\} \forall \ell = 1, \dots, D. \quad (\text{S43})$$

Where \circ, \oslash correspond to *Hadamard product* and *Hadamard division*, respectively. The solution to the ℓ -th least squares problem corresponds to the estimate of $f_\ell(\mathbf{x}_i)$ from $\frac{1}{2}(f_\ell(\mathbf{x}_i) + f_\ell(\mathbf{x}_j))$ as in (S41). More specifically,

$$\frac{1}{2}(f_\ell^\parallel(\mathbf{x}_i) + f_\ell^\parallel(\mathbf{x}_j)) = [([\mathbf{X}_E]_{:, \ell} \circ \chi_E) \circ \omega]_{[i,j]} = \frac{(x_{j,\ell} - x_{i,\ell})\omega_{ij}}{\|\mathbf{x}_j - \mathbf{x}_i\|^2}.$$

The estimated vector field is thus the concatenation of the D least squares solutions,

$$\hat{\mathbf{F}} = \begin{bmatrix} | & | & & | \\ \hat{\mathbf{v}}_1 & \hat{\mathbf{v}}_2 & \dots & \hat{\mathbf{v}}_D \\ | & | & & | \end{bmatrix} \in \mathbb{R}^{n \times D}. \quad (\text{S44})$$

I.2 Smoother vector field from the 1-cochain by a damped least square

Since the linear system in (S43) is overdetermined (n_1 is oftentimes greater than n_0), one can obtain a smoother estimated vector field from the 1-cochain using a damped least squares. That is to say, one can change the aforementioned loss function to the following,

$$\hat{\mathbf{F}} = \underset{\mathbf{F} \in \mathbb{R}^{n \times D}}{\text{argmin}} \left\{ \left\| \mathbf{B}_1^\top | \mathbf{F} - (\mathbf{X}_E \circ \chi_E) \circ \omega \right\|_F^2 + \lambda \|\mathbf{F}\|_F \right\}. \quad (\text{S45})$$

Here $\|\cdot\|_F$ represents the Frobenius norm. (S45) is essentially a multi-output Ridge regression problem. Figure S3 shows the estimated field from the 1-cochain constructed by the simulated field

(shown in Figure S3a) with different damping parameter λ 's. A larger λ yields a smoother (estimated) field in the original space, which can be seen by comparing Figures S3b ($\lambda = 0$), S3c ($\lambda = 1000$), and S3g ($\lambda = 10^5$). This is because a larger λ results in narrower “band” after proper scaling, as presented in the parity plot in Figure S3e–S3j. Cross validation (CV) can be used to choose the damping constant λ . Different scoring criteria used in the validation set will result in different chosen λ values. The scoring function we used throughout this paper is the Fisher z-transformed Pearson correlation value, for we care more about the relative relations of the vector field rather than the absolute scales. The selected regularization parameter (denoted λ_ρ^*) using this criteria tends to be larger than that chosen by the mean squared error (denoted λ_{MSE}^*), thus resulting in a smoother vector field (see e.g., Figure S3h v.s. Figure S3i). Figures S9 and S10 show all the vector fields reported in this paper estimated from the same 1-cochains with different regularization parameter. More specifically, estimated velocity fields with $\lambda = 0$, λ_ρ^* , and λ_{MSE}^* . As clearly shown in these Figures, we gain interpretability by having a smoother vector field without having too much structural changes using λ_ρ^* .

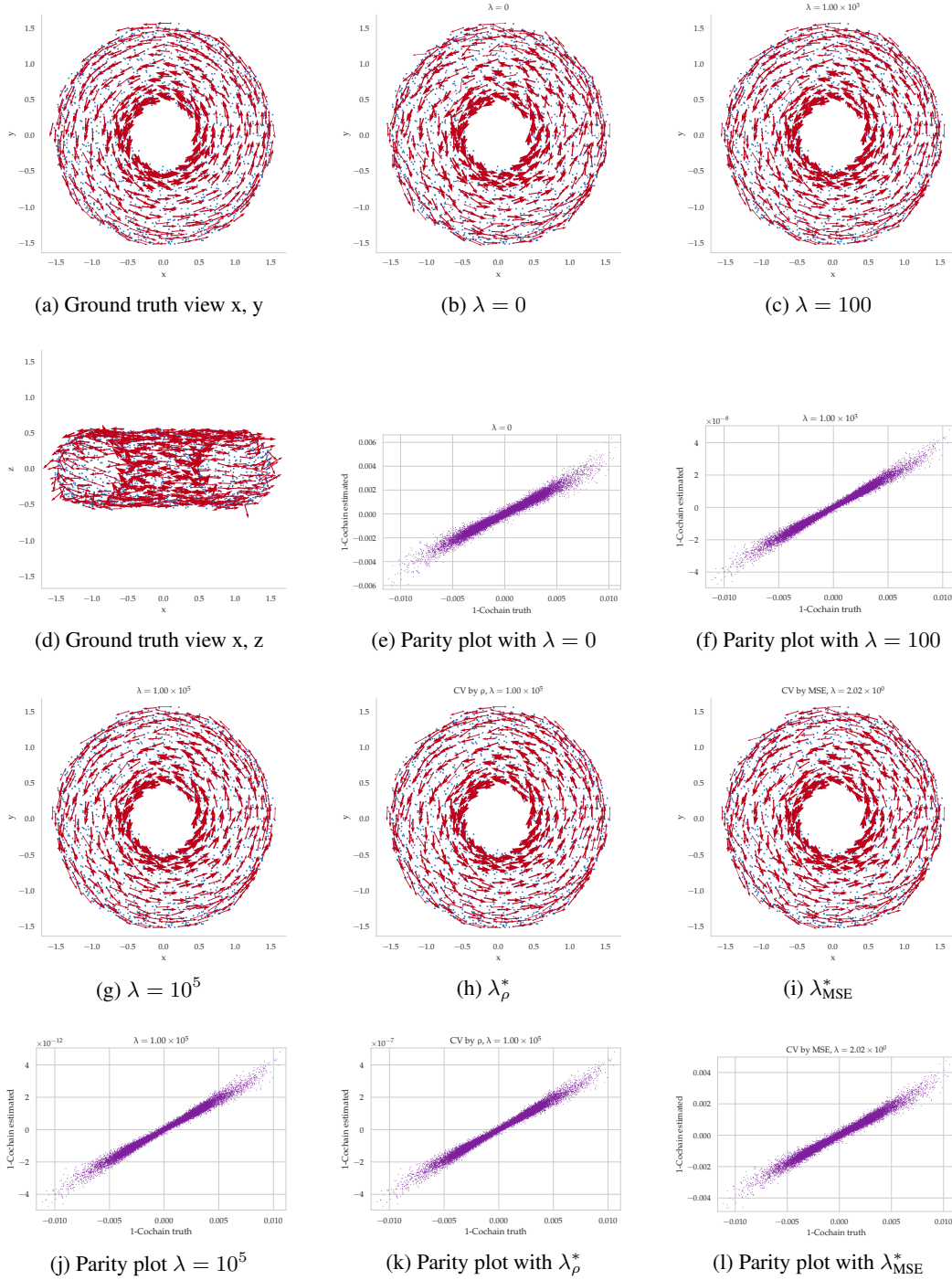


Figure S3: Estimated velocity field from the 1-cochain with different choices of damping parameter λ 's. (a), and (d) shows the synthetic field which cycles around the outer loop of a torus. λ_ρ^* and λ_{MSE}^* represent the damping constant chosen by cross validation (CV) with scoring function be fisher z-transformed Pearson correlation value and mean squared error, respectively.

I.3 Velocity field mapping between representations

Given a set of points $[\mathbf{x}_i]_{i=1}^n$ in \mathbb{R}^D sampled from a Manifold \mathcal{M} , vectors \mathbf{v}_i in the tangent subspace of \mathcal{M} at each data point, and a mapping $\varphi : \mathbb{R}^D \rightarrow \mathbb{R}^d$ from the ambient space to another representation; we are interested in obtaining the vector field $\mathbf{u}_i \in \mathbb{R}^d$ of each point in the new representation space $\phi_i = \varphi(\mathbf{x}_i)$. This problem can be solved by writing out explicitly the definition of the velocity field in the new representation space, i.e.,

$$\mathbf{u}_{ij} = \lim_{t \rightarrow 0} \frac{\varphi_j(\mathbf{x}_i + \mathbf{v}_i t) - \varphi_j(\mathbf{x}_i)}{t} = (\nabla_{\mathbf{x}} \varphi_i(\mathbf{x}_i))^\top \mathbf{v}_i. \quad (\text{S46})$$

The j -th component of the vector \mathbf{u}_i is essentially the directional derivative of the mapping φ along \mathbf{v}_i in the original space. Let $\mathfrak{J}_{\mathbf{x}} \varphi \in \mathbb{R}^{d \times D}$ be the Jacobian matrix, one can turn (S46) to,

$$\mathbf{u}_i = \mathfrak{J}_{\mathbf{x}} \varphi(\mathbf{x}_i) \mathbf{v}_i \text{ with } \mathfrak{J}_{\mathbf{x}} \varphi(\mathbf{x}_i) = \begin{bmatrix} -(\nabla_{\mathbf{x}} \varphi_1(\mathbf{x}_i))^\top - \\ -(\nabla_{\mathbf{x}} \varphi_2(\mathbf{x}_i))^\top - \\ \vdots \\ -(\nabla_{\mathbf{x}} \varphi_d(\mathbf{x}_i))^\top - \end{bmatrix} \mathbf{v}_i. \quad (\text{S47})$$

The velocity field mapping problem mapping now becomes a gradient estimation problem, which can be solved using any gradient estimation methods, e.g., [LSW09, MW06]. In this work, we use the gradient estimation method by [MS16] which aims to solve the (local) weighted linear regression on the local tangent plane. More specifically, the gradient of $f : \mathbb{R}^D \rightarrow \mathbb{R}$ at point \mathbf{x}_i , denoted as $\nabla_{\mathbf{x}} f(\mathbf{x}_i)$, is the minimizer of the following least squares problem,

$$\nabla_{\mathbf{x}} f(\mathbf{x}_i) = \underset{\mathbf{g} \in \mathbb{R}^D}{\operatorname{argmin}} \sum_{j \sim i} w_{ij} \|(f(\mathbf{x}_j) - f(\mathbf{x}_i)) - \mathbf{g}^\top (\mathbf{x}_j - \mathbf{x}_i)\|_2.$$

The w_{ij} can be estimated by the weights used in the Local PCA [CLM13]. Note that if the target embedding is not in Euclidean space, e.g., mapping the small molecule dataset from the ambient space \mathbf{X} to the torsion space as in Figure 2f and 2i, one has to use the proper boundary condition when calculating $f(\mathbf{x}_j) - f(\mathbf{x}_i)$. That is to say, the angular distance in the torsion space should be used (distance between $\pi/2$ and 2π is $-\pi/2$ rather than $3\pi/2$) to get smooth estimation of the gradients.

J Datasets

J.1 Synthetic datasets

Torus data Let the parameterization of a torus be

$$\begin{aligned} x &= (a + b \cos \alpha) \cos \beta; \\ y &= (a + b \cos \alpha) \sin \beta; \\ z &= a + b \sin \alpha. \end{aligned}$$

The torus dataset is generated by sampling $n = 2,000$ points from a grid in $(\alpha, \beta) \in [0, 2\pi]^2$ space and mapping them it into \mathbb{R}^3 by the above torus parametrization; the outer radius of torus is $a = 1$ and the inner radius is $b = 0.5$. Random gaussian noise is added in the first three coordinates. Additional 10 dimensional gaussian noise is added to each data point. The first two eigenforms (point-wise velocity field in Figure S4.) are obtained by solving the linear system as in (S43) using the first two eigenvectors ϕ_0 and ϕ_1 of \mathcal{L}_1^s .

2D strip and synthetic vector field for SSL We sampled $n = 5,000$ points from the grid in $[-2, 2]^2$. We then generate the vector field with $\zeta = 0.3\zeta_{\text{grad}} + 0.7\zeta_{\text{curl}}$, where the analytical form of ζ_{grad} and ζ_{curl} are

$$\begin{aligned} \zeta_{\text{curl}}(x, y) &= [x^2 y, -x y^2]; \\ \zeta_{\text{grad}}(x, y) &= [-x, -y]. \end{aligned}$$

Note that because we have the analytical form of the synthetic vector field, we do not need to use linear approximation of integration as in (S41) to generate the 1-cochain $[\omega]_{xy} = \int_{x \rightarrow y} \zeta(\gamma(t)) \gamma'(t) dt$.

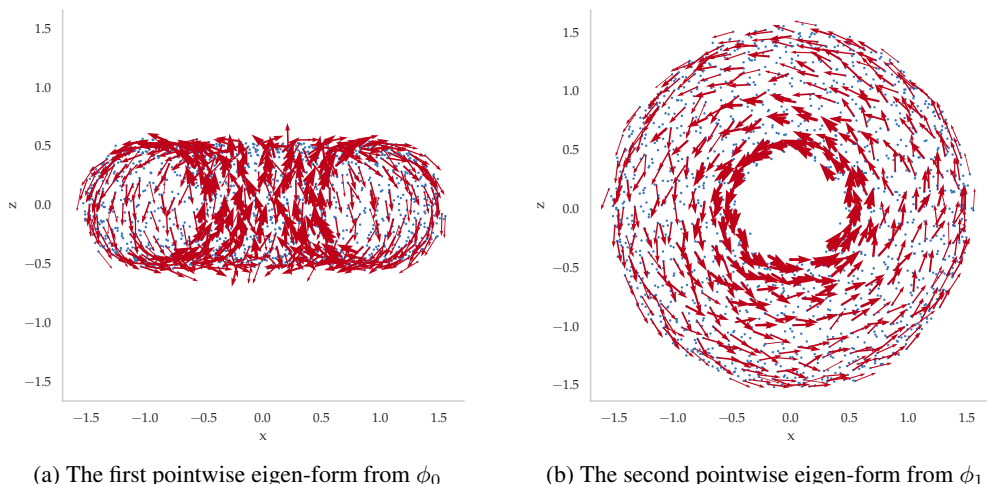


Figure S4: The first two *interpolated* eigenforms from the 1-cochain eigenvectors (ϕ_0 and ϕ_1) of \mathcal{L}_1^s .

J.2 Small molecule datasets

The ethanol and malondialdehyde (MDA) datasets [CTS⁺17] consist of molecular dynamics (MD) trajectories with different amounts of conformational degrees of freedom. A point in the dataset corresponds to a molecular configuration, which is recorded in the xyz format. More specifically, if the molecule has N atoms, then a configuration can be specified by a $N \times 3$ matrix. To remove the translational and rotational symmetry in the original configuration space, we preprocess the data by considering two of the angles of every triplet of atoms in a molecule (under the observation that two angles are sufficient to determine a triangle up to a constant). The linear relation is removed by applying *Principal component analysis* (PCA) with the unexplained variance ratio less than 10^{-4} . This generates the original data \mathbf{X} with *ambient dimension* upper bounded by $D \leq 2 \cdot \binom{N}{3}$. In Figure S5, we estimate the first 10 eigenforms by solving the linear system (S45). The 0-th eigenform clearly represents the bigger loop parameterized by Hydroxyl rotor as shown in the inset scatter plot of Figure 2d. In Figure S5b, it is difficult to tell whether the first eigenflow corresponds to Methyl rotor or not. One can overcome this issue by mapping the first eigenform to the torsion space with prior knowledge as illustrated in Figure 2f. Harmonic flows often represent a global structure; by contrast, flows in Figure S5d–S5f are more localized, implying that the eigenflows are not harmonic. The Helmholtz-Hodge decomposition of the eigenvectors of \mathcal{L}_1 in Figure S5c confirms this.

Figure S6 shows the scatter plot of the first three principal components of the MDA dataset. As clearly shown in the figures, it is difficult to make sense of the topological structure for the manifold of such dataset is a torus embedded in a 4 dimensional space. With the aid of the first two harmonic eigenforms, one can infer that the first loop travels in the direction of northwest to southeast, while the second loop goes diagonally from northeast to southwest. With proper prior knowledge, one can map the harmonic eigenforms to the torsion space to get a better visualization, as shown in Figure 2i.

J.3 Ocean drifter dataset

The ocean drifter data, also known as *Global Lagrangian Drifter Data*, were collected by NOAA’s Atlantic Oceanographic and Meteorological Laboratory. The dataset was used in [FP15] to analyze the Lagrangian coherent structures in the ocean current, showing that certain flow structures stay coherent over time. Each point in the dataset is a buoy at a certain time, with buoy ID, location (in latitude & longitude), date/time, velocity, and water temperature available to the practitioner. We extract the buoys that were in the North Pacific ocean dated between 2010 to 2019. The original sample size is around 3 million, we sampled 1,500 furthest buoy that meet the above criteria.

The velocity field in the original data depends a lot on the events in the shorter time scale, e.g., wind or faster changing ocean current. In comparison, ocean motions at longer time scale oftentimes are more interesting to the scientists. Therefore, we discard the short-term velocity field in the original

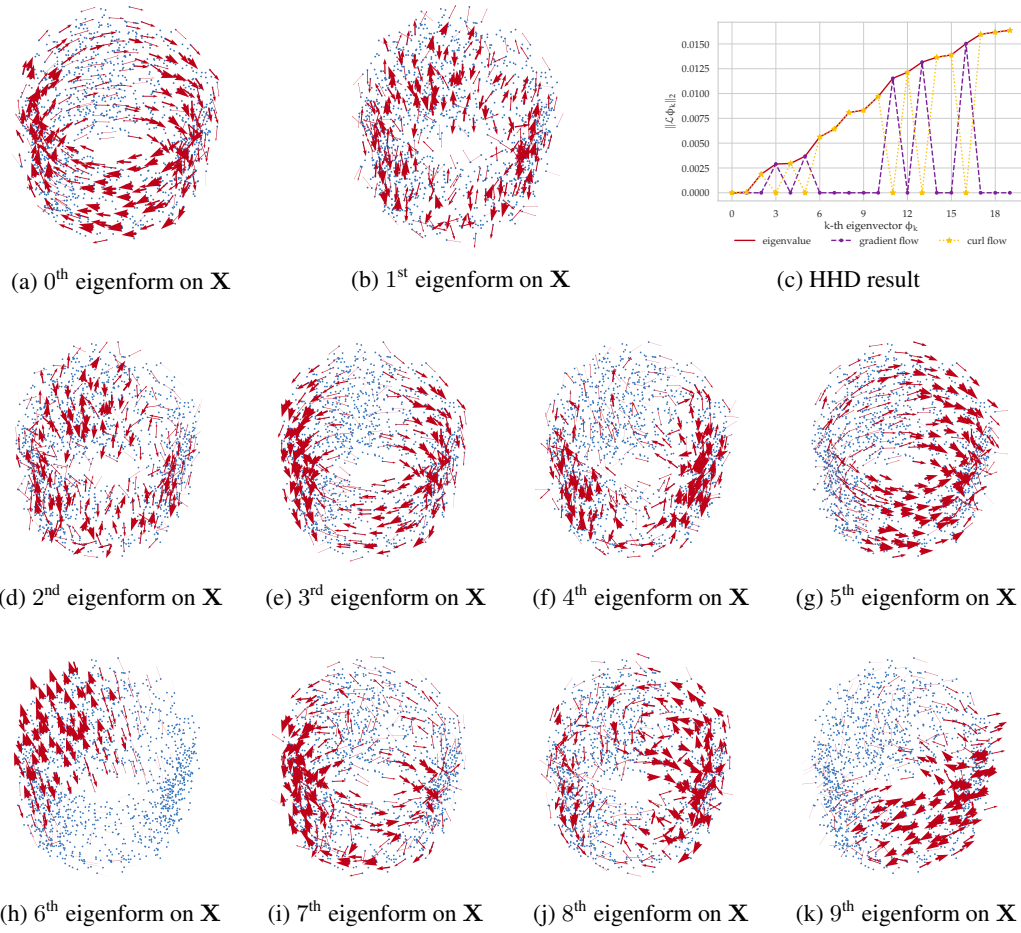


Figure S5: The first 10 estimated vertex-wise eigenforms on the original dataset \mathbf{X} by solving the linear system (S45). Figure (c) is the HHD on the first 10 eigenforms, showing that the first two eigenflows are harmonic; the third, fifth, eleventh, thirteenth, and the sixteenth eigenflows are gradient flow, while the rest are curl flows.

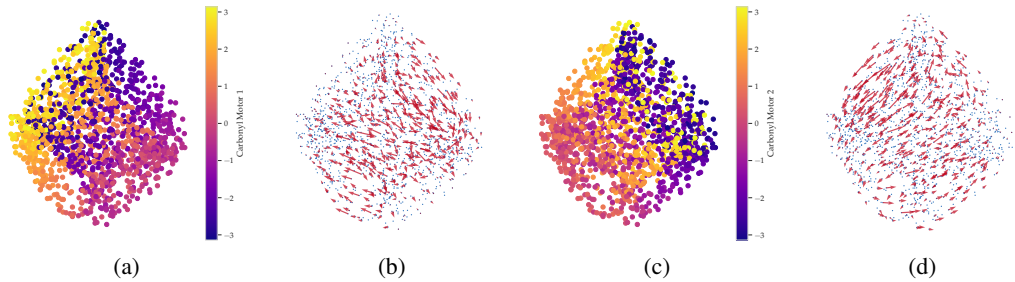


Figure S6: The harmonic eigenflows of the MDA dataset. (a) and (c) are the scatter plot of the first three PCs colored by the first and second Carbonyl rotors (purple and yellow in the inset of 2g, see also 2i). (b) and (d) represent the first two harmonic eigenforms estimated from the eigenvectors of \mathcal{L}_1^s . The zeroth eigenform in (b) parameterizes the first carbonyl rotor in (a), while the first eigenform in (d) represents the second carbonyl rotor as in (c). See also Figure 2i for a better visualization.

data and calculate the the velocity field as follows. We first compute the finite difference of the current location and the next location of the same buoy. The velocity of the buoy at current point is

obtained by dividing this quantity by the time difference. The 1-cochain can be constructed by linear approximate of integral as in (S41) after obtaining the velocity field of each point.

J.4 Single cell RNA velocity data

All of the RNA velocity data (Chromaffin, Mouse hippocampus, and human glutamatergic neuron cell differentiation dataset) as well as methods/codes to preprocess them can be found in [LMSZ⁺18]. The RNA velocity is a point-wise vector field in the ambient space predicting the future evolution of the cell. To generate the 1-cochain, we apply a linear interpolation as in (S41). The number of cells in the Chromaffin, mouse hippocampus, and human glutamatergic neuron cell differentiation datasets are $n' = 384$, $n' = 18,213$, and $n' = 1,720$, respectively. PCA is applied on the RNA expression, resulting in the ambient dimensions of the aforementioned three datasets being $D = 5, 10$, and 2 , respectively. We choose the furthest $n = 800$ and $n = 600$ cells for the mouse hippocampus and the human glutamatergic neuron data when building the simplicial complex. Since the sample size of the Chromaffin dataset is small, we used all the cells in our analysis.

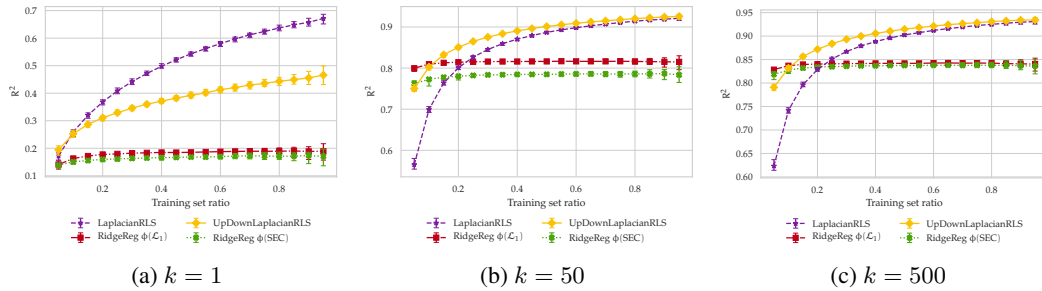


Figure S7: SSL results of the velocity fields of mouse hippocampus cell differentiation dataset with different smoothing parameter k .

In the RNA velocity framework, one can control how smooth the generated RNA velocity is by specifying the number of nearest neighbors k . The larger this parameter is, the smoother the vector field will become. We show in Figure S7 that the proposed algorithm out-performed other algorithms for several choices of smoothness values. Note that in theory, the UpDownLaplacianRLS should be at least as good as LaplacianRLS algorithm, for the first one is the extension of the second method. However, since we only choose the hyperparameter when train ratio is 0.2, it is possible that the under-performance of UpDownLaplacian seen in Figure S7a is due to suboptimal choices of parameters.

K SSL experiments on the divergence free flows

The \mathbf{B}_1 -SSL algorithm proposed by [JSSB19] works on (approximately) divergence-free flow. However, the assumption is not always valid for the flows observed in the many real datasets are often times a mixture of gradient, curl, and harmonic flows. Applying the \mathbf{B}_1 -SSL algorithm by [JSSB19] do not results in a good result, as shown in Figures S8a–S8d. Note that these figures are identical to Figures 3e–3h, but with the SSL results from [JSSB19] (blue curves) added. Except for the synthetic flow, the performances of \mathbf{B}_1 -SSL are as bad as random guess.

To further evaluate \mathbf{B}_1 -SSL of [JSSB19], in comparison with our \mathcal{L}_1 based SSL algorithms, we artificially create data that satisfies the \mathbf{B}_1 -SSL assumptions. Namely, we extract the curl component from the computed 1-cochain using HHD. In mathematical terms, we first solve the following linear system to get the vector potential $\hat{\mathbf{v}} = \operatorname{argmin}_{\mathbf{v} \in \mathbb{R}^{n_2}} \|\mathbf{B}_2 \mathbf{v} - \omega\|_2$. The curl component is obtained by projecting 1-cochain ω onto the image of \mathbf{B}_2 , i.e., $\omega_{\text{curl}} = \mathbf{B}_2 \hat{\mathbf{v}}$. The estimated velocity field from the curl cochains for each datasets can be found in Figures S8e–S8h. As shown in Figure S8i–S8l, the proposed algorithms based on both the up and down Laplacian out-perform [JSSB19] for small train/test ratio. In fact, the performance of \mathbf{B}_1 -SSL is always weak until the proportion of labeled examples exceeds about 0.7. For manifolds with simple structure, i.e., 2D plane and ocean dataset, [JSSB19] can achieve almost perfect predictions ($R^2 \approx 1$) when train-test ratio ≥ 0.9 . However, this is not the case for manifolds with complex structures, e.g., RNA velocity datasets.

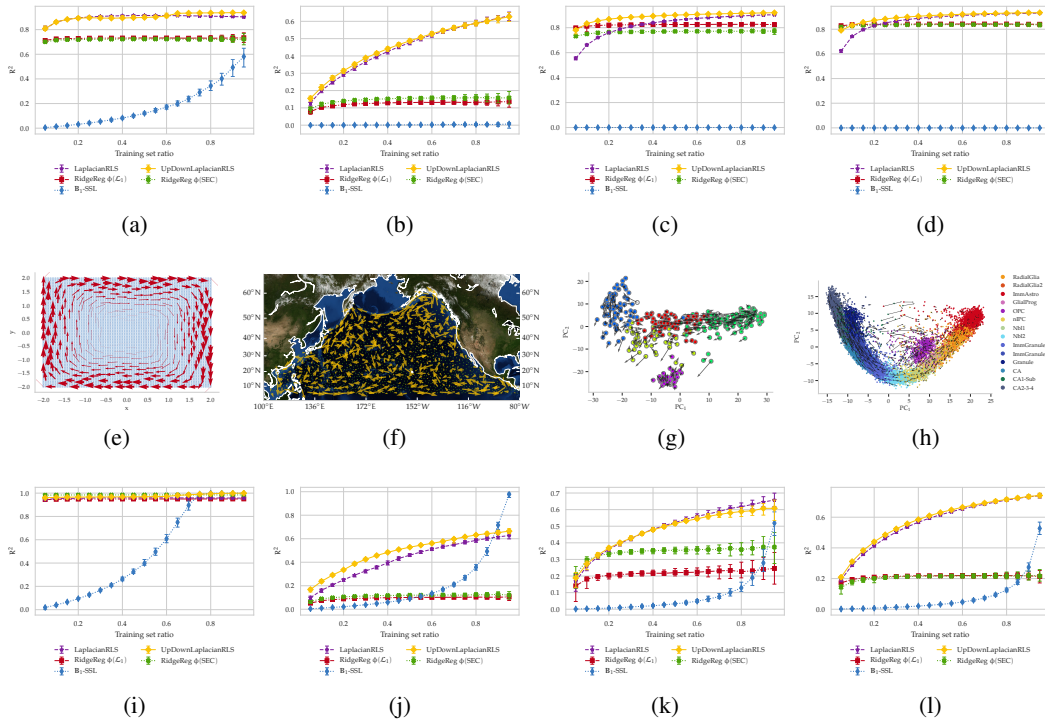


Figure S8: SSL results on various datasets with the B_1 -SSL proposed by [JSSB19]. Columns from left to right correspond to the results of 2D strip, ocean buoy, Chromaffin cell differentiation, and mouse hippocampus cell differentiation dataset. The top row shows the SSL results on the original velocity field with the result of B_1 -SSL (blue curve) added. The second row represents the curl component of the flows in Figure 3 using HHD. The third row are the SSL results of the data with the curl flow shown in the second row.

L Choice of regularization parameter λ for estimating point-wise velocity field from 1-cochain—vector field from all experiments

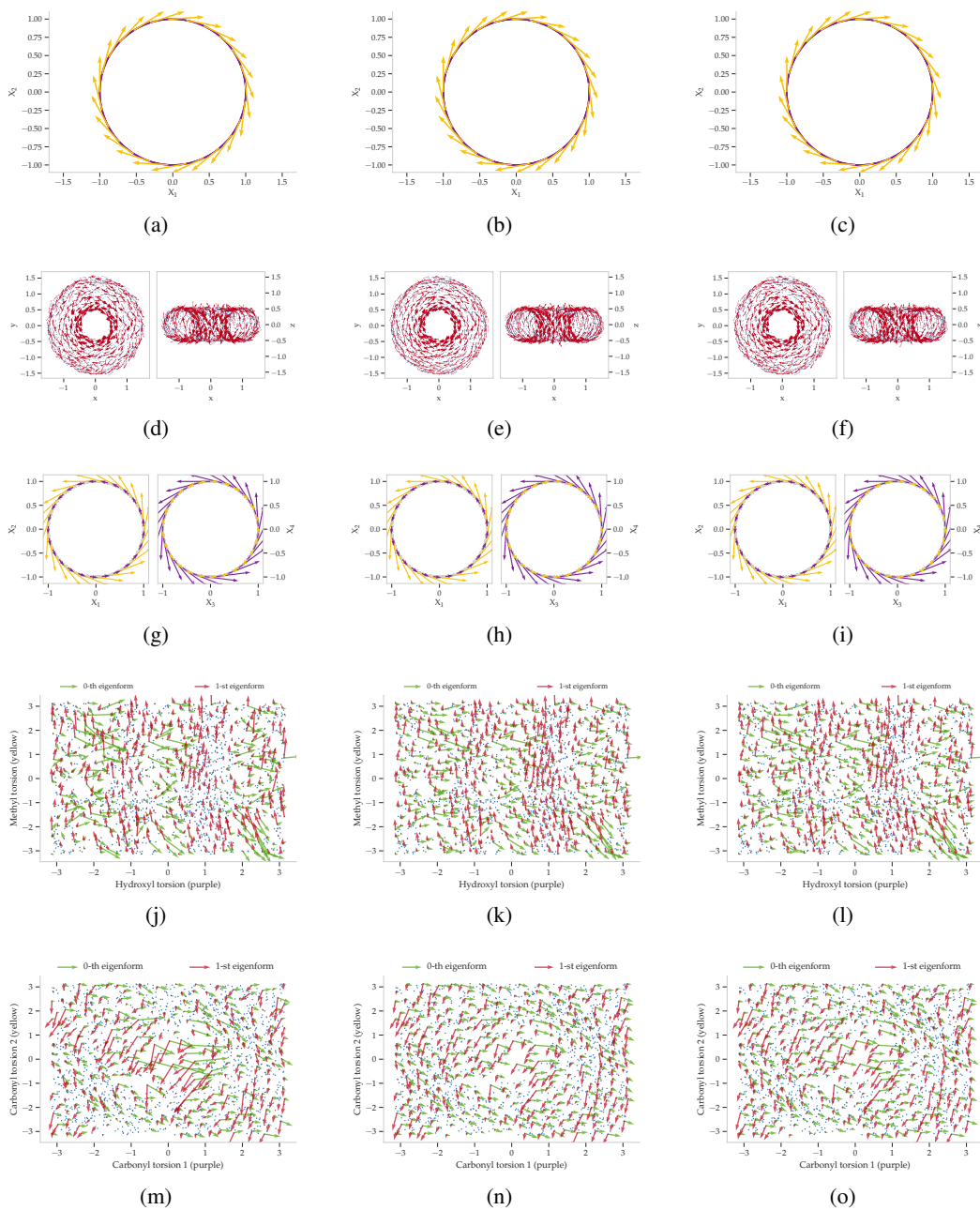


Figure S9: Comparisons of the estimated velocity fields from 1-cochain for various datasets with different regularization coefficient λ 's. Columns from left to right are $\lambda = 0$, λ^* , and λ_{MSE}^* (see more detail in Supplement I.2 and Figure S3). Rows from top to bottom correspond to the eigenflows of synthetic circle, eigenflows of synthetic torus, eigenflows of synthetic flat torus, eigenflows of ethanol in torsion space, and eigenflows of MDA in torsion space. The last two vector fields are mapped from original PCA space \mathbf{X} to torsion space using (S47).

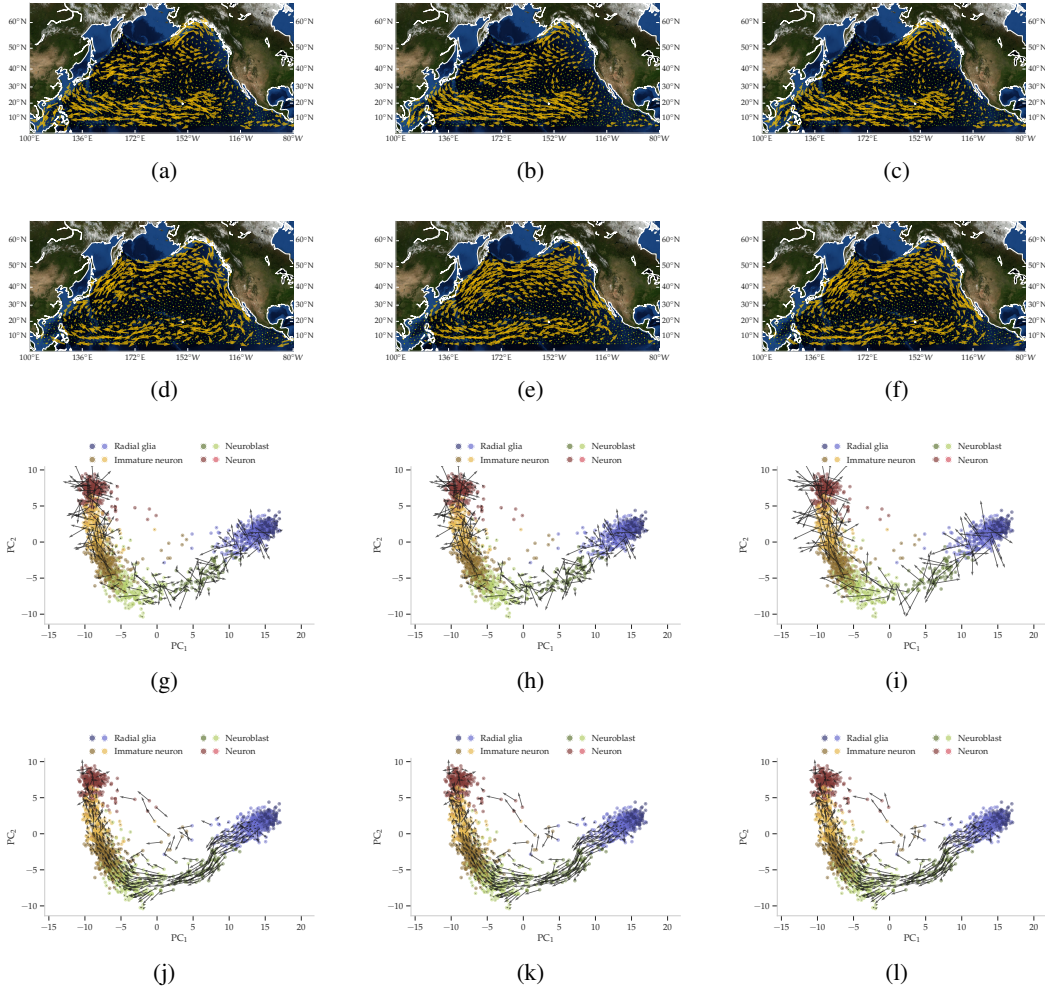


Figure S10: Comparisons of the estimated velocity fields from 1-cochain for various datasets with different regularization coefficient λ 's. Columns from left to right are $\lambda = 0$, λ_p^* , and λ_{MSE}^* (see more detail in Supplement I.2 and Figure S3). Rows from top to bottom correspond to the smoothed velocity field of ocean buoy dataset, estimated velocity field from the inverse problem on ocean buoy data, estimated velocity field of the zero-padded cochain on the human glutamatergic neuron data, and the estimated velocity from the inverse problem on human glutamatergic neuron dataset.